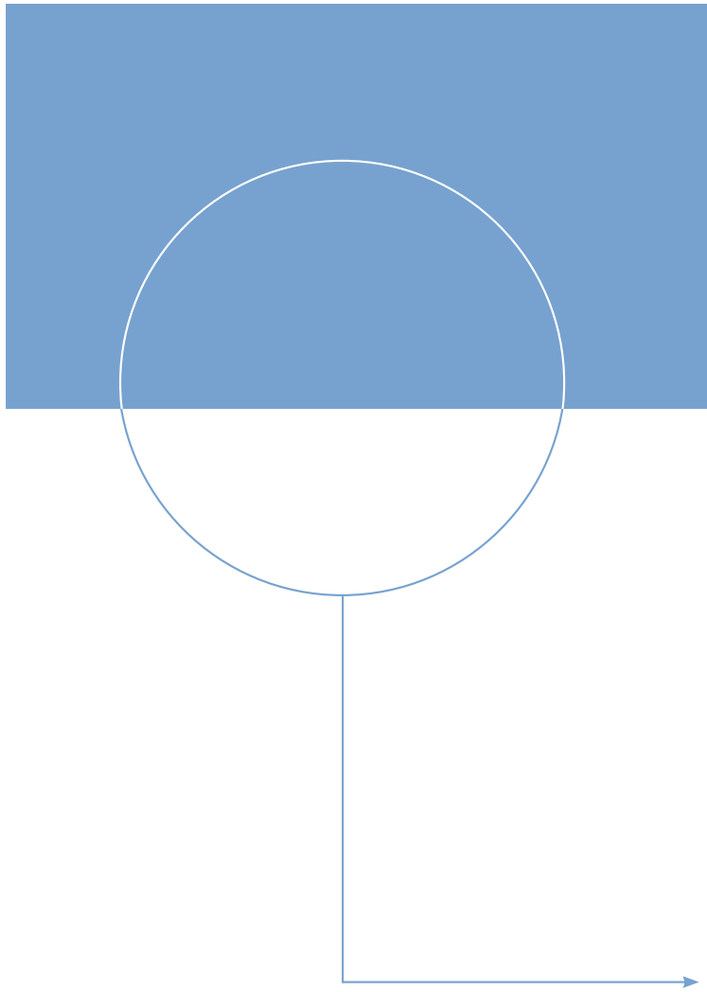

Sindre Steen Eikeland

Development of a miniaturized drone for indoor climate monitoring

June 2020

Master's thesis
2020
Sindre Steen Eikeland
Master's thesis

NTNU
Norwegian University of Science and Technology
Faculty of Information Technology and Electrical Engineering
Department of Engineering Cybernetics

NTNU
Norwegian University of Science and Technology
NTNU
Norwegian University of Science and Technology

NTNU

Norwegian University of
Science and Technology

Development of a miniaturized drone for indoor climate monitoring

Sindre Steen Eikeland

Industrial Cybernetics
Submission date: June 2020
Supervisor: Tor Arne Johansen
Co-supervisor: Geir Mathisen

Norwegian University of Science and Technology
Department of Engineering Cybernetics

Samandrag

Denne masteroppgåva tar eit første steg inn i utviklinga av ei autonom drone for overvaking av innandørsklima.
Ei ramme vart designa og 3D-printa for å fungere som eit grunnlag for framtidig testing av sensorar for overvaking av innandørsklima, samt maskinvare for autonom styring av dronen.
I tillegg til ramma, vart det designa og 3D-printa eit sensorkammer med luftinntak for montering til ramma som ein ekstern modul. Det same vart gjort for LiDAR-fester. Det viste seg seinare at den innbilte metoden for å feste modulane til ramma ikkje fungerte, og ingen av modulane vart testa. Teoretiske estimat indikerte eit velfungerande sensorkammer, medan seinare analyse og diskusjon sådde tvil om dette, og presenterte heller eit alternativ.

Ei løysing før trådlaus lading vart utvikla og testa med suksess, med opp til 0.8 A ladestraum og eit potensiale på $\sim$1.6 A. Løysinga kan brukast i eit autonomt oppsett, sjølv om det testa oppsettet manglar enkelte fordelaktige kvalitetar.
Dei utførde flytestane var dominert av ei driftande drone og, i byrjinga, mykje støy på gyroskopet. Sjølv om implementering av eit "notch filter" praktisk talt eliminerte støy på gyroskopet, fortsette driftinga. Ein gyroskop-akselerometer "dance theory" med ubalanserte motorar vart sett på som ei mogleg årsak til dette problemet.
Uheldigvis vart fleire komponentar i dronen seinare øydelagt, noko som gjorde at problemet med drifting aldri vart løyst. Av same årsak vart heller ikkje sensorkammeret testa.

Kort summert har denne masteroppgåva produsert ei konseptuell drone, med lågare vekt enn andre liknande eksempel, samtidig som den truleg er for stor til å kunne kallast ei "miniatyrisert drone". Plassering av miljøsensorar på dronen vart foreslått, der tilsvarande sensorar for nokre av dei ikkje var inkludert i eksisterande løysingar. Kombinert med grunnlag for trådlaus autonom lading finnast, så vidt forfattaren kjent, ingen liknande eksisterande dronar.

Summary

This thesis takes the first step into the development of an autonomous drone for indoor climate monitoring.
A frame was designed and 3D-printed, with the aim of providing a base for testing of indoor climate sensors and autonomous hardware in the future.
In addition to the frame, a sensor chamber with air intakes was printed for modular mounting to the frame. Also LiDAR mounts were designed and printed for modular mounting. Unfortunately, the mounting technique did not work as intended, and none of the external modules were tested. Theory implied a well working sensor chamber, while analysis and discussion gave some doubt and presented an alternative.

A wireless charging solution was developed and successfully tested, with a charging current up to 0.8 A, and later potential of $\sim$1.6 A. The solution can be used as part of an autonomous solution, though the tested setup lacks some desirable features.
Flight tests conducted were dominated by a drifting drone and, initially, much gyro noise. With the implementation of a notch filter gyro noise was practically eliminated, but drifting persisted. A gyroscope-accelerometer "dance theory" and imbalanced motors seemed likely to be causing the drift.
Unfortunately, a fault in the drone resulted in damage to several components, and so the drifting was never resolved. The sensor chamber was, for the same reason, not tested either.

In short, this thesis has produced a conceptual drone lighter than discovered existing solutions. At the same time, the current prototype is likely too large for it to be called a miniaturized drone. Allocation of environmental sensors has also been suggested, some of which equivalents are not found in the existing solutions either. Combined with a base for wireless autonomous charging there are, to the best of knowledge, no existing drones similar to this.

Preface

This thesis concludes my time at NTNU, but also my time as a student, seven years after starting my first year as a bachelor student in Scotland.
The grounds for this thesis have been laid by **Kjeldsberg Eiendomsforvaltning AS** (KEF), who are eyeing the opportunity to improve today's indoor climate regulation in their estates. With this they aim to increase the employee's satisfaction and productivity, and reduce wasted energy through optimized regulation and understanding of indoor climate.

I would like to thank ...

... my supervisor, Prof. Tor Arne Johansen, as well as Kjeldsberg Eiendomsforvaltning AS, for the opportunity to dive deep in to the world of drones through my master thesis.

... Artur Piotr Zolich, for joining and helping me with valuable discussions and suggestions when it was hard to see the answer.

... Pål Kvaløy, for lending me essential equipment and providing valuable advice and assistance when necessary.

Table of Contents

Samandrag i

Summary iii

Preface v

Table of Contents vii

List of Tables xi

List of Figures xiii

Abbreviations xv

1 Introduction 1
- 1.1 The importance of indoor climate . . . 1
- 1.2 How indoor climate is monitored today . . . 2
- 1.3 The overall concept of a proactive approach by use of drone . . . 2
  - 1.3.1 Autonomous flight and measurements . . . 4
  - 1.3.2 Advantages and applications . . . 6
- 1.4 Existing solutions . . . 6
  - 1.4.1 State-of-the-art examples . . . 7
- 1.5 Aims for the project . . . 8

2 Basic Theory 9
- 2.1 Thrust to Weight Ratio . . . 9
- 2.2 Shroud design . . . 9
  - 2.2.1 Protective shrouds . . . 10
  - 2.2.2 Noise reducing shrouds . . . 10
  - 2.2.3 Thrust increasing shrouds . . . 11
- 2.3 Propeller air flow . . . 11
- 2.4 Power consumption . . . 13

2.4.1 Method 1 . . . 14
2.4.2 Method 2 . . . 15
2.5 Flow in air ducts . . . 16
2.6 Drone equations of motion . . . 17
2.6.1 PID regulator . . . 17
2.6.2 Equations of motion . . . 18
2.6.3 PID regulator design . . . 23
2.6.4 . . . 23

3 Design Specifications 25

4 Hardware 29
4.1 Propellers . . . 29
4.1.1 Size . . . 29
4.1.2 Pitch . . . 30
4.1.3 Number of blades . . . 30
4.1.4 Material . . . 30
4.1.5 Blade tip . . . 30
4.1.6 Selection of propellers . . . 31
4.2 Motors . . . 31
4.2.1 Thrust to Weight Ratio . . . 32
4.2.2 kV-rating . . . 32
4.2.3 Stator size . . . 32
4.2.4 Selection of motors . . . 32
4.3 ESC . . . 33
4.3.1 Single or 4-in-1 ESC . . . 33
4.3.2 Current rating . . . 33
4.3.3 Voltage rating . . . 33
4.3.4 Firmware . . . 34
4.3.5 ESC Protocol . . . 34
4.3.6 Processor . . . 35
4.3.7 Additional features . . . 35
4.3.8 Selection of ESC . . . 35
4.4 Flight Controller . . . 36
4.4.1 Voltage rating . . . 36
4.4.2 Firmware . . . 36
4.4.3 Processor . . . 36
4.4.4 UART . . . 36
4.4.5 Flight essential sensors . . . 37
4.4.6 Additional features . . . 37
4.4.7 Selection of FC . . . 37
4.5 Communication . . . 38
4.5.1 Frequency . . . 38
4.5.2 Number of channels . . . 38
4.5.3 TX protocol . . . 38
4.5.4 RX protocol . . . 39

4.5.5 Selection of communication hardware . . . 39
4.6 Battery . . . 40
4.6.1 Voltage rating . . . 40
4.6.2 Capacity . . . 40
4.6.3 Discharge rate . . . 40
4.6.4 Weight . . . 40
4.6.5 Selection of battery . . . 40
4.7 Hardware summary . . . 41

5 Frame Design and Simulation **43**
5.0.1 Desirable frame features . . . 44
5.0.2 Design 1 - Modular construction . . . 44
5.0.3 Design 2 - Light and flexible compromise . . . 51

6 Charging Solution **63**
6.1 The concept of charging LiPo-batteries . . . 63
6.2 Charging solution - on-board . . . 64
6.2.1 TP4056 module . . . 65
6.2.2 Battery Management System (BMS) . . . 65
6.2.3 Selected on-board charging solution . . . 66
6.3 Charger power supply - off-board . . . 66
6.3.1 Conductive power supply . . . 67
6.3.2 Inductive power supply . . . 67
6.3.3 Selected off-board power supply . . . 67
6.4 Test of charging solution . . . 68

7 Component Manufacturing **73**
7.0.1 Material selection . . . 74
7.0.2 Printing of the frame . . . 75
7.0.3 Printing of sensor chamber and LiDAR mounts . . . 80

8 Drone Assembly and Completion **83**
8.1 Hardware . . . 83
8.2 Software . . . 84
8.2.1 Betaflight setup . . . 84

9 Test flights **89**
9.1 Test flight #0 . . . 89
9.2 Test flight #1 . . . 91
9.3 Test flight #2 . . . 92
9.4 Test flight #3 . . . 93
9.5 Test flight #4 / Troubleshooting . . . 95
9.6 Remaining aspects for testing . . . 97

10 Analysis, Discussion and Further work **99**

11 Conclusion **109**

12 Further work **111**

Bibliography **111**

Appendix **119**
12.1 Simulation Appendix 119
12.2 Analysis Simulation Appendix 127

List of Tables

3.1 Drone design specifications 27

4.1 High and low pitch propeller qualities (GetFPV, 2018) 30
4.2 Flight controller processors (Liang, 2020b) 36
4.3 Hardware summary 41

5.1 Break-down of heart module 48
5.2 Break-down of FC module 49
5.3 Break-down of ESC module 50
5.4 Design 1 dimensions and weight 50
5.5 Sensor data (Kittelsen, 2019) 54
5.6 Design 2 specifications 61

6.1 BMS basic specifications (Banggood) 65
6.2 Components used in test of charging solution 68

7.1 Some physical properties of ABS and PLA (Singh et al., 2019)(Simplify3D) 75

9.1 Flight #0 tune 89
9.2 Flight #1 tune 91
9.3 Selected sets of current and voltage consumption during flight #3 94

List of Figures

1.1 Illustration of information flow in the overall concept 3
1.2 Flowchart of on-board mission processing 4
1.3 Flowchart of off-board mission processing 5

2.1 Air flow simulation of a 3D-scanned propeller (Uthira Kumar et al., 2017) 13
2.2 Comparison plots of the two methods. M1, M2 = Method 1, 2 16
2.3 PID regulated system 18
2.4 General layout of drone workings 19
2.5 Illustration of an earth-fixed frame and body-fixed frame 20

3.1 The complete construction of the drone 25

5.1 Templates of the platform module (left) and frame module (right) 45
5.2 Assembly of platform (yellow, middle) and frame modules (pink and orange, top and bottom, respectively). 45
5.3 The heart module carrying the motors, sensor chamber and air ducts . . . 46
5.4 Top: Connection between motors, ducts and sensor chamber. Bottom: LiDAR mount on the shorter side of the frame 46
5.5 The Flight Controller module carrying the FC 48
5.6 The ESC module carrying the ESC 49
5.7 The complete assembly of design 1 50
5.8 Main frame in design 2 51
5.9 Design 2 features: (1): Receiver slot (2): FC mounting poles (3): ESC mounting holes (4): Battery slot 52
5.10 Sensor chamber with intakes on the sides 53
5.11 Cross section of sensor chamber 54
5.12 Cross section of sensor chamber showing mounting to main frame (right hand side) 54
5.13 Front and rear view of forward/side-way (left) and downward (right) facing LiDAR mounts 56
5.14 Motor forces and meshed model prior to solving 57

5.15 Stress distribution (von Mises) in drone frame (maximum 3.221 MPa) . . 58
5.16 Displacement in drone frame (maximum 0.5963 mm) 58
5.17 Comparison of 300, 550, 650 and 850 mAh batteries 60
5.18 Design 2 including modules and hardware 61

6.1 CC-CV charging method (Battery University, 2018) 64
6.2 Overview of the charging setup 69
6.3 Transmitter datasheet revealing DC power connector polarity 70
6.4 Pictures from the experimental setup of the inductive charging solution . . 72

9.1 Gyroscope readings from flight #0 90
9.2 Gyroscope readings from flight #1 91
9.3 Frequencies of excessive noise from flight #1 92
9.4 Frequencies of excessive noise from flight #2 92
9.5 Gyroscope readings from flight #2 93
9.6 Gyroscope readings from flight #3 95
9.7 Pitch, roll and yaw step responses to current PID-values 97

10.1 Stress distributions (von Mises) in reduced weight frame 101
10.2 An alternative air duct concept 103
10.3 ”Proof” of the gyroscope-accelerometer dance theory 105

Abbreviations

ROV	=	Remotely Operated Vehicles
CNN	=	Convolutional Neural Network
VOC	=	Volatile Organic Compounds
UAV	=	Unmanned Aerial Vehicle
VIO	=	Visual-Inertial Odometry
TWR	=	Thrust to Weight Ratio
NRC	=	Noise Reduction Coefficient
STC	=	Sound Transmission Classification
DF	=	Discount Factor
EMF	=	Electromotive Force
CoG	=	Centre of Gravity
MCU	=	Microcontroller Unit
RPM	=	Revolutions Per Minute
ESC	=	Electronic Speed Controller
PWM	=	Pulse Width Modulation
BEC	=	Battery Elimination Circuit
FC	=	Flight Controller
UART	=	Universal Asynchronous Receiver/Transmitter
IMU	=	Inertial Measurement Unit
MPU	=	Motion Processing Unit
PPM	=	Pulse Position Modulation
PCB	=	Printed Circuit Board
(e)CO_2	=	(Estimated) Carbon Dioxide
TVOC	=	Total Volatile Organic Compounds
CC-CV	=	Constant Current - Constant Voltage
BMS	=	Battery Management System
GND	=	Ground (0 V)
CLI	=	Command Line Interface
TPA	=	Throttle PID Attenuation

Chapter 1

Introduction

While the word "drone" has a broad definition, it has, with a few exceptions, been used throughout this thesis to describe a remotely operated four-motor aerial vehicle. Some other terms found in other papers that may describe the same type of vehicle are "quad-copter" or "UAV".

1.1 The importance of indoor climate

Indoor climate is a product of a number of factors, such as temperature, humidity, CO_2, radon and more, and regulations on acceptable indoor climate conditions exist in order to ensure a safe and healthy working environment. Too poor of an indoor climate over time may lead to temporary health issues such as tiredness, headaches and irritated throat (Helsedirektoratet). In more extreme cases people may suffer long term illness due to, for example, excessive radon levels or mold formation from too much humidity.

Healthy employees on fewer sick leaves is of clear advantage to the employer. In a 2015 report on the years 2008-2012 by *Arbeidstilsynet* (The Norwegian Labour Inspection Authority) on "likely cause of sickness in the workplace" a frequently reported cause was 'physical conditions', or indoor climate (Direktoratet for Arbeidstilsynet, 2015).
A less measurable advantage, and possibly more relevant to buildings with already 'sufficiently good indoor climate', is how the indoor climate affect those who do not fall ill enough to go on a sick leave. While these employees do continue to work, it will be at reduced efficiency, and, in fact, studies show that improving the indoor climate can increase productivity up to 10% (Wyon and Wargocki, 2013).
That leaves the question of "what financial motivation is there for spending money on an already sufficient ventilation system?". An American study found that doubling ventilation rates cost less than $40 per person per year, while increased productivity from better ventilation can be valued at $6,500 per person per year (Allen, 2017). A similar conclusion has been reached in another research presenting benefit-cost ratios ("productivity benefit divided by costs of energy, equipment, and maintenance") up to 9.4 when increasing ven-

tilation rates (Berkely Lab). Improving indoor climate is therefore not just beneficial for the sake of the employee's health, but can also be financially viable and advantageous.

1.2 How indoor climate is monitored today

Today's buildings that monitor indoor climate often do this in a simple manner. Stationary sensors are placed in areas with some degree of air flow to measure simple environmental factors, while other factors are sampled and later analysed and evaluated in a lab.

Regulation of the indoor climate may then be done either *open loop* or *closed loop*. An example of open loop control is a window being opened by an employee when the indoor air starts feeling a little 'heavy'. The window is not closed again until new action is taken. A common closed loop indoor climate control is a thermostat. A desired temperature is set, and the room is heated until the desired temperature is reached, requiring no further action.
Some of today's regulation is open loop, and indoor climate in a building is monitored and regulated either in-house or in an off-site facility, based on readings from the stationary monitors. These monitors have limited coverage, and climate regulations are unlikely to be made until they report values approaching the limit for unacceptable climate values. Simultaneously, an area of the room that is not being monitored may already have passed this threshold. In other words, there is little to no understanding of how the indoor climate of each section relate to each other, and only monitored areas draw full advantage of climate regulation.
Another disadvantage of today's monitoring of the indoor climate is the fact that, as mentioned, some factors are analysed in a lab, rather than live. Regulations on the climate, based on lab analysis, can therefore be performed only much later than ideal. With more advanced sensors providing live analysis this issue can be avoided, but that brings us back to the first issue of today's indoor climate monitoring.

Simply put, one can say that today's solution is a reactive approach to the problem of poor indoor climate. This is most evident from the late responses to lab analysed factors, but also from the fact that some areas are not monitored. Poor climate conditions in one area will eventually propagate through a room, and will only be acted upon on a later time when picked up by a limited range stationary monitor. With the occasional poor indoor climate, the reactive approach may therefore cost the business hours of productivity.

1.3 The overall concept of a proactive approach by use of drone

To reduce lost hours of productivity a proactive approach can be imagined. Two simple reasons that "define" today's reactive indoor climate regulation are the mentioned lab analysed climate factors and limited coverage and understanding of indoor climate. While lab analysis can only be eliminated through sensors capable of live analysis, a drone is here suggested to eliminate, or reduce, the latter problem.

By copying the stationary sensors onto a drone you introduce mobility and the option to cover areas that are currently not monitored. One or several drones constantly moving around in a work environment might, however, introduce new problems, and so it could be difficult to directly transfer the working method of stationary monitors to a drone.
A drone may instead create an understanding of the indoor climate. This includes how conditions measured by one stationary monitor relate to the one on the other side of the room, and the area in between, or how the change in one measured parameter affect a different parameter. Through large amounts of data and smart algorithms one might be able to predict the effect of, for example, increasing ventilation rate in a room of certain geometry with a given live measurement of the current climate conditions.

The concept of indoor climate monitoring by drone may involve one or several drones operating in the same room/building, mapping environmental conditions. All data gathered on the indoor conditions needs to be linked to the position of the drone at the moment data is recorded, and relative positioning of the drone is therefore necessary. Proper drone infrastructure, such as communication and charging possibilities, is provided through one or several *docking stations*. In addition to communication and providing a standby charging dock for the drone(s), the docking station also acts as a link between drone and human. Data gathered by the drone is communicated to the docking station, through radio or any other means of communication. The docking station can then, by use of WiFi, relay data to a cloud. Data is further accessed by anyone with cloud access for analysis and presentation, either in raw format or through a user friendly interface. An illustration of the information flow is seen in figure 1.1.

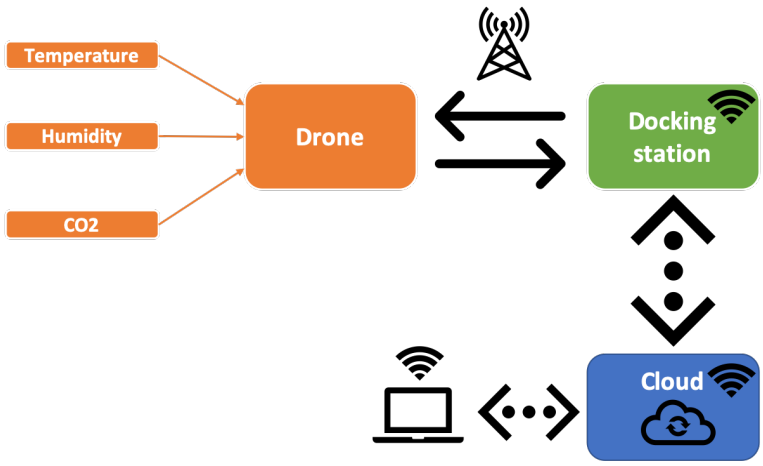

Figure 1.1: Illustration of information flow in the overall concept

1.3.1 Autonomous flight and measurements

Basis for a proactive approach to the issue of poor indoor climate has now been imagined. For efficient use of the drone one would require some degree of autonomy. Six levels of autonomy have been defined for vehicles, where 0 equals no autonomy and a level 5 vehicle is fully autonomous. Level 4, *high automation*, is the point where driver presence is no longer required. If imagined transferred to a drone, level 4 is the minimum level of autonomy that should be aimed for in this case. What differs level 5 autonomous vehicles from level 4 is that level 4 cars do not allow autonomous driving in more hazardous conditions, such as snow or rain (Hendrickson, 2020). While challenging weather conditions do not exist indoors, the presence of other humans during drone operations pose an increasing risk. A level 5 autonomous drone may therefore be thought of as a drone that can operate safely and with high confidence in an environment where other human's presence introduce a degree of uncertainty.

Three elements are imagined required for the autonomous functioning of the drone:

- Follow generated flight route autonomously
- Measure indoor climate parameters and transfer to a cloud autonomously
- Dock, charge and prepare for new mission autonomously

Two options for executing a mission can be considered. The first option is uploading and storing flight instructions on board the drone while docked. Environmental sensors then sample and store measurements during flight in the drone. When returning and docking once again sensor measurements are uploaded to a cloud for presentation and analysis. Upon complete autonomous re-charge the drone is ready to repeat the same procedure for a new mission.
A simple flowchart for a drone with on-board mission processing is shown in figure 1.2.

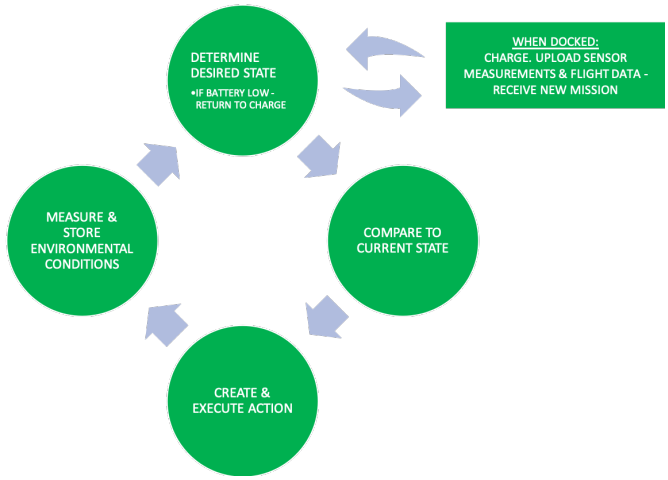

Figure 1.2: Flowchart of on-board mission processing

”Desired state” is, in simplified terms, the desired location of the drone, according to the current mission. As seen the docking station is not involved in the process at all, unless the drone is docked. The main advantage of this option is that the drone can operate outside communication range of the docking station, and does not suffer from communication latency. On the negative side, there will be greater requirements for drone hardware, as extra computational power is required for on-board calculation of action. Additional storage is also necessary in order to store sensor and flight data, as well as the mission itself. There is also no option to monitor sensor or flight data live.

The other option involves the docking station to a much greater extent, with continuous drone-docking station communication. Live measured environmental data and the current state of the drone are continuously communicated to the docking station. Current state is compared to the desired state according to the mission in the docking station, and a command is passed to the drone.
A flowchart for this option is seen in figure 1.3, with green circles representing the drone perspective and blue the docking station perspective.

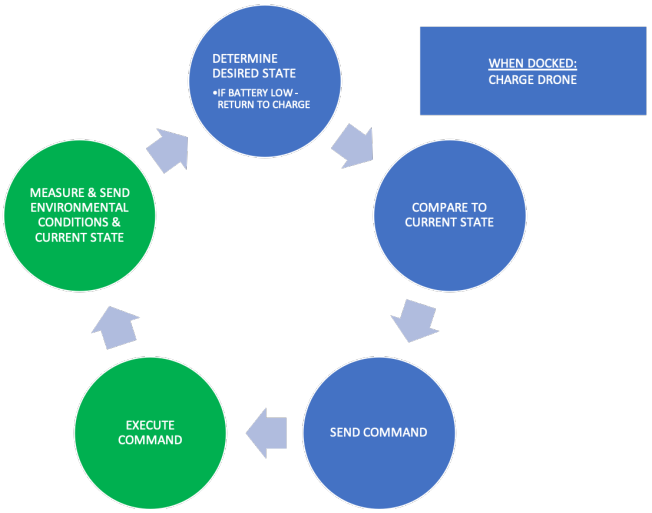

Figure 1.3: Flowchart of off-board mission processing

The docking station is now involved to a much greater extent and the drone is ”dumbed down”. This allows for live updates on the whereabouts of the drone as well as sensor data. Less computational power and little to no storage is required on-board, resulting in reduced weight. Naturally, it lacks that advantage of the other option - the possibility of flying out of range.

Means of autonomous flying has not been taken into further consideration, and so that is still open for evaluation. Combinations of the two options swiftly described above, or a completely different approach, is still possible.
One element of autonomy that has been researched is the means of achieving autonomous

charging. This is further discussed in chapter 6.

1.3.2 Advantages and applications

Based on the descriptions of today's solution on indoor climate monitoring and the drone solution, on can deduct the following long term advantages of introducing drones to the problem:

- A better understanding of how relevant factors for indoor climate relate
- Data to create a base layer for optimal control of existing indoor climate regulation systems
- Data to function as guidelines in optimal design of climate regulation systems in new buildings
- Improved indoor climate to increase workers efficiency and satisfaction

The combination of optimal climate regulation and increased employee efficiency and health will also be of great financial benefit to the business/building owner.
From a business perspective one may also consider means of making revenue from the product itself. ROVs (*remotely operated vehicles*), the drone's "underwater sibling", have often been sold as a service-for-rent product in campaign-based operations. However, with *Industry 4.0* emerging, many businesses look to integrate more products into their own system as a permanent solution (Lu, 2017). Some service oriented business models that satisfy this, to various extents, are (Scibilia, 2019):

- Service and Support Contracts - The drone is sold along with warranty and in-house services
- Assisted Services - The drone is connected to the manufacturer's control center for advice on machine performance
- Machine-as-a-service - The drone is operated by the customer but owned by the manufacturer, responsible for maintenance

While the focus so far has been on drone use in office buildings, and will continue that way throughout the report, one might see the possibility to conduct similar operations in public buildings and private homes as well.

1.4 Existing solutions

To the best of knowledge no solutions to indoor climate monitoring by drone exist as of today. There are, however, examples of research that combine environmental sensors and drones.

A paper from the University of Helsinki presents a drone equipped with sensors to measure volatile organic compounds (VOCs) (Ruiz-Jimenez et al., 2019). The research took

more of a chemical approach, investigating the applicability for a drone to carry different types of sampling systems, rather than designing an autonomous sensor carrying drone, as is the overall concept of this project.

Similar examples exist, such as the fixed-wing solar powered UAV (*unmanned aerial vehicle*) measuring and 3D-mapping greenhouse gases (Malaver et al., 2015), the fixed-wing UAV and drone dust measurement comparison (Alvarado et al., 2015) or the autonomous E-drone (Environmental drone) for air pollution measurements (Rohi et al., 2019). Commercially available solutions can be found at for example Scentroid, providing sensors to be equipped on existing drones (Scentroid).

Common for all above mentioned examples is a fairly bulky and heavy construction, all weighing several kilos. The mentioned E-drone, with a number of sensors for measuring environmental conditions, comes fairly close to appear suitable for indoor climate monitoring. It does, however, suffer from the mentioned bulky construction, and, hence, a visual distraction, as well as being GPS dependant. Indoors, GPS service may not always be available or accurate enough.

1.4.1 State-of-the-art examples

When investigating state-of-the-art examples on drones it is hard not to mention the FLIR developed military grade *Black Hornet* (FLIR). Though it rather resembles a miniaturized helicopter than a drone, its performance shows the great potential in small remotely operated aerial vehicles. The Black Hornet 3 weighs less than 33 g and measures 168 mm in length, all while maintaining 25 minutes flight time at up to 2 km range and a live camera feed (FLIR). Created as a tool for stealthy military operations it is also designed not be noticed, both visually and audibly.

On the autonomy side of high performance drones, a team of researchers from ETH Zürich and the University of Bologna have come up with a low power and weight solution (Palossi et al., 2019). Utilising convolutional neural networks (CNN) and a low power image sensor for visual navigation, autonomy with on-board real-time computations on a 100 mm nano drone was achieved at only 64 mW power consumption. With the autonomy hardware weighing only 5 g this paper proved the feasibility of implementing autonomy on drones where weight and power consumption are critical factors.

The MIT project *Navion* may allow for even lighter, smaller and more power greedy constructions (Suleiman et al., 2019). A team of researchers have developed a microchip that takes inertial measurements and mono/stereo images in a visual-inertial odometry (VIO) algorithm to both map an area and localize the drone's trajectory. While VIO is not a recent method for mapping and localization, the MIT created chip manages to do this while consuming as little as 2 mW of power. The chip itself measures no more than 4x5 mm, and is therefore far from dominant in a drone. However, as the previously mentioned ETH Zürich/University of Bologna researchers point out, the microchip alone is not sufficient for autonomous flying since additional components and circuity would be required (Palossi et al., 2019).

1.5 Aims for the project

The ideal long-term aim for the indoor climate monitoring drone is a compromise between the lightweight, autonomous state-of-the-art examples and the currently existing solutions, modified to suit the earlier discussed applications.
In this thesis the following goals have been set:

- Design and create a prototype frame for a indoor climate monitoring drone
  - Design with future implementation of autonomy hardware in mind
  - Create room for a set of essential sensors for indoor climate monitoring, more suitable than the presented existing solutions
  - Ensure means of air supply/sampling to the sensors
- Evaluate and select hardware for a prototype construction
- Design and test a charging solution that satisfies future requirements for autonomous operations
- Tune and test the drone to satisfactory performance
- Test and verify sensor air supply works as intended

Chapter 2

Basic Theory

Some basic theory was required in the process of designing the drone. For a better design it is beneficial to understand the behaviour of the drone components as well as the drone itself. Following are therefore theoretical approaches to the essential features of the drone.

2.1 Thrust to Weight Ratio

Thrust to Weight Ratio (TWR) is a simple unitless term describing the ratio of thrust produced by the motors to the weight of the drone. The TWR is given by equation (2.1), and may either be calculated for the drone as a whole, or for each motor.

$$TWR = \frac{T_m}{W_d/4} \tag{2.1}$$

Here, T_m (N) is the thrust of a single motor and $W_d/4$ (N) is the drone weight equally divided by four motors.
In order to be able to take off the drone needs a TWR greater than one, as this is the thrust required in order to overcome the gravitational forces experienced on the drone. It is, however, recommended that TWR is *at least* 2, both to compensate for the reduced vertical thrust when flying at an angle and for improved flight performance with some level of acceleration (Drone Omega).

2.2 Shroud design

The shrouds on a drone have three main purposes:

- Protection for both propellers and the surroundings
- Noise reduction
- Increase thrust

2.2.1 Protective shrouds

The protective quality of shrouds is simply the physical barrier they create between propellers and the surroundings. This is a two-way protective feature, meaning that propellers (and motors) are protected from surroundings in a crash, while surroundings are protected from hazardous rotating propellers.
Unless the shrouds are manufactured in a brittle material that may shatter and spread with the rotating propeller like grenade splints in a crash, there are no drawbacks, protection wise, with using shrouds.

2.2.2 Noise reducing shrouds

The noise reduction one can achieve with the use of shrouds depend much upon their material and shape.
Noise from drones mainly come from the high speed rotating propellers. This noise travels through air, before hitting the shrouds. This is the first step of noise reduction. Some materials will more or less let the noise waves fully pass or reflect, while others will add a level of absorption and damping, much like sound isolating material used in houses. Dotterel Technologies are a leading company on noise reducing shrouds, much thanks to the acoustic nano material they use (Dotterel Technologies). Acoustic materials are either absorbing, barriers or composite.
Absorbing materials simply absorb noise, and may come in the shape of *acoustic foam* or *acoustical absorption blankets*. These materials are rated with an *NRC* number (*Noise Reduction Coefficient*), where higher rated materials provide better absorption (Noise Control Specialist).
Barrier's, or noise barriers, sole purpose are to prevent noise transmission from one zone to another. Examples of noise barriers are *acoustical Barrier Blankets* or *ceiling barriers*. Noise barriers are, similarly to absorbing materials, rated with an *STC* number (*Sound Transmission Classification*), where higher numbers indicate more efficient noise barriers (Noise Control Specialist).
Composite materials are basically a combination of absorbing materials and noise barriers, providing the qualities of both. These are therefore rated with both an NRC and STC number (Noise Control Specialist).

The second step in noise reduction is a matter of shroud design. A quick search on Google Images for *drone shrouds* yield numerous pictures of similarly shaped shrouds. They stay fairly narrow at the bottom, but opens up at the top. The basic idea behind this is to direct any noise that is not absorbed in the material upwards, limiting the amount of noise that reach humans on the ground. In an indoor environment this means that the ceiling must have noise absorbing qualities.

By combining well suited, noise reducing materials and well designed shrouds, Dotterel Technologies have achieved a 6 dB noise reduction, with hopes of later doubling the *experienced* distance, sound wise, between you and the drone (The Revolutionaries, 2016).

2.2.3 Thrust increasing shrouds

Much like with noise reduction the increase of thrust lays in the shape of the shroud. There is, however, no need to guide the thrust downward, as this is already forced by the propeller, but rather *concentrate* it. Much of the concept can be explained with the basic equation for *flow rate*, *Q* (m^3/s), in equation (2.2):

$$Q = A * v \tag{2.2}$$

where *A* (m^2) is the area the air flows through and *v* (m/s) is the velocity of the air.
A rotating propeller moves air at a certain flow rate, pushing it into the area beneath the propeller. With no shrouds present this area is in theory more or less "*infinite*", but in practice just *large*, or a little larger than the working area of the propellers. Rearranging equation (2.2) to determine *v*, it becomes apparent that a "large *A*" will produce a "small *v*". As one can experience simply by blowing on your hand, "small v" equals "small force".
With the help of shrouds the area beneath the propellers can be reduced and constricted, giving a larger velocity, and, thus, more thrust without increasing the flow rate. It is not unrealistic to expect a 50% increase in thrust with the use of shrouds (Hrishikeshavan and Chopra, 2012). It must, however, be noted that shrouds are normally fairly large and dominant components that increase drone weight, and so the gained thrust must be weighed up against increased drone weight.

2.3 Propeller air flow

A part of the project involves exploring the use of air ducts taking in air flow generated by the propellers and exiting it into a sensor chamber, as further explained in chapter 5. It was therefore useful to study the air flow generated by the rotating propellers.
In basic terms, a propeller takes air from above and accelerates it in order to generate thrust. The thrust generated will depend on several qualities in the propeller and motor, but an approximation can be found with base in the momentum theory as shown by equation (2.3)(Hepperle, 1997)

$$T_m = \frac{\pi}{4} * D^2 * (v + \frac{\Delta v}{2}) * \rho * \Delta v \tag{2.3}$$

where *D* is the propeller diameter (*m*), *v* the velocity of incoming flow (*m/s*), Δv the additional velocity created by the propeller (*m/s*) and ρ the density of the fluid (kg/m^2).
To solve the equation for Δv one can write the equation out to become a second order equation, shown below in equation (2.4)

$$\underbrace{1}_{a}\Delta v^2 + \underbrace{2v}_{b}\Delta v \underbrace{- \frac{8T_m}{\pi D^2 \rho}}_{c} = 0 \tag{2.4}$$

Solving for Δv

$$\begin{aligned}\frac{-b \pm \sqrt{b^2 - 4ac}}{2a} = \frac{-2v \pm \sqrt{4v^2 - 4(-\frac{8T_m}{\pi D^2 \rho})}}{2} = \frac{-2v \pm 2\sqrt{v^2 + \frac{8T_m}{\pi D^2 \rho}}}{2} \\ = -v + \sqrt{v^2 + \frac{8T_m}{\pi D^2 \rho}} = \Delta v\end{aligned} \tag{2.5}$$

Note that the "$\pm$" is simplified to a "$+$" as the direction of thrust and Δv are defined as the same, and an increase in thrust should *always* increase Δv.
If the drone is just hovering and there is no incoming air, then v in equation (2.5) is set equal to zero. This yields a simpler equation for Δv, equation (2.6)

$$\Delta v = \sqrt{\frac{8T_m}{\pi D^2 \rho}} \tag{2.6}$$

In this case, the thrust generated by each motor in a quadcopter is given by Newton's second law of motion, equation (2.7)

$$T_m = \frac{m_d}{4} * a \tag{2.7}$$

where m_d is the mass of the drone (kg), $\frac{m_d}{4}$ is the drone mass carried by each motor individually (assuming weight evenly distributed to all motors) and a is the acceleration.
One may also give the thrust in terms of TWR with a re-arranged equation (2.1)

$$T_m = TWR * W_d/4 \tag{2.8}$$

The equations described above suggest that the air velocity is uniformly distributed across the full area underneath the propellers. This is, however, not the case. There are numerous examples of propeller simulations available online, such as in one report on *Reverse Engineering and CFD analysis on propeller* (Uthira Kumar et al., 2017). This study had the luxury of scanning a propeller to create a 3D-model of it, before simulating the air flow for a given rotational speed of the propeller. Simulation results, shown in figure 2.1, show fairly large variations in air velocity in the area underneath the propeller (red $\approx$ 10 m/s, green $\approx$ 6 m/s).

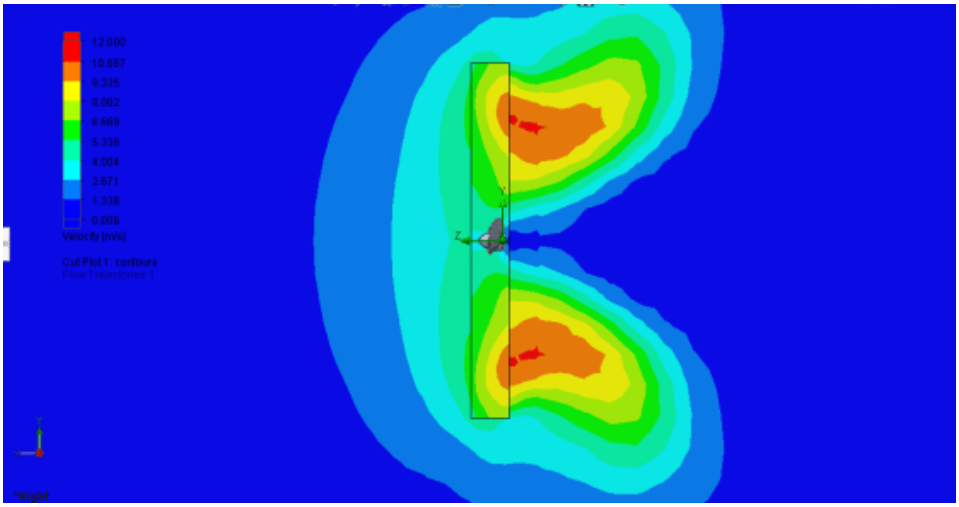

Figure 2.1: Air flow simulation of a 3D-scanned propeller (Uthira Kumar et al., 2017)

The simulation, using a 9 inch (228.6 mm) propeller rotating at 5000 rpm, found a maximum air velocity of 10.618 m/s and a maximum thrust of 2.029 N. By inserting the thrust results and the propeller diameter into equation (2.6), one might be able approximate which colour coded section of the air flow this equation gives the velocity for.

$$\Delta v = \sqrt{\frac{8T_m}{\pi D^2 \rho}} = \sqrt{\frac{8 * 2.029N}{\pi * (0.2286m)^2 * 1.225kg/m^3}} = 8.98m/s \tag{2.9}$$

According to the simulation results this equals the velocity in the border of the yellow/orange region. Closer to the outer ends of the propeller radius the velocity will therefore be less than this. The same goes for the air located further down the air stream. If one is interested in, for example, the green area (air velocity $\approx$ 6 m/s), one could discount the calculated air velocity with a *discount factor* (DF) of approximately $\frac{6m/s}{9m/s} = 0.67$. Note that these numbers are very approximated, and not as reliable as a proper simulation or experimental approach. The effects of shrouds, propeller shape or other factors have not been taken into account. It is, however, clear from the simulation results that air velocity vary underneath the propeller, and that anything near the edge of the propeller radius will not experience the full velocity of the generated air flow. It even seems likely that this velocity is less than what is calculated using equation (2.6).

2.4 Power consumption

Calculating power consumption can help estimate expected flight time, and there are several ways of approaching this problem.

The mechanical output power, i.e. the power that keeps the drone flying, is equal to battery power input, minus losses, and may be described as following:

$$P_{mech} = P_{el} - P_{EMF} - P_{iron} - P_{copper}$$

where P_{el} = battery input power, P_{EMF} = back EMF (back electromotive force) losses, P_{iron} = motor iron losses and P_{copper} = motor copper losses.
The relation between motor power and input power, i.e. the *motor efficiency*, is given by equation (2.10):

$$\eta_{motor} = \frac{P_{mech}}{P_{el}} \tag{2.10}$$

For a given motor efficiency electrical input power is given by

$$P_{el} = N_m \frac{P_{mech}}{\eta_{motor}} = V_{nom} I_{in} \tag{2.11}$$

with N_m being the number of motors, V_{nom} the rated nominal battery voltage and I_{in} battery current output.
And total current consumption:

$$I_{in} = \frac{P_{el}}{V_{nom}} \tag{2.12}$$

In other words, knowing P_{mech} and η_{motor} is enough to estimate P_{el} and, hence, flight time for a given battery. While η_{motor} may be available from the supplier, P_{mech} should be calculated.

2.4.1 Method 1

One way of calculating P_{mech} has already been partially derived when finding Δv.
Assuming no incoming air, the air velocity, v_{air}, equals 0 'far' above the propeller, accelerated to $\Delta v/2$ at the propeller, and fully accelerated to Δv underneath. The mechanical power, or *work*, at the propeller generating a thrust T_m then becomes

$$P_{mech} = F * d/t = T_m \frac{\Delta v}{2} \tag{2.13}$$

The method takes drone mass, propeller diameter and air density into account, but fails to include other factors, such as propeller pitch, number of blades, several efficiencies and more. It may, however, be sufficient for a rough and simple estimate of the power consumption in a drone at a hovering point, with just a few basic parameters at hand. With P_{mech} determined, the power consumption can be estimated for N_m motors with a given efficiency (assuming the motors operate at a constant efficiency). It is, however, normal that batteries do not drain a full 100%, but rather around 80%, and so this needs to be taken into account. Estimated flight time, T_{flight}, in minutes then becomes:

$$T_{flight}(s) = \frac{0.8 * \text{Battery capacity}(Ah) * V_{nom}}{P_{el}(W)} * 60 \tag{2.14}$$

Note that the method is only valid for drones at hover, i.e. a TWR of 1.

2.4.2 Method 2

Another method of estimating flight time is by looking at a known motor efficiency in terms of grams lifted per watt consumed, $\eta_{g/W}$. Power consumption is then given as

$$P_{el} = \frac{m_d}{\eta_{g/W}} \tag{2.15}$$

while current consumption and flight time is found using equations (2.12) and (2.14), respectively.
The advantage of this method is that it 'passively' incorporates any losses in the motor as well as propeller parameters. On the downside it requires a physical thrust test of the motor. The results are then valid for the parameters of the propeller(s) tested.

A comparison between the two methods for a range of drone masses are shown, as an example, in figure 2.2.
Parameters used are the following:

- V_{nom} = 11.1 V (3S LiPo, more information in chapter 4)
- Battery capacity = 0.5 Ah
- D = 2.5" (0.0635 m)
- ρ = 1.225 kg/m^3
- η_{motor} = 0.5 (set low to compensate for the lack of data on losses in the motor)
- N_m = 4
- $\eta_{g/W}$ = 3 g/W

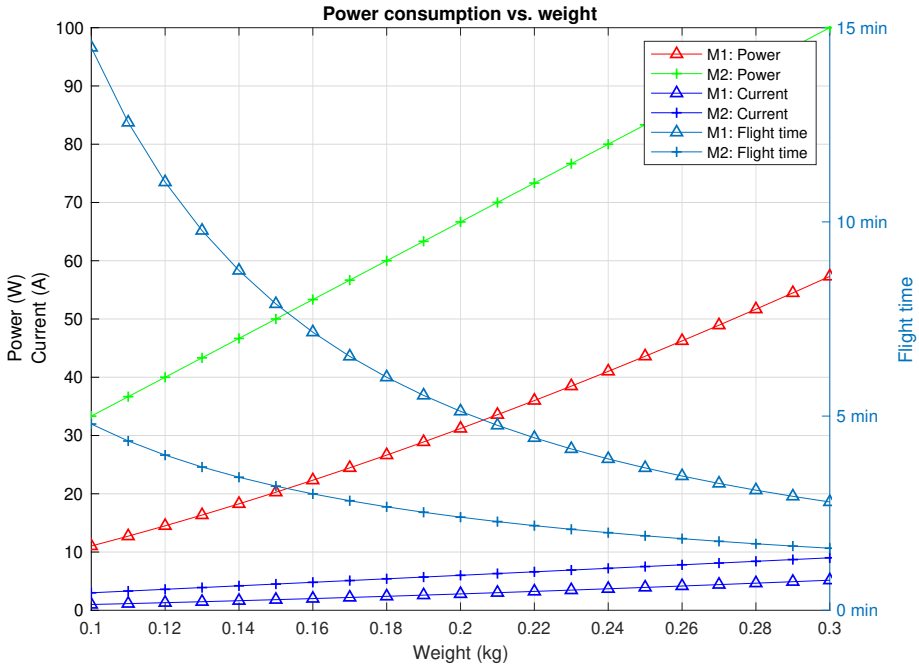

Figure 2.2: Comparison plots of the two methods. M1, M2 = Method 1, 2

The two methods are not really comparable at this point as some random values have been chosen. In this case, however, one can observe a more pessimistic flight time from the second method, while the first method has a steeper decline with increased weight.

2.5 Flow in air ducts

As previously mentioned, it is desirable to explore the use of air ducts to guide air from the propellers to a sensor chamber. The basic working of the ducts is that air enters the inlet with area A_1 (m^2) at velocity v_1 (m/s) and flow rate Q (m^3/s), with the relation earlier described in equation (2.2). The air flows through the duct at the same flow rate, but exits at the outlet of area A_2, into the chamber, at velocity v_2.
An expression for v_2 can then be derived with base in equation (2.2), as shown in equation (2.16)

$$Q = A_1 * v_1 = A_2 * v_2 \rightarrow v_2 = \frac{A_1}{A_2} * v_1 \tag{2.16}$$

The inlet and outlet areas, A_1 and A_2, respectively, are a matter of design. The inlet velocity may be assumed to be the same as the air velocity generated by the propellers, plus any additional incoming air, as described in equation (2.5) and (2.6), but with a discount factor *DF*.

Combining equations (2.6) and (2.16) (where $\Delta v = v_1$), with the discount factor, gives a general equation, equation (2.17), for the velocity of the air entering the sensor chamber, as well as the flow rate.

$$v_2 = \frac{A_1}{A_2} * DF\sqrt{\frac{8T_m}{\pi D^2 \rho}} \tag{2.17a}$$

$$Q = A_1 * DF\sqrt{\frac{8T_m}{\pi D^2 \rho}} = A_2 * v_2 \tag{2.17b}$$

Note that this equation assumes no additional incoming air, which may be considered a reasonable assumption and simplification for a drone hovering or flying at low speed in surroundings with still standing air. For a moving drone with incoming air equation (2.5) is used instead of (2.6).

2.6 Drone equations of motion

While many drone hobbyists tune their drone with an experimental approach, a mathematically designed PID regulator may speed up the process of getting the ideal drone behaviour. This require equations of motion for the drone, as well as an understanding of how a PID regulator works.

2.6.1 PID regulator

A basic system with a PID controller is seen in figure 2.3, with a detailed block diagram of the PID regulator itself at the bottom. In the figure, *r(t)* is the desired state command, *e(t)* the error, or difference, between desired state and actual state of the system, *u(t)* the PID regulated plant input command and *y(t)* the actual, or measured, state of the system. *u(t)* is given by equation (2.18) below:

$$u(t) = K_p e(t) + K_i \int_0^t e(\tau)d\tau + K_d \frac{d}{dt}e(t) \tag{2.18}$$

Using Laplace transformation to find the transfer function of the PID regulator:

$$\begin{aligned} \mathcal{L}\{u(s)\} = \mathcal{L}\{K_p e(t) + K_i \int e(t)dt + K_d \frac{d}{dt}e(t)\} \\ \rightarrow \frac{u(s)}{e(s)} = \frac{K_d s^2 + K_p s + K_i}{s} \end{aligned} \tag{2.19}$$

where $e(s) = r(s) - y(s)$.

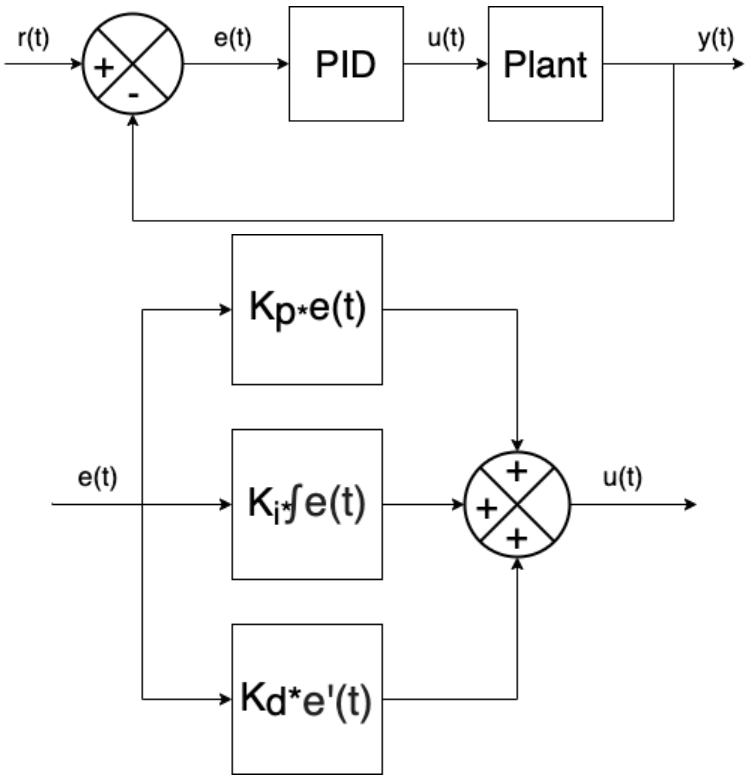

Figure 2.3: PID regulated system

2.6.2 Equations of motion

Now that one has the transfer function for the PID regulator derived the same is necessary for the plant (drone). Step one is finding its *equations of motion*. This process involves a number of steps, but the equations can be found readily derived online. As there is no focus on designing the system from scratch not all parts of the process in getting to the equations will be thoroughly detailed.

The motors are what move and rotate the drone, and therefore a good starting point in modelling its dynamics. We here assume a quad-copter in an X-configuration, with x, y and z axes and motor directions as shown in figure 2.4

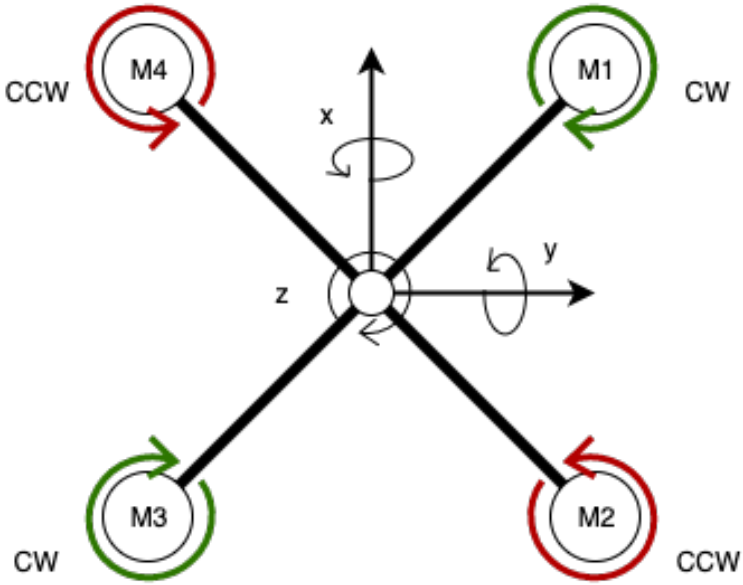

Figure 2.4: General layout of drone workings

Thrust (vertical movement), roll (ϕ, rotation about the x-axis) pitch (θ, rotation about the y-axis) and yaw (ψ, rotation about the z-axis) is created by increasing and reducing power to the right combination of motors. Assuming positive motor force is upward, thrust (F) and torques (τ) according to above mentioned motions are given by the following equations:

$$F_{pr} = F_{M1} + F_{M2} + F_{M3} + F_{M4} \tag{2.20a}$$
$$\tau_{\phi} = l(-F_{M1} - F_{M2} + F_{M3} + F_{M4}) \tag{2.20b}$$
$$\tau_{\theta} = l(F_{M1} - F_{M2} - F_{M3} + F_{M4}) \tag{2.20c}$$
$$\tau_{\psi} = l(-F_{M1} + F_{M2} - F_{M3} + F_{M4}) \tag{2.20d}$$

The l is the length between the motors and the centre of gravity (CoG), as this is the point the drone will rotate about ($Torque(Nm) = Force(N) * length(m)$). Note that the above equations assume equal distance to the CoG for all motors.
Equation (2.20a) is fairly self explanatory, as it describes a simultaneously generated balanced lift on all four corners of the drone. Equations (2.20b) and (2.20c) describe an imbalance about the x- and y-axes, respectively, ultimately tilting the drone to either roll or pitch. Equation (2.20d) manages to avoid imbalance about the x- and y-axis, as well as maintaining the sum of upward thrust at zero (to avoid vertical movement), and rather rotates about the z-axis.
Further on, we define a earth-fixed frame and a body-fixed frame. The earth-fixed frame is locked from drone rotation and movement with constant direction of the axes, while the body-fixed frame follows the rotation and movements of the drone. An illustration can be

seen in figure 2.5.

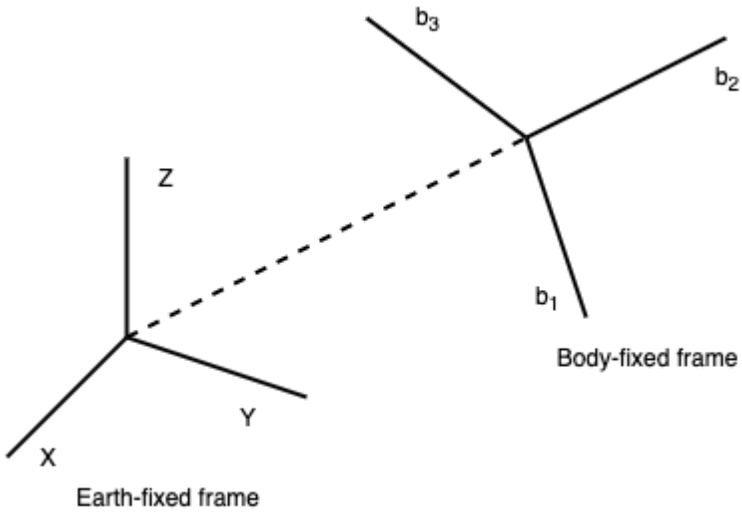

Figure 2.5: Illustration of an earth-fixed frame and body-fixed frame

Some body-fixed frame definitions are given below (Charlie, 2017):

$$\mathbf{v}^b = \begin{bmatrix} u \\ v \\ w \end{bmatrix}$$

Linear velocity (2.21a)

$$\boldsymbol{\omega} = \begin{bmatrix} p \\ q \\ r \end{bmatrix} = \begin{bmatrix} \dot{\phi} \\ \dot{\theta} \\ \dot{\psi} \end{bmatrix}$$

Angular velocity (2.21b)

In addition, the following is used to describe the forces and moment acting on the drone (Charlie, 2017):

$$\text{Force} = \begin{bmatrix} F_x \\ F_y \\ F_z \end{bmatrix} \tag{2.22a}$$

$$\text{Moment} = \begin{bmatrix} \tau_\phi \\ \tau_\theta \\ \tau_\psi \end{bmatrix} \tag{2.22b}$$

The derivation of equations of motion heavily relies on Newton's second law of motion. While many are familiar with the linear version of this, the angular version is less familiar.

Both are given in equation (2.23) (Charlie, 2017).

$$\mathbf{F} = m\boldsymbol{a} \tag{2.23a}$$

$$\mathbf{M} = \mathbf{I}\boldsymbol{\Omega} \tag{2.23b}$$

Here, **F** is the force vector (2.22a), *m* the mass of the drone, **a** the acceleration vector, **M** the moment vector (2.22b), **I** the inertia matrix of the drone and $\boldsymbol{\Omega}$ the angular acceleration. The inertia matrix can, assuming a perfectly symmetric drone, be given as (Charlie, 2017):

$$\mathbf{I} = \begin{bmatrix} I_{xx} & 0 & 0 \\ 0 & I_{yy} & 0 \\ 0 & 0 & I_{zz} \end{bmatrix}$$

The gravitational forces acting on the drone in the earth-fixed frame is simply given as below (positive direction down)

$$\mathbf{F}_{gr}^{e} = \begin{bmatrix} 0 \\ 0 \\ mg \end{bmatrix}$$

with superscript *e* indicating it is defined in the earth-fixed frame. To translate this to the body-fixed frame the *Euler angle transformation matrix*, $\mathbf{C}_e^b$, is used (Charlie, 2017). Subscript and superscript, *e* and *b*, respectively, indicate translation from the earth-fixed to the body-fixed frame.

$$\mathbf{F}_{gr}^{b} = \mathbf{C}_e^b \mathbf{F}_{gr}^{e} =$$

$$\begin{bmatrix} cos\theta cos\psi & cos\theta sin\psi & -sin\theta \\ -cos\theta sin\psi + sin\phi sin\theta cos\psi & cos\phi cos\psi + sin\phi sin\theta sin\psi & sin\phi cos\theta \\ sin\phi sin\psi + cos\phi sin\theta cos\psi & -sin\phi cos\psi + cos\phi sin\theta sin\psi & cos\phi cos\theta \end{bmatrix} \begin{bmatrix} 0 \\ 0 \\ mg \end{bmatrix}$$

$$= \begin{bmatrix} -mgsin(\theta) \\ mgsin(\phi)cos(\theta) \\ mgcos(\phi)cos(\theta) \end{bmatrix}$$

In addition to gravitational forces, the force from the propellers will act on the drone. These were given in equation (2.20a) as a scalar, and are already in the body-fixed frame. In vector form propeller force is given as $\mathbf{F} = [0\ 0\ F_{m1} + F_{m2} + F_{m3} + F_{m4}]^T$. Applying Newton's second law of motion:

$$\begin{aligned} \sum \mathbf{F} = m\boldsymbol{a} \rightarrow \mathbf{F}_{gr}^{b} - \mathbf{F}_{pr} = m\dot{\mathbf{v}}_{\mathbf{e}}^{\mathbf{b}} \\ \rightarrow \begin{bmatrix} -mgsin(\theta) \\ mgsin(\phi)cos(\theta) \\ mgcos(\phi)cos(\theta) - \sum_{i=1}^{4} F_{mi} \end{bmatrix} = m\dot{\mathbf{v}}_{\mathbf{e}}^{\mathbf{b}} \end{aligned} \tag{2.24}$$

$\dot{\mathbf{v}}_e^b$ is found based on *Coriolis theorem* (Charlie, 2017):

$$\dot{\mathbf{v}}_e^b = \dot{\mathbf{v}}_e^b + \dot{\boldsymbol{\omega}}_{\boldsymbol{e}}^{\boldsymbol{b}} \times \mathbf{v}_e^b \tag{2.25}$$

where $\dot{\boldsymbol{\omega}}_{\boldsymbol{e}}^{\boldsymbol{b}}\times$ is simply a skew-symmetric cross-product matrix (Charlie, 2017):

$$\dot{\boldsymbol{\omega}}_{\boldsymbol{e}}^{\boldsymbol{b}}\times = \begin{bmatrix} p \\ q \\ r \end{bmatrix}_{\times} = \begin{bmatrix} 0 & -r & q \\ r & 0 & -p \\ -q & p & 0 \end{bmatrix}$$

Inserting to equation (2.25):

$$\dot{\mathbf{v}}_e^b = \begin{bmatrix} \dot{u} \\ \dot{v} \\ \dot{w} \end{bmatrix}^b + \begin{bmatrix} 0 & -r & q \\ r & 0 & -p \\ -q & p & 0 \end{bmatrix} \begin{bmatrix} u \\ v \\ w \end{bmatrix}^b = \begin{bmatrix} \dot{u} + qw - rv \\ \dot{v} + ru - pw \\ \dot{w} + pv - qu \end{bmatrix} \tag{2.26}$$

Finally, inserting into equation (2.24):

$$\begin{bmatrix} -mgsin(\theta) \\ mgsin(\phi)cos(\theta) \\ mgcos(\phi)cos(\theta) - \sum_{i=1}^{4} F_{mi} \end{bmatrix} = m \begin{bmatrix} \dot{u} + qw - rv \\ \dot{v} + ru - pw \\ \dot{w} + pv - qu \end{bmatrix} \tag{2.27}$$

Next, a similar process is repeated for moment acting on the drone, with the assumption of no external moment. The Coriolis theorem now becomes:

$$\mathbf{M} = \mathbf{I}^b \dot{\boldsymbol{\omega}}_e^b + \boldsymbol{\omega}_e^b \times \mathbf{I}^b \boldsymbol{\omega}_e^b \tag{2.28}$$

With all components of this equation already described this yields the following:

$$\begin{aligned} \begin{bmatrix} \tau_\phi \\ \tau_\theta \\ \tau_\psi \end{bmatrix} &= \begin{bmatrix} I_{xx} & 0 & 0 \\ 0 & I_{yy} & 0 \\ 0 & 0 & I_{zz} \end{bmatrix} \begin{bmatrix} \dot{p} \\ \dot{q} \\ \dot{r} \end{bmatrix} + \begin{bmatrix} 0 & -r & q \\ r & 0 & -p \\ -q & p & 0 \end{bmatrix} \begin{bmatrix} I_{xx} & 0 & 0 \\ 0 & I_{yy} & 0 \\ 0 & 0 & I_{zz} \end{bmatrix} \begin{bmatrix} p \\ q \\ r \end{bmatrix} \\ &= \begin{bmatrix} I_{xx}\dot{p} \\ I_{yy}\dot{q} \\ I_{zz}\dot{r} \end{bmatrix} + \begin{bmatrix} (I_{zz} - I_{yy})qr \\ (I_{xx} - I_{zz})pr \\ (I_{yy} - I_{xx})pq \end{bmatrix} \end{aligned} \tag{2.29}$$

The equations of motion derived from force and moment are, thus, the following:

$$\dot{u} = -gsin(\theta) + rv - qw \tag{2.30a}$$

$$\dot{v} = gsin(\phi)cos(\theta) + pw - ru \tag{2.30b}$$

$$\dot{w} = gcos(\phi)cos(\theta) - \frac{F_{pr}}{m} + qu - pv \tag{2.30c}$$

$$\dot{p} = \frac{\tau_\phi - (I_{zz} - I_{yy})qr}{I_{xx}} \tag{2.30d}$$

$$\dot{q} = \frac{\tau_\theta - (I_{xx} - I_{zz})qr}{I_{yy}} \tag{2.30e}$$

$$\dot{r} = \frac{\tau_\psi - (I_{yy} - I_{xx})qr}{I_{zz}} \tag{2.30f}$$

Linearizing around an equilibrium of hovering, with small angle approximations ($sin(\theta) \approx \theta, cos(\theta) \approx 0$) and neglecting multiplications of small linear/angular velocities, give the

linearized equations of motion for altitude and attitude:

$$\dot{w} = \ddot{z} = g - \frac{F_{pr}}{m} \tag{2.31a}$$

$$\dot{p} = \ddot{\phi} = \frac{\tau_\phi}{I_{xx}} \tag{2.31b}$$

$$\dot{q} = \ddot{\theta} = \frac{\tau_\theta}{I_{yy}} \tag{2.31c}$$

$$\dot{r} = \ddot{\psi} = \frac{\tau_\psi}{I_{zz}} \tag{2.31d}$$

2.6.3 PID regulator design

Typical drone controllers control elevation rate (*w*), pitch (ϕ), roll (θ) and yaw rate (*r*). In the case of elevation and yaw it is therefore desirable to design controllers for their respective rates, rather than angle of rotation or position.
The above equations of motion transformed to the frequency domain using Laplace transformation (initial conditions = 0), with respect to the parameters of desired control, yield the following transfer functions:

$$\frac{w(s)}{-F_{pr}(s)} = \frac{1}{ms} \tag{2.32a}$$

$$\frac{\phi(s)}{\tau_\phi(s)} = \frac{1}{I_{xx}s^2} \tag{2.32b}$$

$$\frac{\theta(s)}{\tau_\theta(s)} = \frac{1}{I_{yy}s^2} \tag{2.32c}$$

$$\frac{r(s)}{\tau_\psi(s)} = \frac{1}{I_{zz}s} \tag{2.32d}$$

2.6.4

For further calculations on the PID regulator design the following is redefined to match labels in figure 2.3:

- $F_{pr}(s) \rightarrow \mathrm{u}_w(s)$, $w(s) \rightarrow \mathrm{y}_w(s)$
- τ_ϕ(s) $\rightarrow \mathrm{u}_\phi(s)$, $\phi(s) \rightarrow \mathrm{y}_\phi(s)$
- $\tau_\theta(s) \rightarrow \mathrm{u}_\theta(s)$, $\theta(s) \rightarrow \mathrm{y}_\theta(s)$
- $\tau_\psi(s) \rightarrow \mathrm{u}_\psi(s)$, $r(s) \rightarrow \mathrm{y}_r(s)$

An example of closed-loop transfer function calculation of a PID-controlled system is seen for pitch below, followed by the rest listed.

$$\begin{aligned}
\frac{u_\phi(s)}{r_\phi(s) - y_\phi(s)} = \frac{K_d s^2 + K_p s + K_i}{s} &\rightarrow \frac{I_{xx} s^2 y_\phi(s)}{r_\phi(s) - y_\phi(s)} = \frac{K_d s^2 + K_p s + K_i}{s} \\
&\rightarrow y_\phi(s) \frac{I_{xx} s^3 + K_d s^2 + K_p s + K_i}{s} = \frac{K_d s^2 + K_p s + K_i}{s} r_\phi(s) \\
&\rightarrow \frac{y_\phi(s)}{r_\phi(s)} = \frac{K_d s^2 + K_p s + K_i}{I_{xx} s^3 + K_d s^2 + K_p s + K_i} \\
&\rightarrow \frac{y_\phi(s)}{r_\phi(s)} = \frac{(K_d/I_{xx}) s^2 + (K_p/I_{xx}) s + K_i/I_{xx}}{s^3 + (K_d/I_{xx}) s^2 + (K_p/I_{xx}) s + K_i/I_{xx}}
\end{aligned} \tag{2.33}$$

And the remaining transfer functions:

$$\frac{y_w(s)}{r_w(s)} = \frac{K_d/(K_d + m) s^2 + K_p/(K_d + m) s + K_i/(K_d + m)}{s^2 + K_p/(K_d + m) s + K_i/(K_d + m)} \tag{2.34a}$$

$$\frac{y_\theta(s)}{r_\theta(s)} = \frac{(K_d/I_{yy}) s^2 + (K_p/I_{yy}) s + K_i/I_{yy}}{s^3 + (K_d/I_{yy}) s^2 + (K_p/I_{yy}) s + K_i/I_{yy}} \tag{2.34b}$$

$$\frac{y_r(s)}{r_r(s)} = \frac{(K_d/(I_{zz} + K_d)) s^2 + (K_p/(I_{zz} + K_d)) s + K_i/(I_{zz} + K_d)}{s^2 + (K_p/(I_{zz} + K_d)) s + K_i/(I_{zz} + K_d)} \tag{2.34c}$$

Chapter 3

Design Specifications

In the following chapters are details on selection of hardware, frame design and features, means of achieving autonomous charging, finalised by assembly and a set of experiments. The general target has been to construct a relatively lightweight drone, but with hardware and a frame design that allows for further experimentation, on for example autonomy, beyond the scope of this project.
The complete construction is shown in figure 3.1, and final specifications in table 3.1, with references to the related chapters of discussion.

Figure 3.1: The complete construction of the drone

Specification	Value	Chapter
GENERAL		
Frame material	PLA	7.0.1
Diameter (mm)	175	5.0.3
Height (mm)	33	5.0.3
Total weight (g, excl. battery)	151	8.1
HARDWARE		
Input voltage range (V, nominal)	7.4-14.8 (2-4S)	4 (4.7)
Input current limit (A)	35	4 (4.7)
FC MCU	STM32F722RET6, 216 MHz	4.4
FC communication protocol	PPM, Serial RX	4.4
ESC MCU	STM32PINF0, 32-bit	4.3
ESC communication protocol	Dshot, Proshot, Oneshot	4.3
IMU	MPU6000, ICM20602	4.4
Barometer	BMP280	4.4
Magnetometer	No	4.4
Telemetry	Yes	4.5.5
Current sensor	Yes	4.3
Voltage sensor	Yes	4.4
Blackbox	MicroSD-card	4.4
SOFTWARE		
FC software	Betaflight, iNav	4.4, 8
ESC software	BLHeli_32	4.3
POWER CONSUMPTION & FLIGHT TIME		
Theoretical power consumption (W)	65.46	5.0.3
Experimental power consumption (W)	61.24	9.4
Theoretical hover flight time (min.) (300 mAh battery)	$\sim$2.5	5.0.3
Theoretical hover flight time (min.) (550 mAh battery)	$\sim$4.0	5.0.3
Experimental hover flight time (min.) (300 mAh battery)	$\sim$2.25	9.4
CHARGING		
Charging method	Inductive (Wireless)	6.3
On-board weight (g)	$\sim$25	6 (6.4)
Charger power supply	Wall socket	6.3
Compatible battery voltages (V, nominal)	7.4, 11.1 (2S, 3S)	6.2
Charging current (A)	$<$0.8	6.2
SENSOR CHAMBER		
Weight (g, excl. sensors)	12.8	5.0.3
Sensor chamber dimensions (mm)	36x36.6x21	5.0.3
Inlet air flow rate (m^3/s)	1.2	5.0.3
Room for temperature sensor	Yes, Si7021	5.0.3

Continued on next page

Specification	Value	Chapter
Room for humidity sensor	Yes, Si7021	5.0.3
Room for pressure sensor	Yes, MPL115A2	5.0.3
Room for VOC sensor	Yes, CCS811	5.0.3
Room for eCO_2 sensor	Yes, CCS811	5.0.3
Room for CO_2 sensor	Yes, T6713	5.0.3
Room for dust sensor	No	5.0.3
AUTONOMY COMPATIBILITY		
LiDAR mounts	4	5.0.3
Room for larger hardware (mm)	97x97	5.0.3

Table 3.1: Drone design specifications

Chapter 4

Hardware

The hardware is a lot of what makes the drone, and is a major part of what differs a drone for photography from a racing drone. Further on are explanations of the essential hardware for the indoor climate monitoring drone in question, as well as choice of hardware with just reasoning.

4.1 Propellers

While the propellers on a drone are seemingly simple they hold some design qualities that define their attributes, and these are discussed further on.

4.1.1 Size

The size of the propeller, measured by its diameter, will define the minimum required drone size to fit two propellers comfortably next to each other. It can also be seen the other way around - that a set drone size limits the maximum propeller diameter.
Propeller diameter do not only make a large contribution on determining drone size, but also on flight performance. Larger propellers will have a greater surface area and are therefore capable of moving more air. Increased movement of air is directly linked to an increase in thrust. On the downside, pushing more air requires more energy. A larger diameter also means an increase in moment of inertia, and so larger propellers tend to respond slower to input changes compared to smaller propellers. This makes them less suitable for racing drones requiring sharp, fast response. Larger diameter propellers do, however, give a steadier flight experience.

Propeller size is normally given in inches, with common sizes ranging from 2” (50.8 mm) to 6” (152.4 mm), though both bigger and smaller sizes are available.

4.1.2 Pitch

The pitch of a propeller defines to what extent the blade has been twisted, and is commonly and most easily explained as ”how far forward that propeller would move in one revolution in a perfect world (neglecting drag and losses)” (GetFPV, 2018). A neat summary of low vs. high pitch propeller qualities are shown in table 4.1 below.

Quality	Low pitch	High pitch
Low-end torque	Higher	Lower
Thrust	Lower	Higher
Speed	Lower	Higher
Power consumption	Lower	Higher
Input response	Faster	Slower

Table 4.1: High and low pitch propeller qualities (GetFPV, 2018)

It is also important to remember that low pitch propellers are more efficient at low speeds, whereas high pitch propellers operate more efficiently at higher speeds (GetFPV, 2018).

As with propeller diameter pitch is also normally given in inches, with, generally, 3” pitch being considered low and 5” considered high.

4.1.3 Number of blades

The main reason for increasing the number of blades is to increase thrust. Logically, this comes at the cost of reduced efficiency, as more propellers will create more drag. If more thrust is necessary it is often preferable to increase diameter rather than number of blades, as size increase is more gentle on the efficiency.
Similar to increasing propeller size, more blades will increase moment of inertia and, hence, slow the input response but improve the experience of a steady flight.

Commonly, propellers come with either two, three or four blades.

4.1.4 Material

Propeller material can affect vibration and noise, as well as efficiency. Stiff propellers vibrate less and are more efficient as they do not bend. They are, however, more likely to shatter in a crash, and therefore considered somewhat of a hazard.

The vast majority of propellers today are made of *poly carbonate* or similar, and considered sufficient in most cases (GetFPV, 2018).

4.1.5 Blade tip

Even the tip of the propeller will have a say on the performance of the drone. There are three main types of propeller tips; pointy, bull nose and hybrid bull nose. A bull

nose propeller cuts the pointy tip and extends the a larger area to the full extent of the propeller's diameter. The increased surface area provides more thrust, but also increases power consumption. A hybrid bull nose is a compromise between the bull nose and the lower thrust, lower power consumption pointy tip option (Liang, 2017a).
As a final note, some propellers come with *wing tips* that are designed to reduce drag, and, hence, increase efficiency (GetFPV, 2018).

4.1.6 Selection of propellers

Propellers are fairly cheap, and should ideally be experienced rather than evaluated on a purely theoretical basis. Three different sets of propellers were therefore acquired. All three sets, apart from the third, are 2.5" diameter propellers made of poly carbonate.

Selected set #1: HQ Durable Prop T2.5X2.5X3 (Elefun, b)

This propeller is a three blade 2.5" pitch propeller with a hybrid bull nose tip. From the very low pitch one can expect good low end torque, low power consumption and fast response. The drawback of low pitch is reduced speed and thrust. Thrust is, however, improved with the blade tip finish and with three blades, rather than two.

Selected set #2: HQ Durable Prop T2.5X3.5X3 (Elefun, c)

This propeller is a three blade 3.5" pitch propeller with a hybrid bull nose tip. It is very similar to the first set of propellers, but the increased pitch will provide a little extra thrust and speed at the cost of higher power consumption.

Selected set #3: Gemfan Flash 2540 Durable 3-blade (GetFPV, b)

The third set of propellers is slightly smaller, 2.4", and has a higher pitch of 4". The most interesting part is the wing tipped finish on an otherwise standard hybrid bull nose tip. The fairly high pitch will provide the drone with more thrust and speed, but with slower response and higher power consumption. The wing tip may, however, help with the efficiency of the propeller.

4.2 Motors

Motors are rich in features, and may have immense variations from one brand to another, despite similar specifications. Following are some key specifications for motors, and a final set of selected motors for this drone. Specifications are only given for brushless motors, as brushed motors are rarely used in drones.

4.2.1 Thrust to Weight Ratio

Details on thrust to weight ratio were earlier explained in chapter 2.1.
Determining the TWR of the drone setup is very difficult without seeing a *thrust test* or similar for the motor, and it may vary with different sets of propellers and batteries.

4.2.2 kV-rating

The kV-rating is, as a rule of thumb, the RPM (revolutions per minute) of the motor per volt applied at no load. As a basic example, a 2000 kV motor will, at 12 volts, spin at 24000 RPM. What kV-rating to go with depends on the application and the propellers. Generally, low kV motors go with large propellers, allowing for slow, high torque rotation for a high payload. Likewise, high kV motors go better with smaller propellers on drones aiming for speed and acrobatics (Kadamatt, 2017).

The kV-ratings of motors commonly range from sub 2000 kV (even sub 1000 kV) in larger drones, to 16.000 kV (though over 20.000 kV is not a rare find either) in lighter racing drones. 4500, 6000, 8000 and 11.000 kV are probably the most frequently used ratings in basic hobbyist drones.

4.2.3 Stator size

Drone motors are in most cases named with a 2+2 four digit number, with the two first stating the stator width and the other two stator height. Taller stators are used to give more power at higher RPM, whereas wider stators improve torque at lower speed (Drone Omega). For this reason, the low kV motors carrying heavy payloads have very wide stators.
It is important to remember that increasing stator size increases drone weight, and so motors that are oversized for its application, ”just for the sake of it”, will be nothing but an efficiency reducing factor.

Common stator sizes for light weight drones are labelled 110X, 120X or 130X, with X often being in the range of 3 to 6. 150X can be used for larger and heavier setups. Both smaller and larger stators than these are available, with more extreme qualities in terms of either lifting capability or speed.

4.2.4 Selection of motors

Much more can be said about motor specifications, but the above give a solid base for matching a set of motors to an application.

Selected motors: EMAX RS1106II 4500kV (Elefun)

The stator size of the EMAX RS1106II 4500kV imply, with its relatively small width but larger height, slightly more focus on speed rather than torque. Based on the earlier

discussion on propellers it is reasonable to assume that these motors will work well with the high pitch Gemfan propellers. These motors also have the advantage of being lighter than the 120X and 130X motors, weighing in at roughly 7 grams. Lighter motors exist, but often at the cost of less torque or speed.
In terms of kV-rating it is too low to be a first pick for a racing drone, as it is aimed for carrying some load rather than performing acrobatic stunts.
The easiest method of determining the suitability of this motor would have been by looking at thrust tests. No thrust test for this particular motor was found, but there was one for its predecessor, the RS1106 4500kV. With a 3S battery the motor proved lifting capabilities of about 50 g while pulling 2 ampere, or up to 120 g at 5 ampere, depending on the propeller (fishpepper, 2017). This was considered sufficient, and there is also a chance that the newer version at hand will prove to be even better.
The motors may also perform well with a 4S battery.

4.3 ESC

The ESC is the component that powers the motors, though some also come with additional features. Following are critical specifications in an ESC, as well as some additional features and the ESC selected for this drone.

4.3.1 Single or 4-in-1 ESC

ESCs can be bought in singles for powering each their motor, or as a 4-in-1 solution where a single component powers all four motors. 4-in-1 ESCs are generally a lighter and more compact solution compared to four single ESCs. The drawback, however, is that if one of the motors were to pull too much current and damage the ESC the whole 4-in-1 component would have to be replaced.

4.3.2 Current rating

The current rating is given as both continuous and burst. Continuous current is how much current the ESC can handle continuously, while burst current is a higher current the ESC can handle for a limited time (typically around 10 seconds) before taking damage. Required current rating is heavily dependent on the motors, as these are the components that will pull the majority of current in the drone. Using an ESC with a current rating much larger than what the motors (and other components) require will, however, often add unnecessary weight to the drone.

4.3.3 Voltage rating

Just as ESCs are rated for a certain amount of current, they also come with a voltage rating denoting the input voltage from the battery they can handle. This is given as a number and the letter "*S*", with S being the voltage in a single LiPo-cell, 4.2V when fully charged (3.7V nominal voltage). A 3S rated ESC will therefore operate at $3 * 4.2V = 12.6V$. However,

ESCs often operate at voltage ranges, for example 2-4S, so that one is not constrained to using batteries of one particular voltage rating only.

4.3.4 Firmware

The firmware on an ESC is what determines the communication protocols on the ESC (see next section), and a way to access options for tuning ESC performance.
A few options are available, such as BLHeli (and BLHeli_S and BLHeli_32), SimonK and KISS, but in reality the majority of ESCs come with a version of BLHeli pre-installed. Looking for anything else than BLHeli will therefore drastically limit your options.
One of the advantages with BLHeli is its user-friendly interface and the fact that it is still being maintained and updated (unlike SimonK)(Liang, 2020a). The first generation of BLHeli was, simply, BLHeli, before being followed up by BLHeli_S and the latest BLHeli_32. While BLHeli_S was designed for Busybee processors, the BLHeli_32 was designed to utilise the power in 32-bit processors (Liang, 2020a).
For most people the default settings in the ESC firmware is satisfactory, with no need to make any changes.

4.3.5 ESC Protocol

ESC protocol is the means of communication between the ESC and the motors or flight controller. The practical difference between protocols is the time used to send data, or *signal width*. Below is a list of some common (and less common with time) protocols and their respective signal width (Liang, 2017b).

- **PWM**: 1000-2000 μs
- **Oneshot 125**: 125-250 μs
- **Oneshot 42**: 42-84 μs
- **Multishot**: 5-25 μs
- **Dshot150**: 106.8 μs
- **Dshot600**: 26.7 μs
- **Dshot1200**: 13.4 μs

PWM (pulse width modulation) was quite common earlier, but has been phased out by faster protocols, much thanks to improved hardware. The Multishot protocol can, in theory, be incredibly fast. However, signal width increases with throttle speed, up to 25 μs at 100% throttle, meaning that in most practical cases its signal width is higher than just 5 μs. That leaves, in many cases, Dshot1200 as the fastest protocol, with a stable signal width of 13.4 μs. This protocol can be found in some 32-bit processor ESCs.

4.3.6 Processor

As seen earlier the processor of the ESC is a central part in the development of better firmware and communication protocols. The most important thing to note in an ESC processor is whether it is 8-bit or 32-bit. As mentioned above, 32-bit processors allow for the use of BLHeli_32 in addition to enjoying the faster Dshot1200 protocol. Higher capacity 32-bit processors also open up for some additional features, described in the next section.

4.3.7 Additional features

With better processors come the option to assign additional tasks to the ESC. Below are a list of some additional features one may find in an ESC (not all require a 32-bit processor).

- **BEC (battery elimination circuit)**: Equips the ESC with a 5V output that can be used to power other components.
- **ESC Telemetry**: ESC telemetry will allow the pilot to monitor ESC data live, such as motor speed and ESC temperature.
- **Current sensor**: With a current sensor in the ESC one can monitor the full current consumption in the drone, since the ESC is directly linked to the battery. This feature goes under the ESC telemetry category.
- **Voltage sensor**: Just like with the current sensor, an ESC with voltage sensor can be used to monitor battery voltage. This feature also goes under the ESC telemetry category.

4.3.8 Selection of ESC

The ESC in the drone constructed was selected so that it would not limit selection of other components to a great extent, much in terms of current and voltage ratings. Great performance, extra features for performance analysis and weight were also thoroughly considered.

Selected ESC: Aikon AK32PIN 20x20 4-in-1 35A 6S BLHeli32 (GetFPV, a)

This ESC handles continuous current of 35 A, 45 A burst current, and battery voltages ranging from 2S to 6S. This allows for great flexibility in both motors (and propellers) and battery. The 4-in-1 solution gives a lighter compact ESC setup. While most ESCs have mounting holes in a 30.5x30.5 mm configuration, this ESC is so small that a 20x20 mm mounting hole configuration is used. This results in a total weight of 10 g.
On the hardware side it features a 32-bit processor from ARM Cortex (STM32F0 series), allowing it to run BLHeli_32 and the Dshot1200 protocol. Additional protocols supported are other Dshot protcols, Proshot and Oneshot.
For analysis purposes this ESC comes with ESC telemetry and sensors for data on voltage, current and motor RPM.

4.4 Flight Controller

The flight controller (FC) is the brain of the drone, and responsible for matching the pilot commands to the behaviour of the drone. Over time, FCs have grown rich in features, and following are some of the most important.

4.4.1 Voltage rating

Just like the ESC the FC is capable of running at a limited range of voltages. The battery voltage must therefore be within the voltage range rating of the FC (and the ESC).

4.4.2 Firmware

FCs have a few more firmware options than the ESC, where some of the common ones are *Betaflight*, *iNav*, *FlightOne* and *KISS* (Liang, 2020b). Going into how each one differ from the other is a difficult task, but the common starting point for getting familiar with flight controller firmware and finding out what you want is Betaflight. It is open-source, available for a number of flight controllers and has a large user base for support.
With the firmware, using a configurator on a computer, one can tune the drone, set up and test communication and much more.

4.4.3 Processor

The processor is what translates pilot commands to motor control, as well as handling any additional tasks. Just like with the ESC a better processor will open up for better flight performance and additional features. The common types of processors found in flight controllers, with the main differences being computational speed and memory, are seen in table 4.2 below (Liang, 2020b).

Name	Speed	Memory
F1	72 MHz	128 KB
F3	72 MHz	256 KB
F4	168 MHz	1 MB
F7	216 MHz	1 MB
H7	480 MHz	128 KB

Table 4.2: Flight controller processors (Liang, 2020b)

F1 and F3, with their slow computational speed and limited memory, are no longer supported in Betaflight, and so most go with F4 or F7. Which one to go with of the two is basically a trade off between cost and power.

4.4.4 UART

Universal Asynchronous Receiver/Transmitter, or UART for short, are ports on the FC that open up for connecting additional equipment, such as radio communication or video, to

the FC. The UARTs come in pairs of receivers and transmitters, so that data can be both sent and received by the FC.
The number of UARTs, and, thus, the amount of additional equipment that can be attached, will depend on the processor (and the design of the FC). For example, the F7 processor will have the potential to handle more in/out data than that of the F4.
A small, but essential, detail in UART ports is how some handle inverted signals, whereas other do not. Some radio receiver signals (more on that later) are inverted and will either need a FC that can handle inverted signals, or an additional module for converting them to readable signals for the UART. F3 and F7 processors can handle the inverted signals, while F1 and F4 are unable to do that and therefore require external inversion.

4.4.5 Flight essential sensors

For stable and reliable flight drones make use of *gyroscopes* and *accelerometers*, depending on the flight mode. These two sensors are combined in a single unit called *IMU*, or *inertial measurement unit*, to provide data on angular velocity and acceleration (or, more correct, force) on three axes.
To avoid having to buy and integrate the IMU as a separate component many FCs come with one already in place, in the shape of an MPU (*Motion Processing Unit*). An example of a commonly used MPU in drones is the MPU6050.
Other sensors that may be included are barometers and magnetometers. An example is the MPU9150, which houses a gyroscope, accelerometer and magnetometer.
All MPUs have a sampling rate, i.e. a rate at which they read and update values. One might think that an MPU holding more sensors sampling at a higher rate than some other MPU is the better choice, but that is not the case. The truth is that some MPUs are adversely affected by the hidden factor of noise. For example, the MPU6000 (sampling rate 8 kHz) is considered a better pick than the MPU6500 (sampling rate 32 kHz), simply due to excessive noise in the MPU6500 (Liang, 2020b).

4.4.6 Additional features

Like with the ESC FCs hold some features that are not necessary for flight, but may come in very handy in its application. A selected very few are listed below.

- **BEC**: The FC may provide a voltage output of typically 5 V to power other components.
- **Current and voltage sensor**: Similar to the ESC.
- **Blackbox**: Lets the drone store flight data on a MircoSD card in the FC.

4.4.7 Selection of FC

The FC was, like the ESC, chosen so that it would not limit further development or experimentation with other hardware combinations. In addition, it was essential to be able to extract flight data from the FC in order to analyze flight performance.

Selected FC: Lumenier LUX F7 Ultimate Flight Controller (Dual Gyros) (GetFPV, c)

The Lumenier LUX F7 comes, as its name indicates, with a top of the line 216 MHz F7 processor (STM32F722RET6), enabling it to handle heavier calculations at greater frequencies. It also supports Betaflight (and iNav) software, making the setup and tuning process fairly user friendly, as well as 2-8S battery compatibility.
In terms of sensors it houses a barometer (BMP280) and *two* IMUs. The first IMU is the well known MPU6000, sampling gyro data at 8 kHz and less prone to noise compared to, for example, the MPU6500. The second IMU, ICM20602, samples gyro data at 32 kHz, four times the rate of the MPU6000. It is newer than the MPU6000 and, therefore less common to find in drones. The high sampling frequency also means that not all processors can handle this IMU. Note that both can not be used simultaneously, but having two options give great possibilities for experimenting.
Additional features in the LUX F7 are a MicroSD-card slot for blackbox logging, 5 V and 3.3 V BEC, battery voltage sensor, 5 UARTs with built-in inversion, Dshot support and support for both PPM and Serial RX (see next section for further explanation). At only 6 g it fits nicely in a lightweight drone.

4.5 Communication

Communication with the drone relies on a transmitter (TX) and receiver (RX), and so following are important considerations on selection of these two.

4.5.1 Frequency

Options for frequency is limited, and in most cases 2.4 GHz is used. Some may use 900 MHz, but in many countries this is illegal as the frequency is reserved for public communication.
In basic terms, higher frequency give more robust communication, while lower frequencies provide better range.

4.5.2 Number of channels

In order to control a drone four channels are required for pitch, roll, yaw and throttle. Additional channels can be used to switch on/off additional features or similar. Common number of channels are four, six, eight and 16.

4.5.3 TX protocol

TX protocol is referred to as the means of communication between the transmitter and the receiver. Deciding on a transmitter will limit the options for a receiver, and vice versa, as they require a matching communication protocol. On the hobby market a transmitter from one brand, such as *FrSky*, will not be able to communicate with a receiver from a different brand, like *Flysky*. Either way, both of these popular brands taken as an example

provide well developed TX protocols. Examples of FrSky TX protocols are D8 and D16, and Flysky TX protocol examples are AFHDS and AFHDS 2A (Liang, 2017b).

4.5.4 RX protocol

RX protocols are the means of communication between receiver and flight controller, and often require more consideration than TX protocols. Not all FCs can directly handle all types of RX protocols (as mentioned earlier, F4 processor FCs are unable to take inverted signals), and some protocols are faster than others. Similarly to TX protocols *some* RX protocols are brand exclusive, while others are universal. Below is a list of some RX protocols (Liang, 2017b).

- PWM (universal)
- PPM (universal)
- SBUS (Futaba, FrSky)
- IBUS (Flysky)

PWM (pulse width modulation) is probably the simplest in terms of working principle. Without going into too much detail, a major drawback of PWM is that each channel require its own wire, in addition to high latency.
PPM (pulse position modulation) is superior to PWM in the sense that it requires only one signal cable for all channels (though the number of possible channels is limited).
Both **SBUS** and **IBUS** are digital serial protocols, as opposed to the analogue PWM and PPM. With these come reduced latency, the option for even more channels and loss-less communication (Liang, 2017b). The drawback of SBUS is the inverted signal which will not work with all flight controllers unless an external inverter is used.

4.5.5 Selection of communication hardware

Communication hardware was selected mostly based on the receiver as this is likely to be what affects drone performance the most. Weight, number of channels, compatibility with the selected FC and communication protocol were important factors.

Selected receiver: FrSky R-XSR (Elefun, a)

The FrSky R-XSR, weighing in at $\sim$1.5 g, adds very little weight to the drone. It supports both SBUS (16 channels) and PPM (8 channels), both of which are supported by the selected FC, but is limited to X-series FrSky transmitters with its FrSky D16 TX protocol. The receiver also supports *telemetry*, i.e. the possibility to transmit live data from the drone to the controller.
Based on the selection of receiver, transmitter selection was limited to a compatible FrSky controllers. This was not seen as a critical, and a Taranis X9D Plus was borrowed for the duration of the project.

4.6 Battery

The battery in a drone has some basic features that may drastically impact the drone performance. These features are explained further on, assuming that an energy dense LiPo-battery is used.

4.6.1 Voltage rating

LiPo-batteries are built up by 3.7 nominal voltage cells (4.2 V fully charged) in series. The number of cells in a battery is denoted with an *S*, such as 2S or 3S for two and three cells, respectively. More cells give more power, but also increases the weight. It is important that the rest of the hardware can handle the battery voltage.
In small-medium drones 3S and 4S batteries are commonly used.

4.6.2 Capacity

Drone LiPo-batteries generally range from the low hundreds of mAh in a light weight drone to several thousand in larger drones. An increase in capacity means an increase in weight, and is therefore not proportional to increased flight time.

4.6.3 Discharge rate

Discharge rate, denoted *C*, is a measure of how much current the battery can provide without taking damage. Discharge rate is given as both continuous and burst, where burst is the amount of current it can supply for a limited time (seconds). How much current the battery can supply is calculated using equation (4.1) below.

$$Current(A) = Capacity(Ah) * C \tag{4.1}$$

As an example, a 500 mAh 75 C continuous current, 100 C burst, battery can provide $0.5A * 75 = 37.5A$ continuously and 50 A for a limited time. In this case, one could therefore not have the motors pulling more than 37.5 A continuously, as this would damage the battery.

4.6.4 Weight

As one might expect, heavier batteries will reduce flight time unless capacity is heavily increased. Considering a capacity-to-weight ratio may therefore be helpful. The relationship is, as mentioned, not linear, and so this would be somewhat helpful only up to the point where weight reduces overall efficiency or exceeds motor thrust capabilities.

4.6.5 Selection of battery

The battery was selected with weight heavily in mind, as batteries tend to largely contribute to the total weight of the drone.

Selected battery: BetaFPV 3S 300 mAh 45/75C (BetaFPV)

The battery selected was already purchased and available prior to this project. It is very light-weight, only 26 g, with a capacity-to-weight ratio of ∼11.5 mAh/g. The 3S voltage is also supported by a broad range of other components, and offers a neat compromise between power and weight. Discharge rates of 45/75 C allow the battery to supply 13.5 and 22.5 A of continuous and burst current, respectively.
It must be mentioned that the selected battery has its limitations. 300 mAh is on the lower end of the market available capacity range, and the maximum 13.5 A continuous current is very likely to limit the motors from operating at its full range. A better option would probably be the Gens Ace Tattu R-line 3S 550 mAh 95C (Elefun, a), with capacity-to-weight ratio 12.8 mAh/g and a continuous current limit of 52.25 A. This was, unfortunately, not easily available at the point of testing the drone.

4.7 Hardware summary

Hardware	Type	Weight (g)	% of total weight
Motors	EMAX RS1106II 4500kV	4 x 7	39.2 %
ESC	Aikon AK32PIN 20x20 4-in-1 35A 6S	10	14.0 %
FC	Lumenier LUX F7 Ultimate FC	6	8.4 %
Receiver	FrSky R-XSR	1.5	2.0 %
Battery	BetaFPV 3S 300 mAh 45/75 C	26	36.4 %
SUM:		71.5	100 %

Table 4.3: Hardware summary

Table 4.3 sums up the hardware to be used in the project, with motors and the battery being the largest contributors to the total weight.
The setup is limited in maximum voltage firstly in the motors (4S), and secondly in the ESC (6S), while minimum input voltage is limited by both ESC and FC at 2S. As for current the battery (13.5 A continuous current) puts some clear low-end current restrictions to the setup. The next limitation is found in the ESC (35 A), though this is far higher than the limit set by the battery.

Chapter 5

Frame Design and Simulation

For frame design Autodesk's Fusion 360 was used. Room for the charging solution was not included, as this was considered a separate component of research, likely immature for implementation on the drone at the end of this thesis.
Fusion 360 is a 3D-modelling software by Autodesk, available for free on a student license. In addition to modelling it features other tools, such as rendering and some basic types of simulations. Simulations can be done using Autodesk's cloud, but in exchange for so-called *cloud credits* that can be purchased. In this case, no cloud credits were available, and so all simulations were run locally. A less ideal personal computer was used for both design and simulations, as the university computers were unavailable due to the Covid-19-virus.
The computer has the following basic specifications:

MacBook Pro 13" (early 2015)

- Processor: Dual-Core Intel Core i5 2.7 GHz
- RAM: 8 GB
- Storage: 256 GB, close to full

3D-modelling was manageable using this computer, but lagging at times. Simulation times were acceptable when keeping meshing basic, at the cost of less accurate results. The simulation results were therefore used merely as a tool for spotting weak links in the design, and to verify that the overall design in general was well within the physical limitations of the material used.

Two designs were modelled, each with their qualities and limitations. Further on are some features of interest when designing the frames, followed by the two designs.

5.0.1 Desirable frame features

In order to suit the application of the drone, as well as further modification and experimentation with the drone, the features listed below have been considered desirable. Note that there are trade-offs to consider when choosing between features.

- **Light weight**
  A light weight drone has numerous advantages in an indoor environment. Power consumption is reduced, resulting in greater flight times and possibly less noise. The impact of a potential crash is also reduced, compared to that of a heavier drone.
- **Strength**
  A minimum requirement is that the drone can carry its load while moving around with some acceleration. A bonus is if the frame can withstand an unfortunate crash without taking damage, while protecting its components. This feature competes with the desire for a light weight frame as greater strength and component protection often require more material.
- **Flexibility**
  As a concept drone flexibility comes in handy with the quality of easy modification for testing of new hardware. This feature does, however, potentially require a more complicated design and extra weight.
- **Shrouds**
  Shrouds is a lot of what this drone is about, as it is used for both noise reduction and damage reduction in case of a crash. The obvious drawback of this feature is the fairly large amounts of weight it adds to the frame.
- **Air duct for sensor chamber**
  Similarly to shrouds, the air duct, or air intake, for the sensor chamber is a central part of this concept. They also both share the drawback of increased weight.
- **Prepare for autonomy**
  As the finished product aims for full autonomy it is beneficial if the first working prototype can carry the necessary hardware in an autonomous drone. This may involve room for a different flight controller or mounting possibilities for LiDAR's. Preparing the drone for autonomy somewhat overlaps with the desire of a flexible design solution.

5.0.2 Design 1 - Modular construction

The first design took a direction towards functionality, much in terms of flexibility. A spacious main frame was designed, notably larger than required with the current hardware, in order to be able to fit a larger flight controller, a small computer or other hardware in a future setup. Wall thicknesses were also deliberately over-engineered in order to have a safe drone, strength wise, as the first flying prototype.
Shrouds and air ducts for the sensor chamber were also included in the design.

The concept

To provide a flexible design the first concept was based on a drone built up by modules, with ”endless” possibilities for easy expansion. The ”heart module” of the drone consists of the motor slots with shrouds, as well as the sensor chamber and its accompanying air ducts. Additional modules were then designed for carrying necessary hardware, such as the ESC and the FC, and added to the heart module.
Two types of additional modules were used in this design; platform modules and frame modules.
The platform modules were designed specifically to carry hardware, while frame modules were designed to enclose the platforms and bind them with the other modules. Below is figure 5.1 showing the templates for the platform and frame modules. The frame modules are 100x80 mm in width and depth, whereas height is adjusted according to the hardware it encloses.

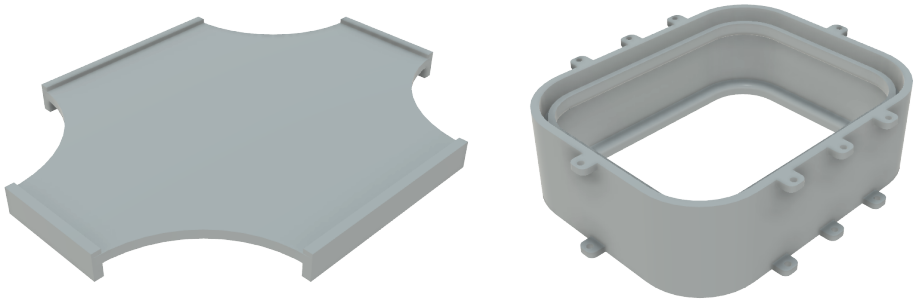

Figure 5.1: Templates of the platform module (left) and frame module (right)

Platform modules are locked by placing them between two frame modules, and then the two frame modules are locked together with nuts and bolts on the outside for easy access to modification. This way, platform modules carrying each their type of hardware can be moved up or down in the arrangement to, for example, experiment with moving the centre of gravity around. Figure 5.2 shows a cross-section of how a platform and two frames are locked together in an assembly.

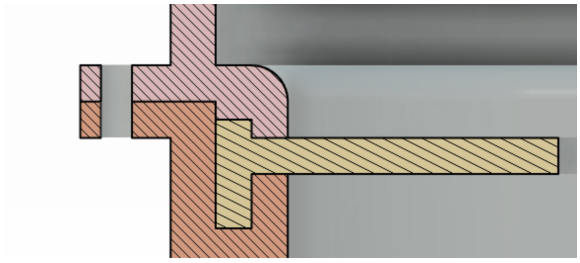

Figure 5.2: Assembly of platform (yellow, middle) and frame modules (pink and orange, top and bottom, respectively).

On the left hand side of figure 5.2 the bolting holes can be seen. It is unlikely that all bolting holes seen in figure 5.1 are necessary, but these were designed as part of the over-engineering approach.

Following are the modules constituting a complete assembly.

The Heart module

Figure 5.3: The heart module carrying the motors, sensor chamber and air ducts

The heart module carries, as seen in figure 5.3, the motors, including shrouds, air ducts and a sensor chamber (68.7 x 48.7 x 18.5mm) measuring 48,396 mm^3. No lid was designed for the chamber. A cross-section showing the connection between motors, ducts and sensor chamber is shown at the top of figure 5.4. The bottom of the figure shows a mounting slot for the Benewake TFmini LiDAR (Benewake), as part of the ”prepare for autonomy” desire. LiDAR mounting slots are found on both short sides of the frame.

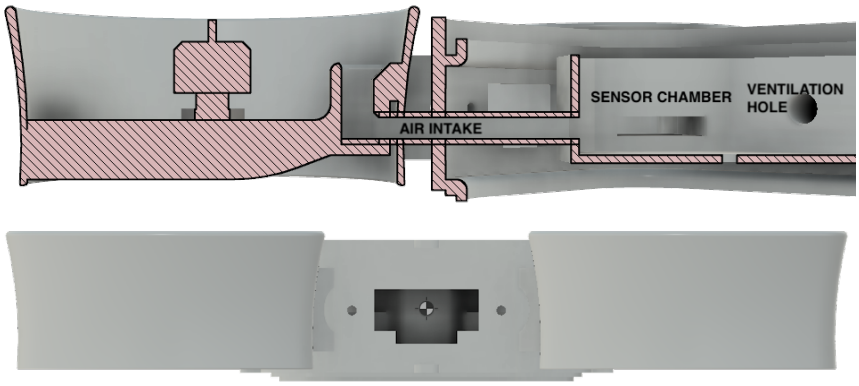

Figure 5.4: Top: Connection between motors, ducts and sensor chamber. Bottom: LiDAR mount on the shorter side of the frame

From figure 5.4 one can also see how the shrouds have been shaped. They are designed to open up at the top to direct noise upwards, but narrow in at the bottom to increase thrust generated from the motors and propellers.
The figure also shows the air duct inlet attached on the side of the shrouds. Ideally, these would interfere as little as possible with the air flow from the propellers, as this reduces efficiency. At the same time, some amount of flow rate is desired in the sensor chamber in order to achieve sufficient circulation of air.
An estimate of air flow rate and air velocity is calculated using the previously established equation (2.17) with the following parameters and assumptions:

- A_1 = 0.197 m^2
- A_2 = 0.095 m^2
- DF = 0.7
- TWR = 1
- W_d = 2.55 N (estimated weight of frame assembly, including hardware)
- D = 0.0635 m
- ρ = 1.225 kg/mm^3
- Assumption 1: Drone is hovering (TWR = 1) or flying at low speed (TWR $\approx$ 1)
- Assumption 2: Losses in the ducts are neglected

$$v_2 = \frac{0.197m}{0.095m} * 0.7\sqrt{\frac{8 * 1 * 2.55N/4}{\pi * (0.0635m)^2 * 1.225kg/m^3}} = 26.3m/s$$
$$Q = 0.095m^2 * 26.3m/s = 2.499m^3/s$$

Since all four motors are linked to the sensor chamber the full air flow rate coming in is 9.994 m^3/s. That is an extremely large flow rate considering the relatively low sensor chamber volume. Assumptions aside, the actual flow rate is likely to be far less. The above calculations do still indicate efficient circulation of air in the chamber.

In table 5.1 all components constituting the ”heart module” are shown with their respective weight, assuming a plastic material of density 0.001 g/mm^3.

Figure	Name	Qty.	Weight (g)	% of total weight
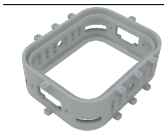	Frame	1	31.4	26.8%
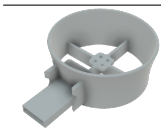	Shroud and duct	4	74.8	63.9%
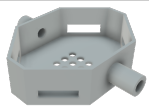	Sensor chamber	1	10.8	9.2%
SUM	Heart Module	6	117.0	100%

Table 5.1: Break-down of heart module

Flight Controller module

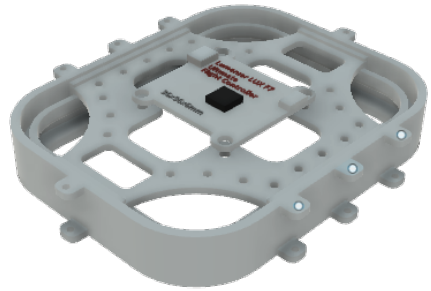

Figure 5.5: The Flight Controller module carrying the FC

The Flight Controller module's, shown in figure 5.5, sole purpose is to mount the flight controller. The FC is mounted on a platform that is locked between the FC module and Heart module. In addition, it features mounting holes and openings to fit the earlier mentioned Benewake LiDAR in a downward facing position.
With only two components, a platform module and a frame module, the construction is fairly simple. Weight distribution on the FC module is shown in table 5.2.

Figure	Name	Qty.	Weight (g)	% of total weight
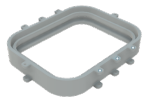	Frame	1	20.9	75.0%
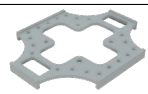	Platform	1	7.0	25.0%
SUM	FC Module	2	27.9	100%

Table 5.2: Break-down of FC module

ESC Module

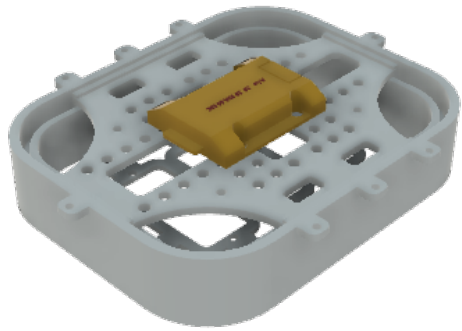

Figure 5.6: The ESC module carrying the ESC

Similar to the FC module, the ESC module, shown in figure 5.6, has a single main purpose, this time to carry the ESC. The platform features a number of mounting holes, whereas the frame itself, which this time is closed at the bottom, has three mounting slots for a downward facing Benewake TFmini LiDAR. Three slots are merely for the purpose of flexibility, and not for mounting three LiDARs facing the same direction, as this is not necessary.
The platform is locked between the ESC module and the above FC module, and the closed bottom of the frame ends the possibility to further addition of modules.
The weight distribution of the ESC module can be seen in table 5.3.

Figure	Name	Qty.	Weight (g)	% of total weight
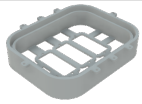	Frame	1	34.9	81.0%
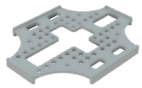	Platform	1	8.2	19.0%
SUM	ESC Module	2	43.1	100%

Table 5.3: Break-down of ESC module

Design 1 Summary

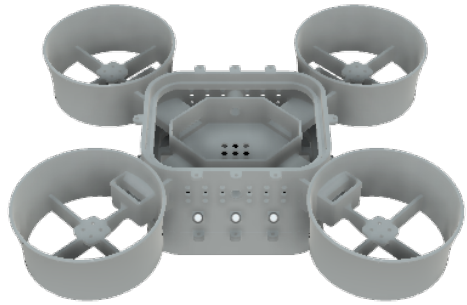

Figure 5.7: The complete assembly of design 1

Feature	Value
Diameter (mm, propeller-propeller diagonal)	193
Height (mm)	67
Weight (g)	188

Table 5.4: Design 1 dimensions and weight

The complete assembly of the first design is shown in figure 5.7, with dimensions and total weight in table 5.4. From the bottom to the top, it is assembled by the ESC module, FC module and Heart module, constituting a total weight of approximately 188 g (hardware excluded). The ESC, FC and Heart modules contribute to 23%, 15% and 62% of the total weight, respectively.
Low quality strength analysis was performed throughout the process, indicating a well over engineered design, as expected. Because of the large weight, making it less suitable for efficient flying, this design was discarded. Any further analysis is therefore not included.

5.0.3 Design 2 - Light and flexible compromise

The second design came as a reaction to the larger and heavier design 1. The first design has a flaw in the sense that the heart module does not carry all necessary hardware in order to fly, and would therefore require additional modules. The ”heart” has therefore been defined as the parts that generate thrust (motors), carries the components required for its purpose (sensor chamber carrying sensors) and shrouds reducing the noise. A better approach to defining a ”heart module” may be to include all components that make a drone fly, and rather have the sensor chamber and air ducts as an auxiliary function.

The concept

In order to reduce weight in the frame design some of the module concept seen in design 1 is left out. The basic idea was to deign a frame printed in one piece, capable of carrying necessary hardware for flying, but not perform any other other specific tasks. In order to maintain some flexibility it can be easily modified to carry more specialised hardware.
Similarly to the previous design there is room to fit larger hardware than what is used in this case. It is also intentionally over-engineered for the sake of a sturdy construction, though not to the same extent as the previous design.
The design is divided in two main parts; main frame and specialised modules, presented next.

Main frame

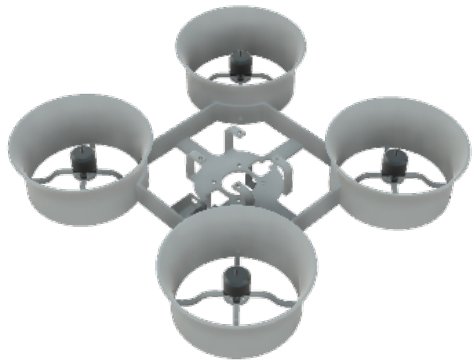

Figure 5.8: Main frame in design 2

The main frame shown in figure 5.8 houses all components necessary for a flying drone; motors, ESC, FC, battery and receiver, but nothing more. Visual comparison to the ’heart module’ in design 1 indicate a much lighter design, while at the same time being richer in features. This visual impression is backed up by the reduced weight, estimated to be 66.5 g (0.001 g/mm^3 plastic).
The inside of the frame itself measures about 97x97 mm, and so there is room for installing larger/more hardware with simple modifications on the inside of the frame.

The shrouds are designed similarly to the ones seen in the previous design; wider at the top, before narrowing in at the bottom.

Figure 5.9 sums up all mounting possibilities in the second design.
On the left hand side of (1) is the receiver box, specifically and tightly designed to house the FrSky R-XSR receiver. It has a hole in the back for the antennas to exit, and another hole in the front for the signal output connector to go. When plugging in the signal cable from the FC the receiver remains locked in place.
Just underneath (2) one can see one out of four poles holding the FC. These are placed so that the mounting holes on top of the poles are in a 30.5x30.5 mm configuration.
Just north-east of (3) is one of four mounting holes for the ESC, centred around a larger hole (for ventilation and weight reduction purposes) in a 20x20 mm configuration.
To the left hand side of (4) one can see parts of one out of two battery holders. These are dimensioned to tightly hold the BetaFPV 3S 300 mAh (from the hardware chapter) in place.

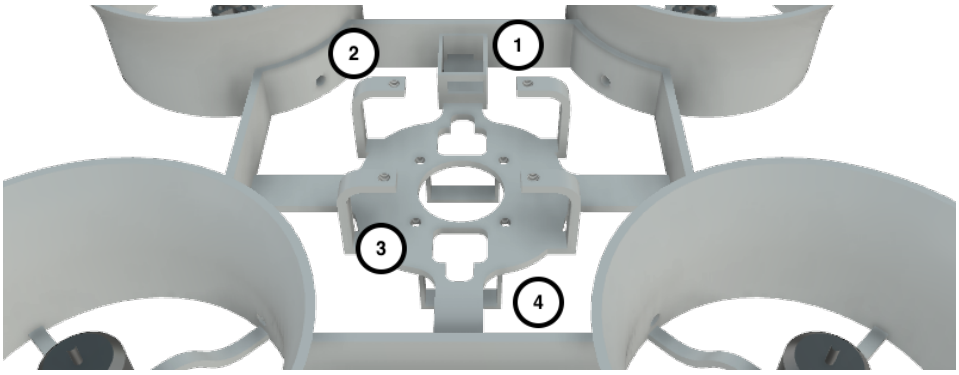

Figure 5.9: Design 2 features: (1): Receiver slot (2): FC mounting poles (3): ESC mounting holes (4): Battery slot

Specialised module: Sensor chamber

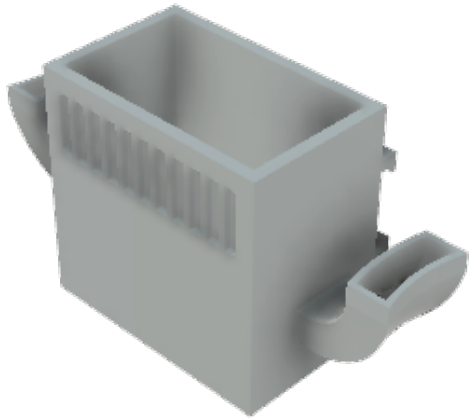

Figure 5.10: Sensor chamber with intakes on the sides

Figure 5.10 shows the sensor chamber to be mounted on the main frame. The current version weighs 12.8 g and measures 36x36.6x21 mm on the inside, with a volume of 27,669 mm^3, $\sim$57% the size of the sensor chamber in design 1. The simple geometry and the fact that it comes as a standalone module, separate from the drone itself, allows for easy customization to fit its content. It features double air intakes that connect to the air flow inside the shrouds (shown in figure 5.11), ventilation grid and an easy clip on solution for mounting to the main frame (shown in figure 5.12).
No lid was designed for the sensor chamber.

Figure 5.11 also shows suggested placement of four sensors (figure 5.12 shows two of them at a different angle). Note that they are tightly placed in order to maintain a design as compact as possible. The following assumptions were therefore made:

- No/little additional components are required inside the chamber for the sensors to work
- Auxiliary electronics are placed outside the chamber
- Wires from the sensors to auxiliary electronics are small in diameter and not dominant
- Mounting of the sensors can be done using glue or any other method requiring little space.

The sensors used are listed in table 5.5. Data is based on a fall 2019 project by Sivert Kittelsen (Kittelsen, 2019).
The following abbreviations are used in the table:

- **VOC** - Volatile Organic Compounds

- **eCO$_2$** - Estimated carbon dioxide

Fig. 5.11 number	Model	Measures	Dimensions (mm)	Weight (g)	Typ. consump. (mA)
1	Si7021	Temperature Humidity	17.8x15.3x3	1	0.15
2	MPL115A2	Pressure	5x3x1.2	0.61	0.05
3	CCS811	VOC, eCO$_2$	21x18x3	2	30
4	T6713	CO$_2$	30x15x8.6	4	20
SUM				7.61	50.2

Table 5.5: Sensor data (Kittelsen, 2019)

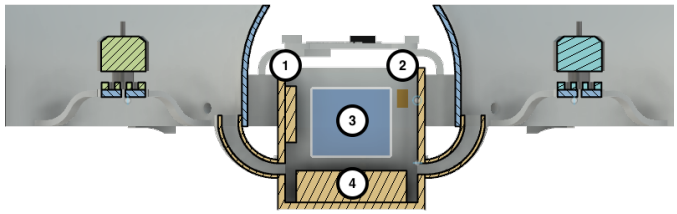

Figure 5.11: Cross section of sensor chamber

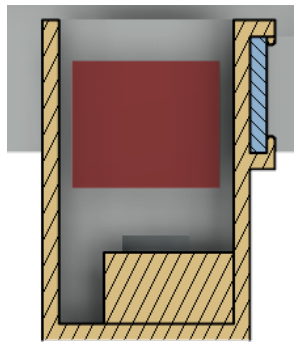

Figure 5.12: Cross section of sensor chamber showing mounting to main frame (right hand side)

Kittelsens paper aimed to find sensors for measuring temperature, humidity, pressure, CO$_2$, dust and TVOC (Total Volatile Organic Compounds). Si7021, MPL115A2 and T6713 were chosen in a final selection of sensors for the former four environmental factors, respectively, whereas sensors for dust and TVOC needed more testing. Nevertheless, room for the TVOC/VOC measuring CCS811 sensor was made in the sensor chamber, in

case a sensor of similar size is found sufficient in the future.
As for a dust measuring sensor no available space was found in the current sensor chamber design. The two dust sensors tested were GP2Y1010 AU0F and SPS30 measuring 46x30x17.6 mm, 16 g, and 41x41x12 mm, 26 g, respectively (Kittelsen, 2019). While the sensor chamber is easily customized to fit desired components it was considered ineffective to include a bulky dust sensor in a small sized drone with limited thrust capabilities.

The estimated air velocity and flow rate entering the sensor chamber can once again be calculated using equation (2.17). The same parameters and assumptions stated in the design 1 calculations are used, with the following exceptions:

- A_1 = 0.063 m^2
- A_2 = 0.024 m^2
- W_d = 1.47 N (estimated weight, including chamber and hardware)

Yielding the following velocity and flow rate:

$$v_2 = \frac{0.063m}{0.024m} * 0.7\sqrt{\frac{8 * 1 * 1.47N/4}{\pi * (0.0635m)^2 * 1.225kg/m^3}} = 25.3m/s$$
$$Q = 0.024m^2 * 25.3m/s = 0.6072m^3/s$$

With double inlets to the chamber the total amount of flow rate is 1.2144 m^3/s. That is $\sim$12 % of the flow rate seen in the previous design, but still very large considering the size of the sensor chamber. Even though decreased flow rate is not proportional to the decreased size of the sensor chamber, the estimated flow rate is more than sufficient as air is still rapidly replaced. As with design 1 it is, however, unlikely to achieve this exact flow rate considering all assumptions made.

Specialised module: LiDAR mounts

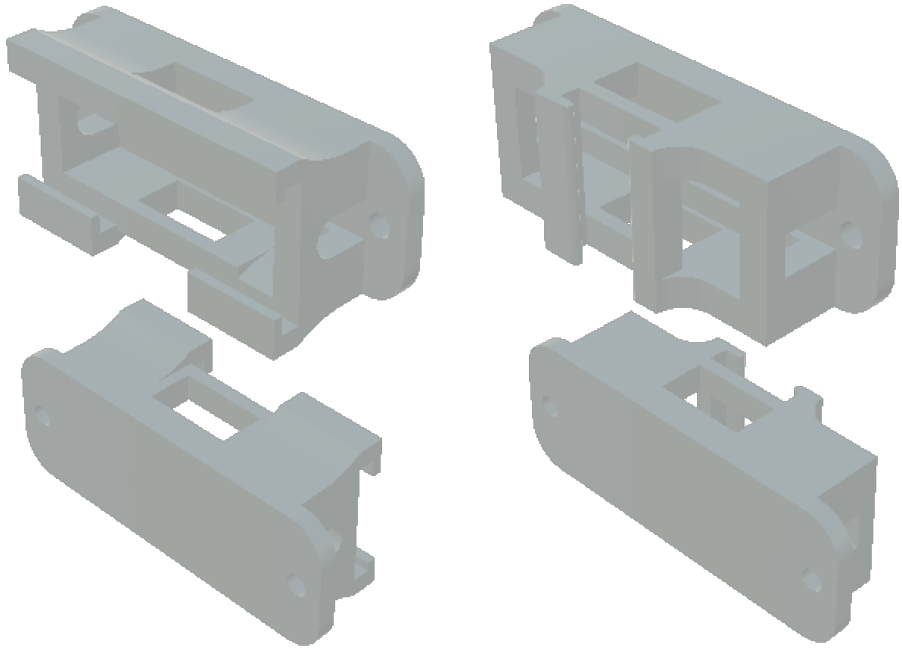

Figure 5.13: Front and rear view of forward/side-way (left) and downward (right) facing LiDAR mounts

Figure 5.13 shows the two LiDAR mounts designed for mounting on the drone, one for LiDARs facing side-ways, forward or backward, the other for a downward facing LiDAR. Mounting holes are, as in design 1, placed to match the lightweight Benewake TFmini LiDAR (Benewake). The working principle of attaching them to the drone is the same as with the sensor chamber, with the only difference being in the downward facing mount, which is narrower in order to fit the flat bars running across inside the frame.
The mounts are hollowed out on the inside for the benefit of reduced weight, but also for cable passage. This allows for placing the mounts over the receiver antenna exit hole.
Estimated weights are 3.47 g for the side/forward facing mount and 3.23 g for the downward facing mount.

Design analysis

As the first design was discarded it was decided to go with the latter one, and in order to ensure a sufficiently rigid structure it was beneficial to perform a strength analysis. As previously mentioned computational power was limited, with only Fusion 360 on a gradually outdated laptop at hand.
Strength analysis was performed using Fusion 360s simulation tool and the static stress

study. This study type requires both a minimum of one constraint and load, in addition to a specified material with set physical properties.
Material of choice was the Fusion 360 built-in alternative ABS (physical properties in table 7.1, chapter 7.0.1), a much used material in 3D-printing with good strength qualities. To represent the pulling force of each motor point loads were applied to each of the motors, with equal magnitude and direction upwards. The constraint is more tricky to translate into physical drone behaviour, as no part of the drone is actually constrained the same way, for example, a bridge is constrained at the ends. Either way, a fixed constraint in the x, y and z axis was applied to the large hole underneath the ESC, as this point is just below the centre of gravity of the drone.
To determine the magnitude of the forces generated by each motor it was decided to work with at TWR of 2 and drone weight of 150 g. Force per motor was then found using equation (2.1):

$$TWR = 2 \rightarrow T_m = \frac{2 * W_d}{4} = \frac{2 * 0.15kg * 9.81m/s^2}{4} \approx 0.74N$$

This was rounded up to 1 N.
Meshing was performed automatically by Fusion 360 with average mesh size set to 5% of model size. Finer mesh is possible, but would, to a greater extent, challenge the computational power available during solving.
The mesh and forces set prior to simulation is shown in figure 5.14.

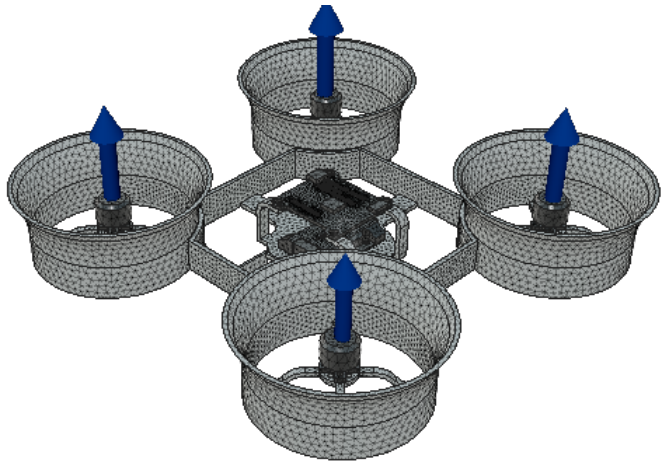

Figure 5.14: Motor forces and meshed model prior to solving

The first test result presented a minimum *safety factor* of 7.23. Safety factor is a way of describing how strong the structure is compared to how strong it needs to be. In other words, the construction is very unlikely to be challenged strength wise.

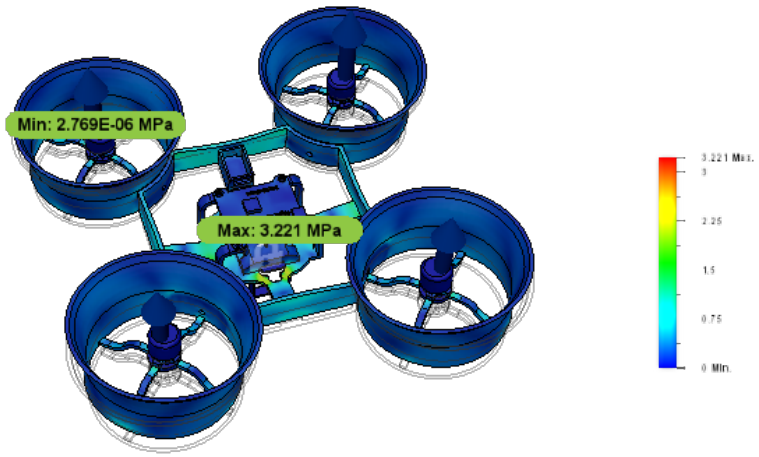

Figure 5.15: Stress distribution (von Mises) in drone frame (maximum 3.221 MPa)

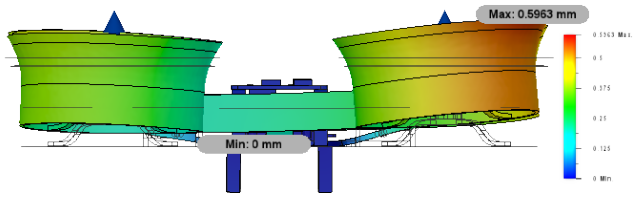

Figure 5.16: Displacement in drone frame (maximum 0.5963 mm)

Figure 5.15 shows stress distributions across the frame, with a maximum of 3.221 MPa near the ESC area at the frame centre. Nearby regions also experience some stress, while the shrouds go more or less unaffected. As the centre of gravity is located in the ESC region, where a fixed constraint was put, the stress distribution across the drone can be considered reasonable. However, since, in reality, no section is constrained, but will actually give in to the motor force and move accordingly, the magnitudes are likely exaggerated.
Figure 5.16 shows scaled up deformation of the drone. The figure is seen from the side, with the receiver box being on the left hand side of the figure (behind the shroud, inside the frame). This provides extra stiffening on this side, hence the lack of symmetry. Either way, the maximum displacement of 0.5963 mm raises no concern.

A full report on the simulation can be seen in chapter 12.1, *Simulation Appendix*.

Estimation of flight time and current consumption was done using the equations from chapter 2.4. Estimated weight, including frame, sensor chamber and LiDAR mounts (table 5.4), hardware (table 4.3) and 10% additional miscelaneous weight sums up to $m_d \approx$ 0.18 kg. Other parameters are:

- Propeller diameter, D = 2.5" (0.0635 m)
- V_{nom} = 11.1 V
- Battery capacity = 0.3 Ah
- ρ = 1.225 kg/m^3
- η_{motor} = 0.5 (50%)
- $\eta_{g/W}$ = 2.75 g/W (fishpepper, 2017)

Method 1 in chapter 2.4 yields the following power consumption and estimated flight time at hover:

$$T_m = \frac{m_d * g}{4} = \frac{0.18kg * 9.81m/s^2}{4} = 0.44N \tag{5.1a}$$

$$\Delta v = \sqrt{\frac{8T_m}{\pi D^2 \rho}} = \sqrt{\frac{8 * 0.44N}{\pi (0.0635m)^2 \rho}} = 15.10m/s \tag{5.1b}$$

$$P_{mech} = T_m \frac{\Delta v}{2} = 0.44N \frac{15.10m/s}{2} = 3.32W \tag{5.1c}$$

$$P_{el} = N_m \frac{P_{mech}}{\eta_{motor}} = 4 \frac{3.32W}{0.5} = 26.56W \tag{5.1d}$$

$$T_{flight} = \frac{0.8 * Ah * V_{nom}}{P_{el}} * 60 = \frac{0.8 * 0.30Ah * 11.10V}{26.56W} * 60 = 6.02min \tag{5.1e}$$

$$I_{in} = \frac{P_{el}}{V_{nom}} = \frac{26.56W}{11.10V} = 2.39A \tag{5.1f}$$

While method 2 suggests the following

$$P_{el} = \frac{m_d}{\eta_{g/W}} = \frac{0.18kg * 1000}{2.75g/W} = 65.46W \tag{5.2a}$$

$$I_{in} = \frac{65.46W}{11.10V} = 5.90A \tag{5.2b}$$

$$T_{flight} = \frac{0.8 * 0.3Ah * 11.10V}{65.46W} * 60 = 2.44min \tag{5.2c}$$

There is a clear disagreement between the two methods, where the latter one is the most pessimistic. While being the simplest method of the two, the second method is, however, likely to be the most accurate in this case. Its 'core data', $\eta_{g/W}$, is retrieved from an actual test of the motors (fishpepper, 2017). Though the tested motors are the predecessors of the ones used here, and efficiency at a given thrust varied depending on propellers, the efficiency used in the above calculations is a good approximation. The propellers used in

the thrust test provided $\eta_{g/W}$, at 45 g thrust (180 g/4 motors), ranging from $\sim$ 2-3.2 g/W. In a quadcopter this is the equivalent of P_{el} and T_{flight} ranging from 90.00 W to 56.35 W and 1.78 min to 2.84 min, respectively.
It therefore seems reasonable to expect a hover flight time of approximately 2-2.5 minutes, pulling $\sim$6 A, though with some uncertainty.

As mentioned in the *Hardware* chapter there was some doubt on the BetaFPV 300 mAh battery, due to its fairly low capacity (albeit accompanied by low weight). A simple theoretical comparison to other batteries is therefore presented in figure 5.17. An efficiency of 2.75 g/W was used for all batteries, though, realistically, there will be some variations due to weight differences. Batteries marked in the plot are:

- BetaFPV 3S 300 mAh 45/75C - 26 g (11.5 mAh/g) (BetaFPV)
- Gens Ace Tattu R-Line 3S 550 mAh 95C - 43 g (12.79 mAh/g) (Elefun, a)
- Gens Ace Tattu R-Line 3S 650 mAh 95C - 60 g (10.8 mAh/g) (Elefun, b)
- Gens Ace Tattu R-Line 3S 850 mAh 95C - 85 g (10.0 mAh/g) (Elefun, c)

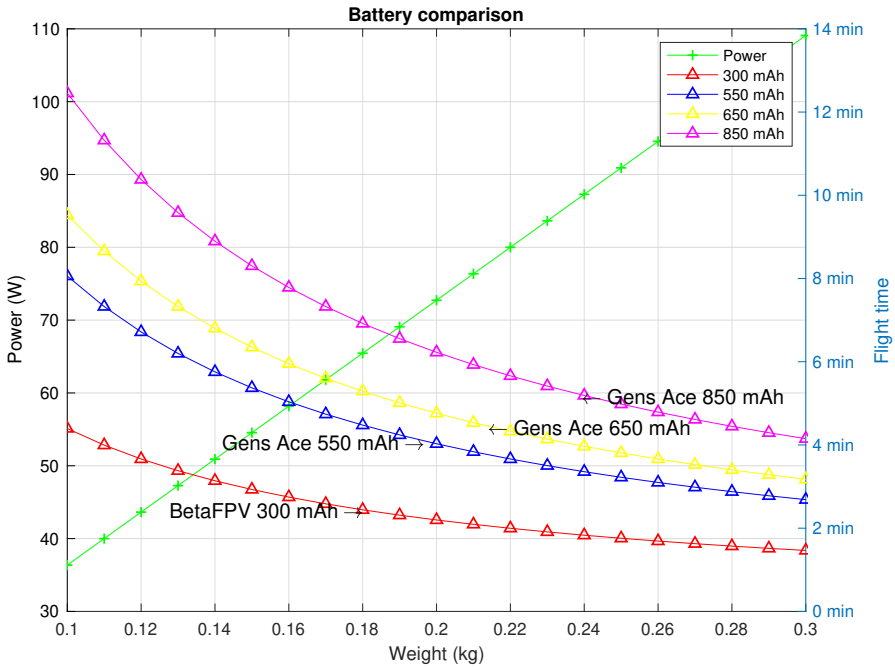

Figure 5.17: Comparison of 300, 550, 650 and 850 mAh batteries

The gap between the current 300 mAh battery and the Gens Ace Tattu 550 mAh is fairly large, almost doubling flight time with only 17 g increased drone weight. The low

change in weight means a drone carrying the 550 mAh battery will likely operate at a similar efficiency to a drone carrying the 300 mAh battery. From 550 mAh to 650 mAh there is little difference in flight time, but it adds another 17 grams. Anything larger than 550 mAh at 43 g, for the current motors, therefore seems unlikely to bring any large improvements to the drone.

Design 2 Summary

Figure 5.18: Design 2 including modules and hardware

Feature	Value
Diameter (mm, propeller-propeller diagonal)	175
Height (mm, sensor chamber and battery holders excluded)	33
Weight (g, frame, 4 x LiDAR mounts and chamber)	93
Flight time (minutes, 300 mAh battery)	$\sim$ 2.5

Table 5.6: Design 2 specifications

Design 2 provides a frame nearly half the weight of the first design, while maintaining all the same functions. Some flexibility has been removed, while still having room for LiDAR and sensor chamber modules. Despite being smaller in terms of both diameter and height there is still room for replacing the current hardware with larger and more powerful hardware.
Strength analysis showed that the construction is more than rigid enough, and that weight can still be reduced by reducing both wall thickness and overall diameter.

Chapter 6

Charging Solution

As part of the autonomous drone a solution for on-board charging, without replacing the battery or any other human interaction, is required. Following an explanation on the concept of charging LiPo batteries are a short description of the concept, as well as the solutions considered and tested for this application. The solutions have been divided in an on-board section (LiPo-charger) and an off-board section (charger power supply).

6.1 The concept of charging LiPo-batteries

LiPo-batteries are high in energy density and need to be treated correctly in order to avoid damage, such as swelling or fire. A clear idea of the concept of charging LiPo-batteries was therefore crucial prior to designing and testing the charging solution.

A LiPo-battery is, as swiftly explained earlier, built up by one or several cells in series producing $S * V_{cell}$ voltage, with *S* being the number of cells in series and V_{cell} the voltage of each cell. The nominal voltage of one cell is 3.7 V, while a fully charged cell measures 4.2 V. Cell voltage above 4.2 V could potentially damage the battery, and even cause a fire. With several cells connected in series each cell should be at the same voltage in order to keep the battery balanced and avoid uncontrolled flow of energy between the cells.

Common LiPo-chargers of today ensure both overcharge protection and cell balance. They also charge the battery according to a *constant current-constant voltage* (CC-CV) algorithm. CC-CV charging starts by applying constant current to the battery, before the current exponentially decreases and a constant 4.2 V (or just below) is maintained. An illustration of how this algorithm works is shown in figure 6.1 (Battery University, 2018). The purpose of CC-CV charging is partly to extend battery life cycle, though some argue CC-CV may actually accelerate battery damage as energy carrying lithium-ions are made defect (Qnovo, 2014). Either way, CC-CV charging is the commonly used and accepted method in today's LiPo-chargers.
Another common feature in LiPo-chargers is allowing to set a charging current. Many

batteries are only safely charged at maximum 1C, and free current flow above this from the energy source could therefore be dangerous.

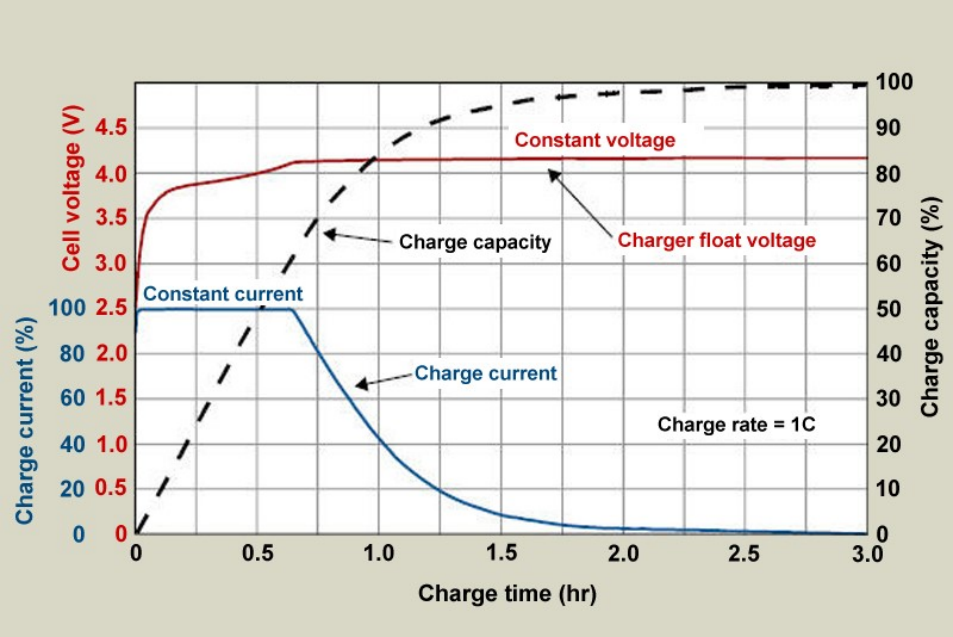

Figure 6.1: CC-CV charging method (Battery University, 2018)

Essential factors in designing the charging circuit therefore include:

- Overcharge protection at 4.2 V (or just below)
- Cell balance
- CC-CV is preferred, but likely not critical from a safety perspective
- Other method of current control if CC-CV is not used

6.2 Charging solution - on-board

A simple way of creating a safe and ”tested” charging solution would be to keep a LiPo-charger on the ground and connect to the battery when the drone lands. However, this was considered too complicated as not only would a perfect V+ and ground connection to the battery be required, but also a perfect connection to the balancing plug.
The alternative was to put a LiPo-charger on the drone, and *somehow* autonomously power it when the drone is docked. There are two challenges with this; LiPo-chargers are often large and heavy, and the battery would need to switch between being connected to the charger and the load (ESC). Alternatives therefore had to be considered.

Initially, two alternatives for an on-board LiPo-charger were considered; the TP4056 module and a *battery management system* (BMS).

6.2.1 TP4056 module

The TP4056 module is a small circuit board that can be powered from a USB and charges with CC-CV. It also features over-discharge and overcharge protection. The module is made for single cell LiPo-batteries, but several modules can be set in a configuration to charge and balance multiple cells (though the complexity increases along with the number of cells). It does, however, not have a solution for switching the battery connection between charging and load. In addition, from personal experience, an employee at NTNU had doubts on the suitability of the module. The TP4056 module was therefore discarded.

6.2.2 Battery Management System (BMS)

The other option, a BMS, come in versions specifically designed for a set number of cells, and DIY configurations are therefore not necessary. The battery also connects to the load via the BMS, and so no method for switching between charging and load is required. Similarly to the TP4056 module it also features over-discharge/charge protection and cell balancing, though no CC-CV algorithm or any other form of current control. Current control would therefore have to come as an external solution.

Test of the BMS module

Most BMS' considered for this application are sold on websites such as Amazon, Ebay and Banggood. The BMS' found on these pages generally had no datasheet and limited technical data available. For that reason, in addition to investigating its suitability for on-board drone charging, a set of BMS' were ordered for testing. The BMS ordered, weighing 9.8 g, were listed with some specifications, and a selected few are seen in table 6.1 (Banggood).

Parameter	Min.	Typ.	Max.
Current consumption (μA)	12	18	24
Overcharge protection voltage (V)	4.2	4.25	4.3
Balanced starting voltage (V)	4.17	4.2	4.23

Table 6.1: BMS basic specifications (Banggood)

In basic terms very little current should be consumed by the BMS, but the overcharge protection voltage is a little high. It should, however, manage to balance the cells at about 4.2 V.

A test of the BMS was conducted, aiming to verify and determine the following:

- Current consumed by the BMS

- Limits to input voltage
- Cell voltage at which the BMS stops charging
- Its ability to balance the cells

At first, a power supply was used to power the BMS at 15 V and 0.6 A, no battery connected. It was observed that it was able to handle the 15 V, and the limited resolution power supply did not report on any current being drawn. It was therefore decided that the current consumed by the BMS could be neglected.

Next, a 3S 300 mAh battery was connected to the BMS, wired as specified by the Banggood seller. The power supply automatically reduced current down to about 0.3 A. During charging it was observed that two cells were quite similar in voltage, while the third cell voltage was $\sim$0.1 V greater.
The higher voltage cell did not stop at 4.2 V, but kept on charging. When the cell in question reached 4.28 V, 0.03 V above listed typical overcharge protection voltage, the charging was finally cut. The two other cells then both measured a balanced and acceptable 4.19 V.
Based on poor overcharge protection and cell balance the BMS was discarded from the charging solution.

6.2.3 Selected on-board charging solution

With the BMS deemed unsuitable another option was discovered in the continuing search for a proper on-board charging solution. Turnigy 12 V 2-3S Basic Balance Charger, a dedicated low-end LiPo-charger, has all the features earlier requested (Hobbyking). In addition, it can be powered by any 11-14 V DC source. The battery is also charged through the balancing plug only, and so the V+/GND plug can always remain connected to the ESC. Larger capacity batteries may, however, take some time to charge as maximum current output is limited to 800 mA.
While LiPo-chargers on the market were never really considered due to large weight and volume, the Turnigy charger is listed with a weight of only 46 g, with dimensions 74x50x25 mm. That is plastic casing included, and stripped of most excessive material weight and dimensions end up at 18 g and 72x40x23 mm, respectively. Weight can be further reduced by a few grams by removing the DC power connector and the 2S battery balance plug. The height can also be reduced to about 16 mm by lowering two elevated LEDs.
The Turnigy charger was tested on the same battery as the BMS, and the results were exactly what the charger promised. That leaves a method of powering the charger the only problem.

6.3 Charger power supply - off-board

Two methods of supplying 11-14 V to the on-board charger were considered, and are presented separately further on.

6.3.1 Conductive power supply

The first, and most basic, option is a physical connection between the on-board charger and the power supply. Both poles on the input of the charger are wired to a part of the drone that touches the landing pad when docked. The charger is then powered by applying voltage to the parts of the landing pad that connects with the input of the charger. To avoid the necessity of high accuracy landing larger areas of the pad can be made conductive. A smart landing pad that detects plus and minus poles on the charger input contact points, and provides supply voltage and ground accordingly, can be used to even further reduce the need for accuracy. Examples of such solutions already exist, for example Skysense's Indoor Drone Charging Pad (Skysense).

Advantages with the conductive solution are, in addition to the low landing accuracy required, little weight added to the drone, simple setup and troubleshooting and high charging efficiency ($\sim$85% with wired charging (Hill, 2019)). On the negative side, contact points are exposed to open air. One might also argue that the technology is ageing, as more and more devices are charged wirelessly rather than through contact points.

6.3.2 Inductive power supply

Inductive, or wireless, charging is the other method of transferring power to the drone. The concept is the same as seen in other wirelessly charged devices, such as some mobile phones. A stationary transmitter coil induces power in a receiver coil in the drone, which then powers the on-board battery charger.
Inductive charging pad is also a product already available on the market. WiBotic, for example, is a company offering solutions to be integrated in 'any' drone (WiBotic). Their lightest solution charges at up to 90 W/5 A, with a receiver weight of 46 g (74 g including enclosure), while the largest solution, at 220 g (413 g incl. enclosure), charges at 300 W/30 A.

Inductive charging has the advantage of being more of a topical subject, compared to conductive charging, with more and more devices moving over to wireless power transfer. In addition, the method allows for a fully enclosed drone. The negatives of this method is generally lower efficiency ($\sim$75% with the common Qi-standard (Hill, 2019)) and it likely being a heavier and more complex solution compared to the conductive method. There is also a requirement for high landing precision as transmitter and receiver coils need to be more or less perfectly aligned in order for there to be any power transmission. Some deviation in alignment is possible, but that often results in reduced efficiency.

6.3.3 Selected off-board power supply

It was decided to move on with the inductive method for power supply. Trends suggest this to be the future dominating method of power supply in certain groups of consumer electronics, and it is likely to see further improvements in this field. One might also see this as a small step towards in-flight charging, a technology already partly developed, which could make a huge difference to the efficiency of drones (Global Energy Transmission).

Most easily available inductive chargers can only supply up to 5 V at 5 W with the Qi-standard. As 5 V is too low for the on-board charger requiring 11-14 V, Semtech's TSDMTX-19V2-EVM transmitter (Semtech, b), powered from a wall socket, in combination with the TSDMRX-19V/20W-EVM receiver (Semtech, a), are more suitable. The receiver can output 19 V at up to 20 W, with charging efficiency up to 85%, eliminating the high efficiency advantage conductive charging had over inductive charging. The low weight of approximately 5 g (receiver coil plus PCB) also means there is not much of a weight difference between the conductive and inductive charging options. Current control comes through smart communication between receiver and transmitter, where the receiver "tells" the transmitter how much current (or, rather, power) is required.
However, with the receiver output of 19 V being too high for the Turnigy charger this needs to be stepped down. This can be achieved using the L7812 voltage regulator, which reduces the 19 V to an output of 12 V (STMicroelectr., 1998). Maximum output current from the L7812 is 1.5 A, and so, in terms of charging rate, the Turnigy charger is still the bottleneck of the system.

6.4 Test of charging solution

Components used in the test of the charging solution are listed in table 6.2, while the complete charging setup is illustrated in figure 6.2. Estimated on-board weight is $\sim$25 g (battery excluded).

Figure 6.4 reference	**Component**	**Reference**	$V_{in}/$ V_{out}
1	Ansmann DC Power Supply	(RS Components)	230 V AC/ 19 V DC
2	TSDMTX-19V2-EVM	(Semtech, b)	19 V DC/ -
3	TSDMRX-19V/20W-EVM	(Semtech, a)	- 19 V DC
4	L7812	(STMicroelectr., 1998)	19 V DC/ 12 V DC
5	Turnigy LiPo-charger	(Hobbyking)	12 V DC/ $<$12.6 V DC
6	BetaFPV 3S 300 mAh LiPo-battery	(BetaFPV)	$<$12.6 V DC/ $<$12.6 V DC

Table 6.2: Components used in test of charging solution

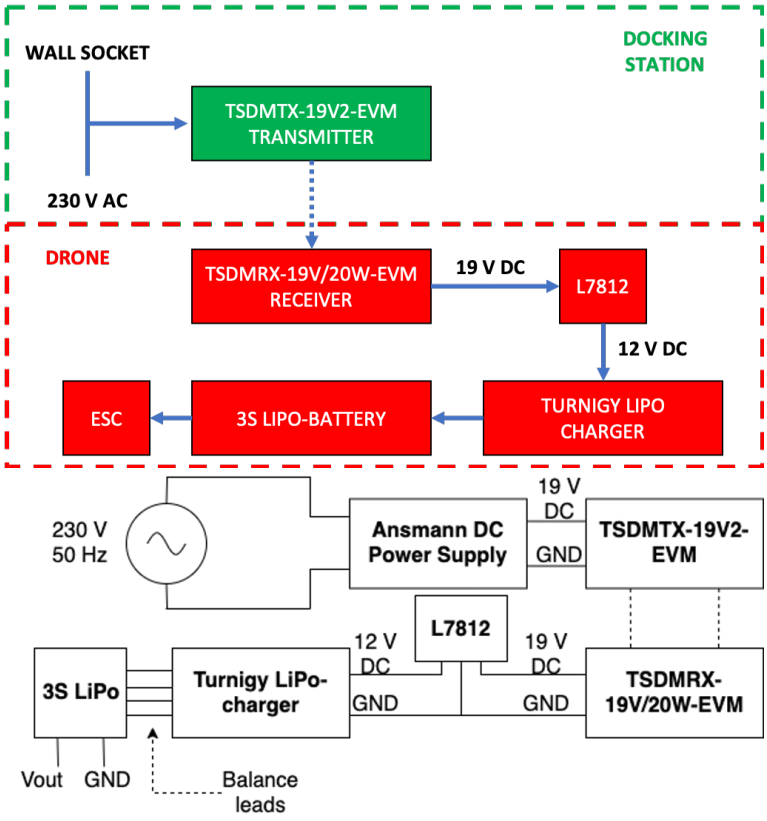

Figure 6.2: Overview of the charging setup

The Ansmann DC power supply was acquired separately of the transmitter due to the manufacturer/seller failing to include a power supply. This introduced the question of correct polarity of the DC power connector. Searching through the transmitter datasheet (figure 6.3) revealed a positive tip/ground sleeve polarity, equivalent to the commonly used symbol for positive polarity:

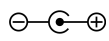

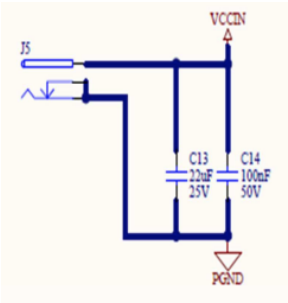

Figure 6.3: Transmitter datasheet revealing DC power connector polarity

Connecting the power supply to the transmitter lit up a green LED, indicating correct polarity and a (so far) working transmitter.

By placing the receiver directly above the transmitter coil, no load connected, LEDs on transmitter and receiver confirmed power transmission. Spacing between transmitter and receiver was ensured through the protective plastic casings the products were delivered in, an equivalent of approximately 7 mm. The manufacturer recommends a minimum and maximum spacing of 6 and 10 mm, respectively (Semtech, 2016).

At no load and perfectly aligned, receiver voltage output was measured to about 19.45 V DC. To verify the manufacturers guidelines on vertical transmitter/receiver spacing, an additional $\sim$2.3 mm of spacing (total of $\sim$9.3 mm) was used. This gave no change in voltage output, while connection was lost at an another $\sim$2.3 mm of spacing (total of $\sim$11.6 mm). Further tests revealed acceptable horizontal receiver displacement of approximately 10 mm before LEDs confirming connection shut off. Receiver voltage output did, however, remain constant at 19.45 V prior to disconnection.

Further on, a test circuit using the L7812 buck converter was set up in order to step down the receiver's 19 V to a 12 V LiPo-charger input. The voltage regulator output was measured to 12.17 V DC, within the acceptable input range of the charger. Though the voltage appeared stable, it may, in the future, be beneficial to add smoothing capacitors to the L7812 input and output to ensure stability. This is also suggested in the L78XX datasheet (STMicroelectr., 1998).

With a verified 11-14 V DC output the Turnigy LiPo-charger was added to the circuit. A red LED swiftly lit up, confirming acceptable power input with no load on the charger. While charging a green LED should light up, before shutting off at complete charge. The charger current at no load was measured to 11.4 mA.

The final test of the charging circuit was to connect the battery. Prior to charging battery voltage was measured to be 11.56 V. A test of current flow with battery connected indicated 0.2-0.3 A going in to the charger. There were, however, larger amounts of current, 0.6-0.7 A, just at the moment of closing the circuit. The battery has earlier been

charged at 0.6 A (2C) using a higher end LiPo-charger with no issues. Being just a burst of higher current this rose no immediate concern. Assuming an average of 0.25 A charging current estimated charging time from 0 to 100% for the 300 mAh battery is $\frac{0.3Ah}{0.25A} \approx 1.2$ hours

Five minutes in battery voltage was checked to confirm that it was actually charging. It then measured 11.64 V, 0.8 V greater than before the charging started. The battery was then left connected to complete the charging process, while battery temperature and other potential hazards were carefully monitored. A general observation was that all components seemed to operate at safe conditions, though the L7812 heated up beyond the point where it could be touched. While the voltage regulator automatically shuts down at too high temperatures (making the ”operate at safe conditions” comment a viable statement), it may not be suitable in the drone if heat is an issue.

1-1.5 hours later the charger shut off the green LED, indicating complete charge. Battery voltage was measured to be 12.64 V, with cells 1-3 at 4.22, 4.20-4.21 and 4.20-4.21 V, respectively. This is slightly over the 4.20 cell voltage one should expect, especially for the first cell, but yet a much better outcome compared to the BMS test.

The full test setup is shown in figure 6.4, with numbers referring to each component in table 6.2. A breadboard was used to house the L7812 and its associated wires, while a set of ’helping hands’ were used to keep the L7812 12 V output and ground separate.

Some comments on the Turnigy charger’s Hobbyking product page mentioned the battery draining while plugged in as a drawback. To test this the circuit was left as shown in figure 6.4, but with the receiver removed from the transmitter. In other words, no external power was supplied to the circuit. Battery voltage, after remaining plugged in to the circuit for 35 minutes, was measured to 12.62 V, a drop of 0.02 V. Some loss of voltage should always be expected, especially just after a complete charge, and so this was considered acceptable.

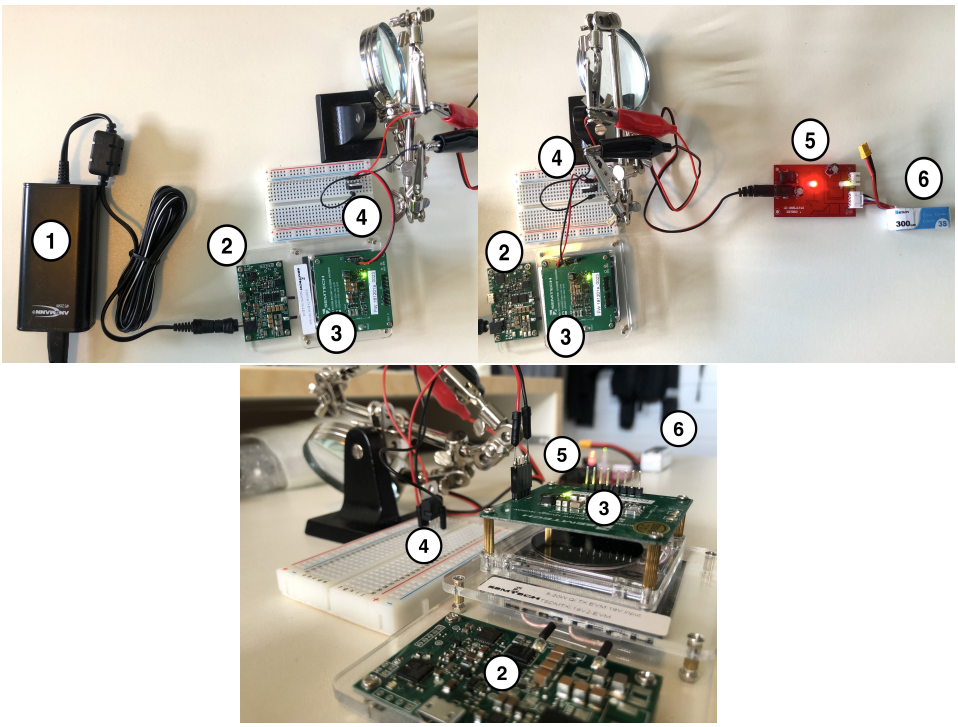

Figure 6.4: Pictures from the experimental setup of the inductive charging solution

Chapter 7

Component Manufacturing

All components were manufactured using the Ultimaker 3 Extended 3D-printer. The 3D-models were, as previously described, designed in Fusion 360 and prepared for 3D-printing using *Cura*. Cura is a software for working printer settings such as extruder temperature, printing velocity, support structure, and much more. Cura also estimates weight of the print, and this may slightly differ from what Fusion 360 estimates.
Below is a list describing some basic 3D-printer components/features, terminology, as well as basic settings in Cura.

- **Printer bed**
  The printer bed is the surface the 3D-object is created on. Ultimaker 3 Extended features a heated printer bed which is required when printing with certain materials, such as ABS.
- **Printer extruder/nozzle**
  The printer extruder/nozzle is the part where plastic is heated before being extruded on to the printer bed or the object on the printer bed.
- **Quality**
  Quality, or resolution, is determined by the thickness of each printed layer. Cura has pre-defined quality settings ranging from *extra fine* (0.06 mm) to *fast* (0.2 mm), but can also be set manually. Higher quality will result in increased printing time.
- **Material**
  The material setting in Cura is used to set the temperature of the nozzle and printer bed. A certain nozzle temperature is required to melt the material, but also for new layers to attach to already printed layers. Note that too high nozzle temperature will make the material too fluid, consequently messing up the geometry of the print.
  Printer bed temperature helps the print sticking to the bed, in addition to prevent it from cooling too fast.
- **Cooling**
  Cooling is basically a feature used to actively cool the printed layers. Too hot layers

makes it difficult for new layers to attach, while too fast cooling may cause *warping* in some materials. Cooling is set in the range 0 to 100%.

- **Warping**
  Warping often occurs when the material cools down too fast and starts contracting. This results in some parts of the print, often the corners, to lift from the printer bed. When that happens there is no way of continuing the print. Some materials, such as ABS, are more prone to this.

- **Brim**
  Brim is a software setting in Cura used to create a thin printed layer on the outer edges of the object to be printed. Using a brim improves printer bed adhesion for the 3D-object, preventing it from loosening. Basic brim settings are *brim width* and *brim line count*. Brim width and brim line count improves adhesion surface area and adhesion strength, respectively.

- **Infill**
  Infill is an option to reduce the weight of the object by filling only a certain percentage of a solid object. Infill must be seen in relation to wall thickness, since a 2mm thick solid object with 1mm wall thickness will have no leftover volume to fill.

- **Support**
  Support is a basic structure automatically generated by Cura if enabled. It prints additional structures to support overhanging parts of the 3D-object, preventing them from collapsing during print. The additional structures are fairly easy to remove upon completion of the print. Support is set as disabled/enabled with *support overhang angle* to specify at what angle (degrees) of overhang the supporting structure is to be applied.

To improve printer bed adhesion hair spray was sprayed on the printer bed just prior to the start of the printing.

Further down is a discussion on the 3D-printer material options, followed by descriptions on the process of printing each component.

7.0.1 Material selection

Two types of material were available for the print - ABS (*Acrylonitrile butadiene styrene*) and PLA (*polylactic acid*). PETG (*Polyethylene Terephthalate Glycol-modified*) is also a fairly common material used in 3D-prints, but was not considered in this project.
Some physical properties of the two materials considered are summed up in table 7.1 (Singh et al., 2019)(Simplify3D).

Property	ABS		PLA	
	Value	SD	Value	SD
Density (g/cm^3)	1.04		1.24	
Young's modulus (*MPa*)	175 ± 0.11	0.09	47.9 ± 0.10	0.08
Yield stress (*MPa*)	0.49 ± 0.21	0.17	0.27 ± 0.16	0.13
Glass transition temp. ($^\circ C$)	109.76 ± 0.2	0.16	62.57 ± 0.21	0.17

SD = Standard deviation

Table 7.1: Some physical properties of ABS and PLA (Singh et al., 2019)(Simplify3D)

From table 7.1 one can first of all see that ABS will give a lighter print than that of PLA, roughly 85% of a PLA print. The strength properties, *Young's modulus* and *yield stress*, are also better with the ABS. Young's modulus is basically a measurement of how well the material can withstand deformation, while yield stress is the stress point when the material enters plastic deformation. Beyond yield stress comes ultimate strength (not listed in the table), the point where the material breaks. The values for this are 40 and 65 MPa for ABS and PLA, respectively (Simplify3D). In other words, it will take more for PLA than ABS to break. It is, however, unacceptable for the drone to enter plastic deformation (yield stress) in the first place, and so, 'strength wise', ABS is superior to PLA for this application.
The final physical property listed is the glass transition temperature. This is the point where the material will start loosing some of its physical properties, and can be visualised as the heated surface of a piece of plastic taking a glass-like look. Above this temperature the Young's modulus of the material will be reduced, making it less resistant to plastic deformation. From table 7.1 one can once again see the superiority of ABS to PLA, with close to double the glass transition temperature.

There are still some advantages with using PLA in 3D-printing. First of all, it is bio degradable, and therefore an environmentally friendly solution. It must, however, be mentioned that ABS is recyclable. Secondly, PLA is generally an easier material to print with. Required printing temperatures are lower than that of ABS, and warping is usually not a problem.

With all differences between the two types of material in mind, ABS appear as the better choice, at the cost of a slightly more challenging print. The lower density and higher glass transition temperature are two very desirable features in a light drone carrying components that can reach higher temperatures (such as the ESC).

7.0.2 Printing of the frame

The frame was the first part to be printed, but not without challenges, and a total of four attempts were made. Below are descriptions of the process in printing the frame. Settings were set as default/recommended by Cura, unless specified otherwise. *Brim* settings were in all frame prints set to 2 mm brim width and *brim line count* 5. Ideally the brim width would be larger, but due to dimensional limitations on the 3D-printer printing bed this was not possible.

Printing attempt #1

- **Material:** ABS
- **Quality:** Fine (0.1 mm)
- **Nozzle temperature:** 220 °C
- **Printer bed temperature:** 60 °C
- **Cooling:** Disabled
- **Infill:** 20% (likely no effect)
- **Support:** Enabled, 60° overhang angle
- **Estimated printing time:** 26 hours, 52 minutes
- **Estimated weight:** 76 g

As ABS was used it was important to avoid too rapid cooling, and so active cooling was disabled. In addition, openings on the 3D-printer were covered where possible in order to avoid heat escaping. The first attempt started off with no issues, and visual inspection showed no sign of problem with adhesion or warping. This was, however, only during the first layer, and so it was unlikely to spot any defects either way.
The print was started in the evening, and continued overnight. In the morning after someone on the premises where the 3D-printer was located reported a failed print. At approximately 2-3 millimeters frame height the print had started warping and was pushed out of the printer by the moving nozzle. The rest of the printing process, until stopped in the morning, was done loosely in the air, resulting in nothing but loose plastic threads.

Printing attempt #2

It was suggested that printer bed adhesion was too poor in the first attempt. This seemed plausible, partly considering the forced reduction in brim width. The hair spray for adhesion used was also not the same as normally used with that printer. Therefore, the ”correct” hair spray was used in the second attempt. No changes were made to the settings.
Only a few hours in the print failed again, at a height similar to the previous attempt. Once again, poor printer bed adhesion and warping seemed to be the cause. In retrospect, increasing printer bed temperature would possibly be a better response to the failure of the first attempt, rather than just changing hair spray type. This would possibly have prevented the print from cooling too fast, a common cause for warping.
As the failures in the first two attempts were typical failures to expect with ABS it was decided to move over to using PLA in further attempts. This simplifies the printing process by reducing risk of warping, but, as discussed earlier, at the cost of poorer physical properties.

Printing attempt #3

- **Material:** PLA
- **Quality:** Fine (0.1 mm)
- **Nozzle temperature:** 200 °C
- **Printer bed temperature:** 60 °C
- **Cooling:** Enabled, 100%
- **Infill:** 15% (likely no effect)
- **Support:** Enabled, 60° overhang angle
- **Estimated printing time:** 26 hours, 15 minutes
- **Estimated weight:** 84 g

With PLA comes reduced need of higher temperatures, and so the nozzle temperature was reduced to 200 °C. Cooling was also enabled at 100% to ensure rapid cooling so that new layers attach easier. With the low risk of warping when using PLA this was considered safe and appropriate.
Again, there were no initial problems with the print. When checking in on the print roughly 7 hours in, beyond the point of failure in the first two attempts, there were still no issues. However, about one hour later is was yet again reported by others on the premises that the print had failed. This time it appeared that the new layers of plastic were not attaching to the already printed object.
The cause of failure this time was concluded to be due to the nozzle temperature being too low. As earlier mentioned the plastic needs to be heated to a certain temperature for it to attach to the existing structure.

Printing attempt #4

- **Material:** PLA
- **Quality:** Fine (0.1 mm)
- **Nozzle temperature:** 210 °C
- **Printer bed temperature:** 60 °C
- **Cooling:** Enabled, 100%
- **Infill:** 15% (likely no effect)
- **Support:** Enabled, 50° overhang angle
- **Estimated printing time:** 26 hours, 21 minutes
- **Estimated weight:** 84 g

The main response to a failed third attempt was to increase nozzle temperature by 10 °C, to 210 °C, in order to ensure proper attaching of new layers. Support overhang angle was also reduced from 60° to 50° to ensure better support, since warmer plastic takes a more fluid state and could potentially mess up the geometry.
Increasing nozzle temperature appeared to be the right measure to take, as the fourth attempt yielded a successful print and a drone frame with no obvious defects.

Evaluation of the finished drone frame

In order to evaluate whether a new design or print was necessary, some immediate observations of the materialized drone frame design were made:

- Each component of the frame (i.e. shrouds, motor slots etc.) appear as very solid.
- The weakest parts appear to be the poles holding the flight controller, but they caused no immediate concern.
- The thin parts connecting motor slots to shrouds appear fairly rigid, though grainy and printed with low resolution.
- The frame is very flexible on the diagonal (when grabbing two shrouds on the diagonal and folding them upwards), and there is a chance that too much force may cause damage. During flight all shrouds will normally have some force applied simultaneously, and so damage from too much force on one diagonal only seems unlikely.
- Mounting holes for motors, ESC and FC were very tight, and had to be worked on in order to expand them.

Despite some minor faults in the design it was concluded as functionally fit for its purpose.

However, since the frame was manufactured with a material of physical properties that may not suit the application perfectly, it was necessary to investigate critical weaknesses and potential improvements.
ABS has three general advantages over PLA; strength, weight and heat tolerance. Neither simulations nor visual inspection caused any concern for the strength of the PLA printed frame (simulations were done using ABS, but the high minimum safety factor ($\sim$7) means a weaker material is likely acceptable). The additional 8 grams gained with PLA cannot be eliminated without physically removing material through revision of the design or forcefully modifying the frame post printing.
The main concern was in the poor heat tolerance of PLA ($\sim$60 °C glass transition temperature). There are mainly two components that may cause heating beyond PLA tolerance - ESC and motors. One might also consider the battery a potential excessive heat source, but a LiPo-battery passing 60 °C will raise other concerns than just plastic deforming.
Unfortunately, there seem to be no specifications on operating temperature for the components used in this drone. There are, however, numerous forum discussions regarding the general advice on the temperature of drone components. These share valuable knowledge and experience, such as one discussion on *RCUniverse.com*, started by *StarscreamF22*

(StarscreamF22/RCUniverse, 2014). This particular discussion was regarding an RC car, but the concept remains the same as in a drone (LiPo-battery powers ESC, which in turn power and control motors). After 15 minutes only the RC car motors went beyond 60 °C (81 °C), while the ESC and battery kept well below, at 47 °C and 39 °C, respectively. Further reading on that particular discussion reveals generally accepted operating temperature for these three heat generating components:

- **Motors:** $<$71 °C
- **Battery:** $<$49 °C
- **ESC:** $<$65 °C

Similar temperature limits for these components are verified in other forums, such as in *RCGroups.com* (Stanbur/RCGroups, 2017). As these temperatures are repeatedly described as maximum operating temperatures, it seems safe to say that, without testing, the components in this setup will not exceed these limits. Still, the limits for motors and ESC are above acceptable for the physical property limitations of PLA. There are, however, some arguments why this will not be an issue:

- Motors and ESC are distanced from the frame through *soft mounts*
- The ESC in this particular setup features a heat sink
- Component temperature limits are for the surface temperature of the components, not the surroundings, which will experience lower temperatures
- The air surrounding the motors is constantly cooled/replaced by the propellers
- Racing drones safely fly at speeds and pull amperage far greater than what is necessary or recommended for the given application of this drone

A different approach to the issue is to improve the physical properties of the PLA, for example through *annealing*. Annealing means re-structuring the macro molecular structure of the material, from *amorphous* ("chaotic" structure, weaker performance) to *semi-crystalline* or *crystalline* (semi-structured/structured, better performance)(Kočí, 2019). This is done by heating up the finished print. Annealing PLA at 90 °C gives incredible results, and can move the glass transition temperature up from 60 °C to $\sim$110 °C, making it perform even better than ABS (Kočí, 2019). The drawback of annealing PLA at these temperatures is the deformation it causes to the geometry. Annealing the whole frame will likely ruin the geometry of it, and should therefore only be considered for simple standalone parts.

Further options for improving the physical properties of PLA, or methods of reducing heat transfer to the frame, were not considered at the time. It is recommended that the frame will be made from the far better type of ABS, or any material with similar/better qualities, in the future, and therefore not necessary to spend resources on improving the current, temporary prototype. In addition, with the arguments listed above, it seems unlikely that the PLA prototype frame will take any immediate damage from heat. The printed frame

was therefore evaluated as a suitable prototype for testing. In later designs including the wireless charging solution PLA may, however, not work due to the heated L7812 buck converter.

7.0.3 Printing of sensor chamber and LiDAR mounts

The sensor chamber and LiDAR mounts are far smaller than the frame, and were therefore printed together. Their smaller size also meant that brim size could be increased, and so this was set to 5 mm. The frame was quite challenging to remove from the printer bed upon completion, and so brim line count for this print was reduced to 3 for reduced brim strength.

Printing attempt #1

- **Material:** PLA
- **Quality:** Fine (0.1 mm)
- **Nozzle temperature:** 210 °C
- **Printer bed temperature:** 60 °C
- **Cooling:** Enabled, 100%
- **Infill:** 15% (likely no effect)
- **Support:** Enabled, 50° overhang angle
- **Estimated printing time:** 7 hours, 52 minutes
- **Estimated weight:** 31 g (sensor module, 1x downward facing LiDAR, 3x forward/side facing LiDAR)

With the successful print of the frame in mind it seemed reasonable to print the sensor chamber and LiDAR mounts with the same settings.
As expected, the print carried through with no issues on the very first attempt.

Evaluation of the finished sensor module and LiDAR mounts

The following observations were made on the completed modules:

- All modules came across as very rigid, causing no concern for them breaking.
- The supporting structure inside the ducts of the sensor chamber will be very challenging, if not impossible, to remove.
- The visualised technique for mounting the modules to the frame did not work, as the material is far too rigid.

While some of these observations were unfortunate, some workarounds exist.
The slots for attaching the modules to the frame can simply be removed, and the components can be glued on.
When it comes to the inaccessible supporting structure in the ducts, it was possible to remove *some* of it. The ducts are not completely blocked, and so it is still possible to test the concept to some degree. Worst case fix is to break the ducts off, remove supporting structure, and glue them back on.
As none of the components are critical for the drone, and they were still usable, though limited, there was no immediate need to re-design and print again at the cost of reduced progress on the project.

Chapter 8

Drone Assembly and Completion

The assembly and completion of the drone is divided in a hardware and software section, describing the process and challenges of the setup.

8.1 Hardware

During assembly of the hardware and the frame some challenges were encountered:

- Motors were not flat under. They could therefore not be mounted flat on the motor slots, but rather had to be balanced by tightening/loosening the mounting screws.
- Mounting holes for ESC and FC were too small, despite earlier efforts on expanding them. The ESC holes were widened using a screwdriver and some force. This was not possible on the FC mounting holes as too much force would break the poles. A soldering iron was therefore used to melt away some material (not recommended as it damages the soldering tip).
- The receiver box proved to be just a bit too narrow for the receiver to fit. That was unfortunate, since the solution seemed perfect otherwise. The box was therefore removed by force to create space, leaving some left-over material still stuck to the frame. There was no longer a plan for properly fitting the receiver to the drone, and so double sided tape was used.
- All propeller sets are mounted on the motor shaft by force. Only one out of three sets of propellers would stick to the motor shaft.

Soldering was necessary for connection between motors and ESC, and receiver and FC. This was done using Dibotech Soldering Station 60 W, heated to 380 °C, and 0.5 mm solder. With limited experience on soldering to solder pads, like the ones found on the ESC and FC, this came with some challenges as well:

- A pointy soldering iron tip was used at first, but deemed unsuitable when trying to apply solder to the solder pads. An inclined flat tip made the process far easier.

- The solder is far from perfect, but it was decided to stop before damaging any components since a number of attempts had already been made with the pointy iron tip. Light pulling of the wires was performed and connections were concluded to be rigid. No overlapping solder causing short circuits or bridging solder pads was observed.

In addition, a 35 V 330 μF smoothing capacitor was soldered accross the power input terminals of the ESC.
The frame equipped with necessary hardware (excluding battery) ended up at 151 g.

8.2 Software

The first step in the software process was downloading Betaflight and installing the CP210x drivers. Next, the FC was connected to the PC in bootloader mode and flashed with MATEKF722SE firmware.

The borrowed Taranis X9D Plus came with non-EU (FCC) firmware, while the receiver, FrSky R-XSR, had the EU (LBT) version. It was therefore necessary to update the receiver to non-EU firmware, and so the latest non-EU ACCST D16 release (2020-03-24 v.2.0.1) was flashed to the receiver. This was done by uploading new firmware to a MicroSD-card that was inserted to the transmitter, and then flashing the receiver via the transmitter.
Despite both transmitter and receiver having non-EU firmware there was trouble binding. After much troubleshooting it seemed likely that this was due to a mismatch between the versions of receiver and transmitter firmware (Spychalski, 2020).
The receiver was then downgraded to the ACCST D16 2019-11-28 (FCC) update. A new attempt was made at binding receiver and transmitter, this time with no issues encountered.

8.2.1 Betaflight setup

With a working receiver, as well as having all other hardware mounted and connected, the first setup in Betaflight was started. The first round of configuration was done using Oscar Liangs guide as base, with modifications where this was seen fit (Liang, 2018a). The Betaflight Software is built up of several tabs, and the setup process for each tab is explained further on.

SETUP TAB

The drone was placed on a leveled surface and accelerometer calibrated. Proper calibration was tested by rotating the drone around, verifying that the movements matched the Betaflight live 3D-model of the drone.

PORTS TAB

The *PORTS* tab is used to setup UART communication in the FC. Prior to the first flight it was only seen necessary to ensure communication between receiver and FC. The SBUS

protocol receiver was soldered to UART2 on the FC, and so SerialRX was enabled on UART2.

CONFIGURATION TAB

The *CONFIGURATION* tab is used to configure all hardware on the drone.

Motor configuration. It was verified that the physical motor configuration matched the configuration in Betaflight. Configuration was set to QuadX.

ESC configuration. Regarding protocol, the 32-bit processor allows for use of Dshot1200. However, support for this has been removed from Betaflight, and so Dshot600 was used. The number of motor poles was set to 12, according to the specifications of the motor. Other ESC settings were kept as default.

System configuration. These were, to some degree, set random, as it is a matter of experimentation. The initial setup was:

- **Gyro update frequency:** 8 kHz
- **PID loop frequency:** 4 kHz
- **Accelerometer:** Enabled
- **Barometer:** Enabled
- **Magnetometer:** Disabled (no magnetometer on FC)

Gyro update and PID loop frequencies will be experimented with using 2, 4 and 8 kHz. While the F7 processor FC allows for it, 32 kHz is not available in Betaflight, as they argue it shows no improvement over 8 kHz. Gyro update frequency is the frequency at which the gyroscope sample its readings, while PID loop frequency is the frequency at which the FC runs through the PID loop. A common relationship between the two settings is to keep gyro update frequency twice the PID loop frequency. Keeping the frequencies low will free some workload on the CPU and reduce noise, and it is recommended to keep CPU load below 30%. However, with the F7 processor it should be able to handle high frequencies. In addition, if the build is not that prone to vibration and noise, high frequencies may improve the flight experience as the current state of the drone is updated and regulated more frequently. This should all be seen in correlation to power consumption as well.
The accelereometer is not required in all flight modes, but was kept enabled to observe how the drone behaves when utilising all features available. The same goes for the barometer.

Receiver. Since using the FrSky X-XSR receiver with SBUS signal, receiver mode was set to *Serial based receiver* and serial receiver provider to *SBUS*.

Other features. The *Other features* section presents enable/disable options for a number of additional features. The following were enabled in the first configuration, much on recommendation from Oscar Liang's guide:

- **TELEMETRY** - Enables telemetry
- **ANTI-GRAVITY** - Temporarily boosts the integral in the PID controller with sudden throttle increase for improved control in such cases (and is therefore mainly advantageous for more acrobatic flights)
- **AIRMODE** - Basically allows the pilot to have some control of the drone when throttle is set to zero by keeping the PID loop active even at zero throttle.
- **DYNAMIC FILTER** - Detects the frequency of noise and reduces noise based on these dynamic detections

RECEIVER TAB

The *RECEIVER* tab provides a user interface to verify that controller commands are received and interpreted as intended.
First it was verified that the first four channels, throttle, yaw, pitch and roll, responded to the controller stick movements as intended.
Secondly, midpoints and endpoints were fixed. These should range from 1000 to 2000, with midpoint at 1500. This was done using a combination of the *OUTPUTS* tab on the controller and the CLI (*Command Line Interface)* in Betaflight (Ash, 2017). There were some difficulties in tuning it, and so *Extended limits* had to be enabled on the controller. Endpoints were, eventually, managed to set as 1000 and 2000, with midpoints at 1500.

MODES TAB

The *MODES* tab allows use of available channels to adjust features in-flight.

ARM mode was set to auxiliary channel 1, associated with a three-way flip switch on the controller (only a two-way flip switch is necessary). The switch was then used to arm/disarm the motors for safety purposes.
Flight modes *ANGLE* and *HORIZON* were set to auxiliary channel 2, on a three-way flip switch on the controller:
Neither mode activated - Horizon mode activated - Angle mode activated

PID TUNING TAB

Default values for tuning were kept, as these are often acceptable. Observations during flights will help pinpointing how PID values should be further tuned. Some other modifications were made, though, to ensure a safer first flight. These parameters do not change the behaviour of the drone, but are rather just parameters that alter the relationship between controller and drone.

- RC Rate was reduced as higher RC rates make the drone more responsive and sensitive to stick movements. Not knowing how the drone behaves during the first flight, too sensitive sticks may be unfortunate.

- RC Expo at 0%. This means that the motors respond linearly to stick movements. Increasing RC Expo introduces an exponentially increasing relationship between motor response/sensitivity and controller stick movement. In other words, small stick movements are less sensitive, but as the sticks are moved further from the centre it becomes more sensitive.
- Throttle expo increases throttle resolution at throttle mid. Throttle mid is by default at 0.5, but will eventually be set to throttle used at calm cruising speed, to increase resolution around this point.
- TPA (Throttle PID Attenuation) basically reduces PID values at the throttle TPA break point. This can help reduce vibrations, and may later be applied when discovered at what throttle value vibrations start appearing.

MOTORS TAB

The *MOTORS* tab was used to verify that the motors actually are in an order that matches the order set in Betaflight, as well as motor direction of rotation. This was tested by powering each motor separately, battery connected and no propellers (for safety purposes), using throttle sliders in the Betaflight software.

The first test showed that all motors would respond to the sliders, but in the wrong order and wrong direction of rotation.
Changing motor direction was solved by desoldering any two out of three wires on each motor and swapping their place on the ESC.
Motor order was changed using the CLI. Step one was to determine the current pin assignment for each motor by typing

```
resource
```

When the current pin of each motor had been revealed, the motors were swapped around and allocated to the correct pins. Using `MOTOR 1` and pin `B06` as an example, this was done by typing

```
resource MOTOR 1 B06
save
```

After swapping motor wires and re-mapping the motors the throttle sliders were again used to confirm correct motor order and direction of rotation. With motors functioning as intended, that concluded the Betaflight configuration.

Chapter 9

Test flights

Following are descriptions of a number of flights conducted. Not all are included as some were not meant for a full analysis of the flight performance. Data was collected using the built-in MicroSD-card slot in the flight controller and a *FAT32* formatted MicroSD-card. Graph analysis was done using Betaflight Blackbox Explorer.

9.1 Test flight #0

Propellers: HQ Durable Prop T2.5X3.5X3
Test flight #0 is in reality one of those flights conducted without the aim of full flight analysis. It is still included as this was the starting point for further flights.
All settings were as default in Betaflight, unless specified otherwise in the previous chapter. The default PID-values used in test flight #0 are shown in table 9.1.

	P	I	D
Pitch	46	90	38
Roll	42	85	35
Yaw	30	90	0

Table 9.1: Flight #0 tune

After several rounds of minor changes in Betaflight the first flight was launched, and the following observations and impressions were made:

- There appeared to be large amounts of vibration as the drone was experienced as noisy. The nuts on the bolts holding the FC also started to loosen, as well as the ESC heat sink (which apparently has not been properly attached to the ESC)
- There was noticeable drift in negative pitch (backward drift)

- Horizon mode seems a good mode for the first flights as it gave a fairly manageable control experience in the horizontal plane

There are a couple of possible reasons for the drift:

- Drone was calibrated while not resting perfectly horizontally
- Noise on the gyro

Uneven flight controller calibration seemed reasonable as the drone is not perfectly flat underneath. It can therefore not be calibrated properly by just resting it on a flat surface, as was done in the first round of calibration. After a review of the blackbox flight log, figure 9.1, gyro noise seems a plausible contribution to the drifting as well.

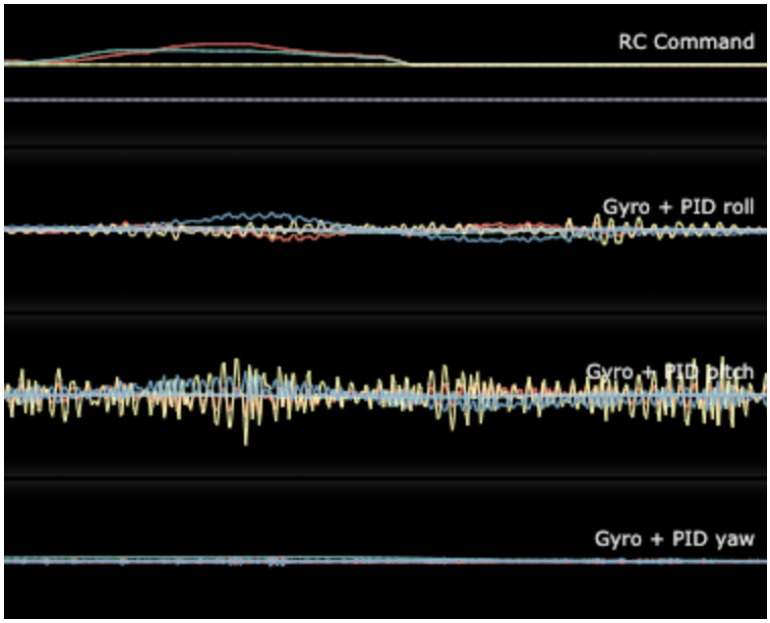

Figure 9.1: Gyroscope readings from flight #0

While yaw suffers little to nothing from noise there are indications of noise on the roll, and even more so on pitch. The most noticeable noise is on the *derivative* of the pitch PID regulator (yellow).

Possible measures to take before the next flight:

- Re-do FC calibration, ensuring perfectly even surface
- Tighten bolts
- Reduce D in the pitch PID controller
- Reduce gyro sampling frequency
- Adjust filtering

9.2 Test flight #1

Propellers: HQ Durable Prop T2.5X3.5X3
Prior to flight #1 the FC was re-calibrated, bolts were tightened and the derivative of the pitch PID controller was reduced from 38 to 20.

	P	I	D
Pitch	46	90	20
Roll	42	85	35
Yaw	30	90	0

Table 9.2: Flight #1 tune

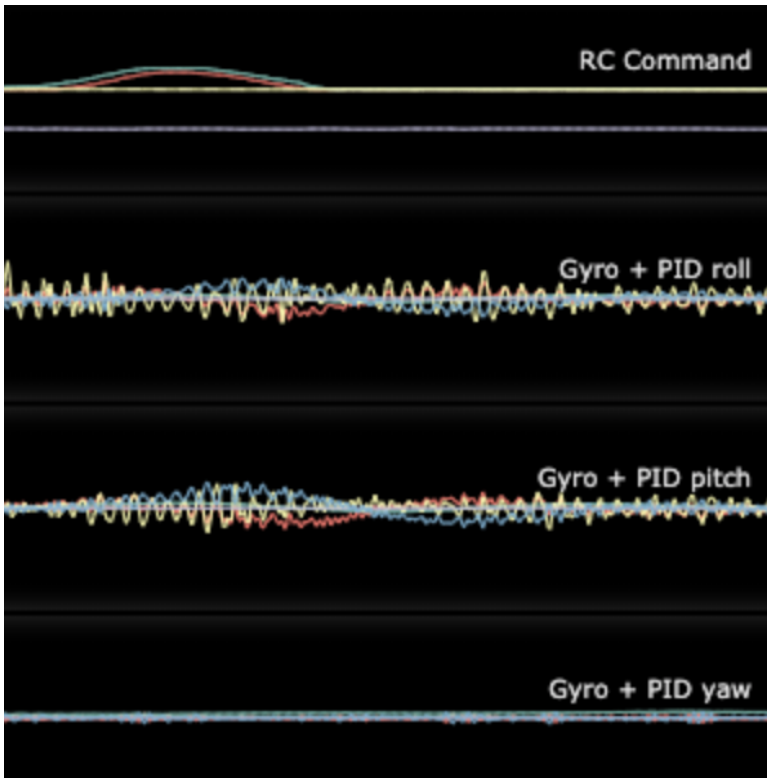

Figure 9.2: Gyroscope readings from flight #1

As figure 9.2 shows reducing D for pitch had a clear effect on the gyro noise, as it is now reduced to noise levels similar to that of the roll.
However, noise levels for both pitch and roll are still unacceptable, and one can not continue reducing the derivative indefinitely as this will likely reduce flight performance as well.

9.3 Test flight #2

Propellers: HQ Durable Prop T2.5X3.5X3
No change in PID values.
Prior to test flight #2 noise was attempted reduced using notch filtering. The Betaflight Blackbox Explorer identify frequencies causing excessive amounts of noise in the gyro, and this is shown, for pitch, in figure 9.3. A similar plot was seen for roll noise.

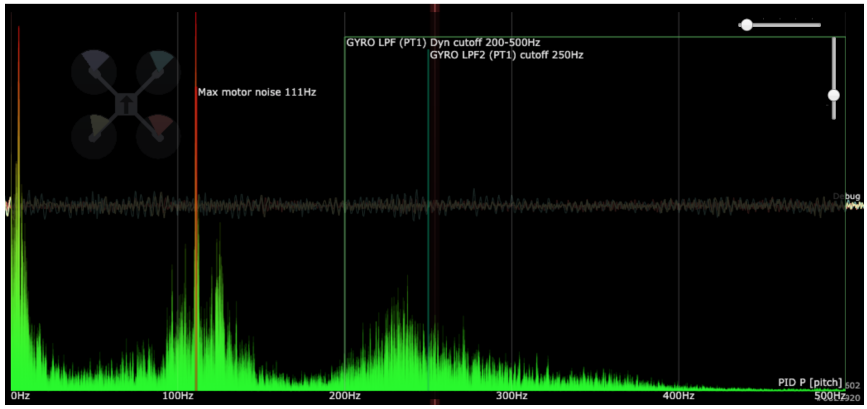

Figure 9.3: Frequencies of excessive noise from flight #1

The plot shows a peak at 111 Hz, followed by another at $\sim$230 Hz. Notch filtering was therefore applied with a centre at 230 Hz and a range of $\pm$60 Hz. The notch filter will drastically reduce gain at 230 Hz in order to dampen high frequency noise, and increase gradually to normal gain at 230 $\pm$ 60 Hz.
Figure 9.4 below show the pitch noise plot after activating the notch filter described.

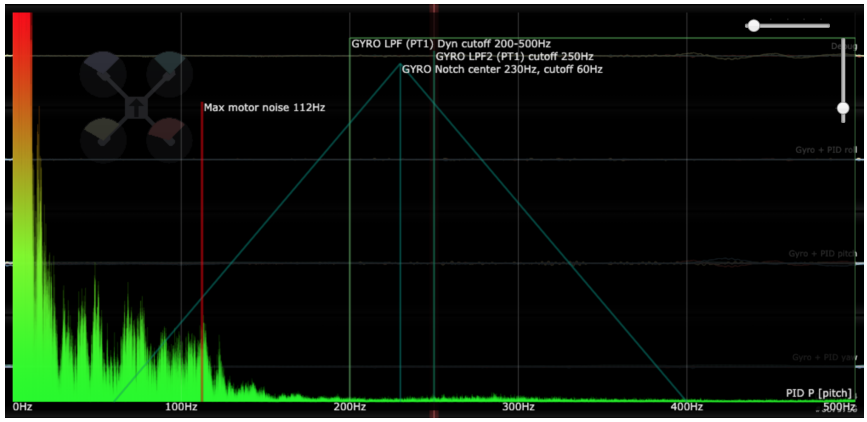

Figure 9.4: Frequencies of excessive noise from flight #2

As one can see, the notch filter had an incredible effect on noise reduction at the fre-

quencies discussed above, as it is now more or less eliminated. The same was seen for roll noise, whereas yaw noise was practically gone. The filter improved flight experience, and its effect is backed up by the new gyroscope plot in figure 9.5 below.

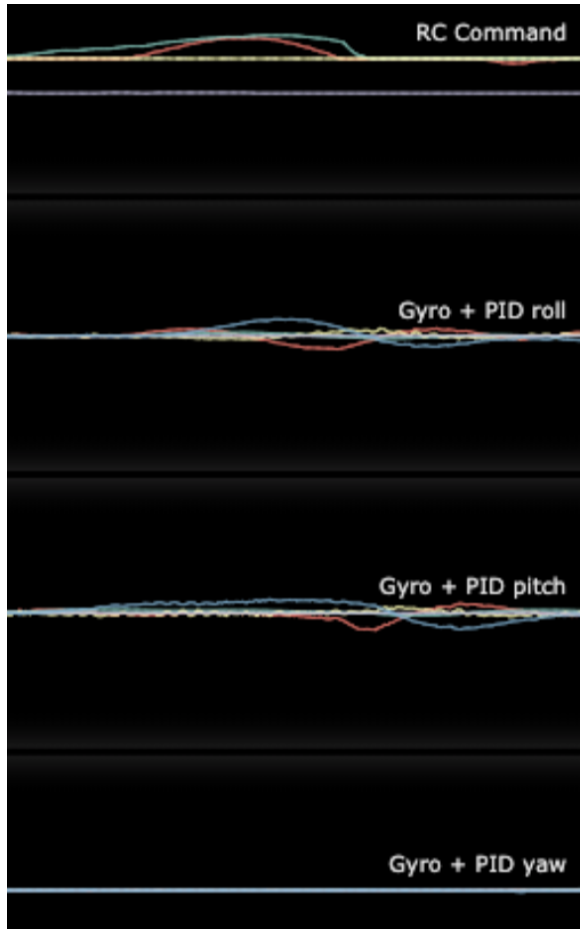

Figure 9.5: Gyroscope readings from flight #2

9.4 Test flight #3

Propellers: HQ Durable Prop T2.5X3.5X3
No change in PID values.
Test flight #3 aimed to estimate hover flight time. The following measures were taken to reduce power consumption, while expecting the same flight experience as before:

- Barometer disabled
- Gyro update frequency set down from 8 kHz to 4 kHz

- PID loop frequency set down from 4 kHz to 2 kHz

The barometer never had a practical function in the prior flights, while gyro and PID loop frequencies were reduced in order to reduce processor power consumption. Possible side effects of this is reduced noise, but also reduced flight accuracy. Still, the set frequencies should be acceptable. The measures taken reduced estimated CPU load from $\sim$5% to $\sim$2%.

With limited flight experience it was challenging to maintain hover at all times. It was therefore necessary with small corrections in altitude, pitch and roll throughout the flight. The flight was ended when a propeller loosened and the drone crashed. Two arms connecting motor slots to the shrouds broke from the crash, but were later glued back on.
After the crash battery voltage was measured to be 11.28 V, or 3.76 V per cell. A rough recommendation is that cell voltage does not go below $\sim$3.5 V. In that sense, it would therefore have been possible to hover for some more time if the propeller had not loosened. However, other sources say that cell voltage should not go lower than $\sim$3.75 V (80%) (Salt, 2020). According to this flight #3 safely utilised all power available.

The Betaflight Blackbox Explorer showed a flight time of approximately 2 minutes and 15 seconds, close to the estimated flight time in equation (5.2) (2 minutes and 26 seconds). Motors were reported to operate at $\sim$35% when hovering.
It was, as mentioned, difficult to maintain constant hover, and therefore difficult to conclude on power consumption at hover. The Betaflight Blackbox show currents alternating between $\sim$5.5 A and $\sim$6.5 A, with dips and peaks at about 4.5 A and 7.5 A, respectively. This is close to the earlier estimated current consumption of 5.90 A, using *method 2* with a given motor efficiency. In terms of power consumption Betflight Blackbox does not have an option for investigating this. A few selected current and voltage data sets were therefore used to estimate power consumption:

Current	**Voltage**	**Power**
5.58 A	10.83 V	60.43 W
6.14 A	11.06 V	67.91 W
4.80 A	10.96 V	52.61 W
5.64 A	11.02 V	62.15 W
5.86 A	10.77 V	63.11 W
Avg.: 5.61 A	**Avg.**: 10.93 V	**Avg.**: 61.24 W

Table 9.3: Selected sets of current and voltage consumption during flight #3

Once again, this is in the area of the earlier estimated 65.46 W, and confirms the thrust test based *method 2* as a better approach than the mathematically derived *method 1* when estimating power consumption.

When it comes to flight experience there was no noticeable change with the reduced gyro and PID loop frequencies. Gyroscope readings show that noise now might come at a slightly lower frequency, as shown in figure 9.6, but the difference is minimal.

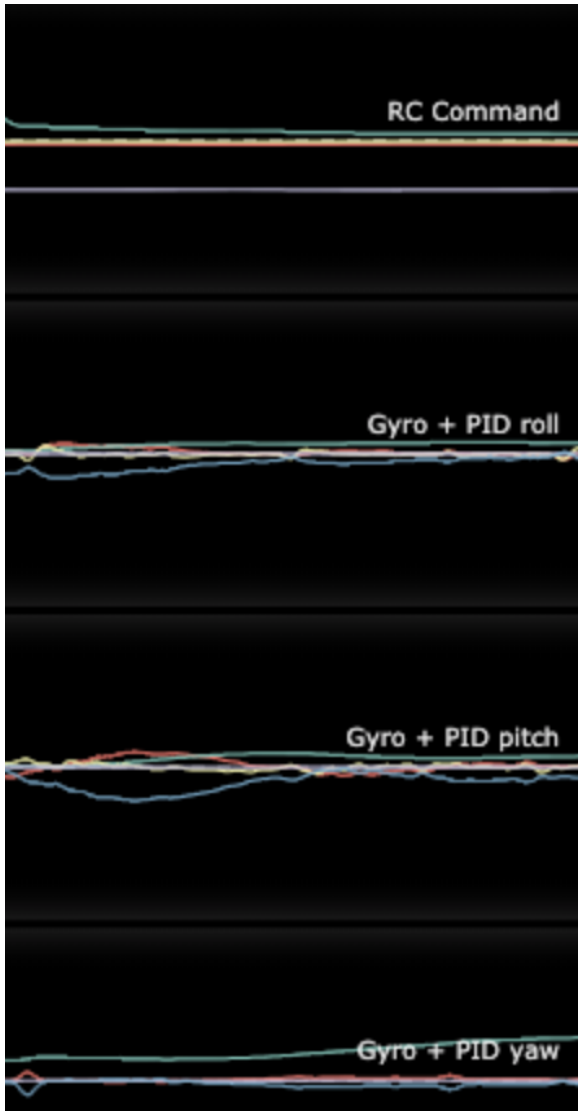

Figure 9.6: Gyroscope readings from flight #3

9.5 Test flight #4 / Troubleshooting

Propellers: Gemfan Flash 2540 Durable 3-blade

Just prior to flight #4 some re-soldering was done, as well as gluing a new set of propellers to the motor shafts for a more or less permanent propeller solution (since the previous set had a loose propeller). When arming the drone motors spun for a short second, before

shutting down with a small cloud of smoke emerging from the centre front area of the drone.

Immediately after the smoke appeared the battery was removed and safely stored in a LiPo-charging bag.

It was deemed necessary to troubleshoot the problem, whether for the purpose of replacing damaged parts and continue experiments or to learn the weaknesses of the construction. Initial troubleshooting revealed the following:

- No obvious visual damage to the battery. It would, however, not charge (charger display read ”Connection break”).
- No visual short circuits due to poor soldering.
- No visual damage to the components of the ESC.
- Both battery and front motor, left hand side, had a distinctive smell.

Being at the end point of power flow, it seems plausible for the front-left motor to be the root cause of the problem.
Considering the location of the emerging smoke it seemed likely that either the battery, smoothing capacitor, ESC of FC was damaged as well, indicating that replacing the motor would not be sufficient.
Further troubleshooting, first by connecting the FC to the computer, revealed that it was still working. The smoothing capacitor, showing no visible damage, is rated at 35 V, more than the battery can supply. Looking back to current ratings in the *Hardware chapter*, the current rating of the battery (45/75C = 13.5/22.5 A) is far less than that of the ESC (35 A). A built in fuse in the battery, or simply damaging amounts of current, may therefore have saved the ESC.

These theories were attempted confirmed by use of a multimeter.
Front-left motor was tested by spinning the motor by hand and measuring the AC voltage across all combinations of the three wires, similar to a generator. It was challenging to determine whether the motor was faulty or not, as all motors appeared to generate small amounts of voltage. In case there is interest in using the same motors for future flights it is recommended that all motors are desoldered and run directly from a power source for testing, since motor troubleshooting was rendered inconclusive.
Testing the **ESC** was even more challenging, as plausible faults could be in a number of locations and since the components are very small in size. Attempts were, however, made at measuring resistance on the MOSFETs, especially those associated with the suspected faulty motor. Again, it was difficult to arrive at a conclusion, and no further attempts at troubleshooting by use of multimeter were made.

Maintaining the assumption of the motor being the root cause of the problem it would be very beneficial to determine exactly what caused it. While it could simply be a faulty design, one can not ignore the possibility that some of the glue used to attach the propellers has entered the motor bell. This opens the possibility for the other motors to fail in

the same manner at a later point, as all had their propellers glued on. With glue reducing rotational freedom in the motor more current is consumed in an attempt to spin the motor at a desired speed. Alternatively, the glue has somehow short circuited the motor. It was, however, possible to rotate the motor bell by hand (possibly with slightly more friction compared to the others).

With no other plausible theories, it was difficult to conclude on exactly what caused the drone to fail. It was decided not to make further attempts at flying, due to both limited time remaining on the project and uncertainty as to what pushed the drone into critical failure. Unfortunately, it was therefore not possible to test all aspects of the drone. Some of these are presented next, along with a theoretical approach on how they could have been researched/tested/solved.

9.6 Remaining aspects for testing

As implied in the flights #0 and #3 descriptions, the issue of a drifting drone was a problem that had carried on throughout all flights, particularly with regards to pitch.

As a first step of investigating the drifting issue a unit step response for the drone with the current PID-values was plotted in MATLAB, using the earlier derived equations (2.32),(2.33) and (2.34). The results are shown in figure 9.7.

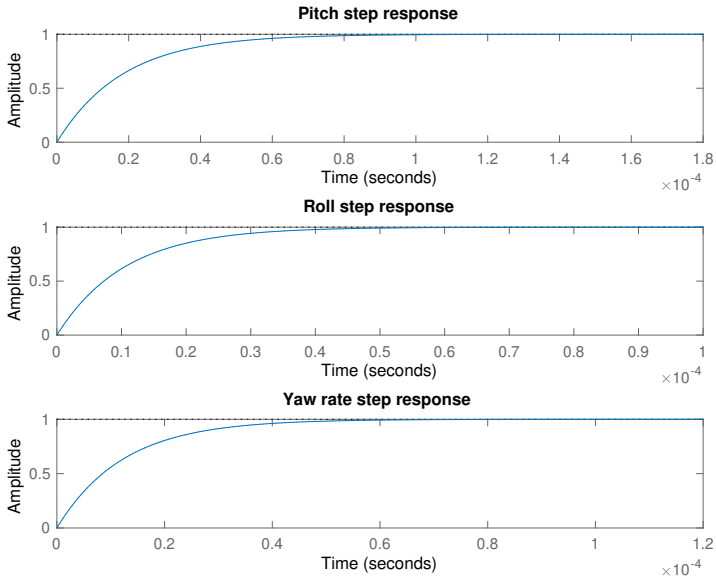

Figure 9.7: Pitch, roll and yaw step responses to current PID-values

The plots suggests very fast response and no steady-state error. While the response felt fast, there certainly was a degree of steady-state error. It therefore seems likely that either the earlier derived mathematical model for a PID-regulated drone fails to capture the full complexity of drone control, or then the drifting issue lies elsewhere.
Attempts at discovering alternative PID values were made using MATLABs PID-tuner tool, launched by the command `pidTuner(sys,type)`. `sys` is the plant to be controlled and `type` is the controller type. Sliders in the PID-tuning tool are used to control response time and robustness/aggression, alternatively bandwidth and phase margin. Depending on slider values, a live unit step response plot for the plant can be seen in the tuning tool, in addition to corresponding PID-values, settling time and more.
No other PID values appeared to give a much better response than the current values. However, still assuming that poor tuning causes drifting and that the derived mathematical model is too inaccurate, one should expect the experienced steady-state error, i.e. drifting, to reduce or vanish with an increased I (integral) value in the PID-controller.

Another feature not tested was the sensor chamber and its air ducts. Calculations during design did, however, indicate a good rate of air flow entering the chamber, even if the numbers are slightly optimistic. A later test of the sensor chamber would be much more valuable if a set of sensors were included, which was never intended in this report.
More unfortunate is the fact that flight performance with the sensor chamber attached was not tested. Since disrupting the propeller generated air flow, the sensor chamber inlets will negatively affect drone efficiency and, hence, flight time. To what extent is not known.

Chapter 10

Analysis, Discussion and Further work

This chapter will take an analytical and critical perspective of components of the complete product, findings during the flight tests, as well as the aspects that were not tested. In addition, a quick analysis of the execution of the project is presented at the end.

The charging solution
Starting with the charging solution and the inductive method of powering the on-board LiPo-charger, Semtech have developed a very robust solution that could provide charging currents up to $\sim$1.6 A for 3S batteries.
One issue, however, was the L7812 voltage regulator reaching a surface temperature unsuitable for skin contact. While the temperature was never measured, it is very plausible that it could damage the PLA printed frame, given the low glass transition temperature of PLA. Even though ABS or any other material may be able to sustain the high temperature, the component does bring in an additional element requiring attention. In a closed up frame heat will eventually build up, and with a heat generating ESC already present there is a chance that higher temperatures inside the drone will damage or reduce performance of certain components. Looking at the scope of the drone, *to measure indoor climate conditions*, the current design with its external sensor chamber will take little damage from heated components. Other designs, however, such as the suggested *modular design 1 construction* with its internal sensor chamber, may get measurements influenced by the presence of the L7812 buck converter.
An alternative to the voltage regulator may lay in the transmitter, which comes with a micro-USB connector that has been used in online guides for transmitter firmware updates through a Windows compatible only software. The manufacturer was unsuccessfully contacted, asking if the transmitter could be programmed so that the receiver outputs less than 19 V (11-14 V). For various reasons (no easy access to a Windows computer, time limitations etc.) the software solution was never investigated. If possible, this could move power dissipation away from the L7812 and the drone, over to the stationary transmitter.

When it comes to the on-board LiPo-charger it performed just as promised, though slightly overcharging the battery and not perfectly balancing the cells. A test of the circuit with no power applied showed no unexpected amount of battery draining. In retrospect, the test could have been improved, as 35 minutes is unlikely fully representative for the amount of time the drone may find itself in standby.
Furthermore, some lacking features can be pointed out, by imagining four states the whole system may, at various frequency, operate at:

- Drone in flight
- Drone docked for re-charge in between flights
- Drone docked and standby for further missions (hours, days)
- Drone and docking station stored away (days, months)

In flight the charging circuit will not operate, and the re-charge in between flights concept has already been proved more or less satisfactory. However, having successfully charged the tested battery at 0.6 A with a dedicated LiPo-charger, the 0.3 A provided during the charging circuit test is an unnecessary limit to the system. Means of setting charging current manually could therefore drastically improve charging time, and even function as a safety barrier if the circuit ever was to pull more current than desired.
The latter two states of operation also bring out a couple of features lacking in the tested solution. LiPo-batteries that are left unused for an undefined amount of time should never be stored fully charged or discharged. As mentioned in the test of the charging circuit, a battery will always drain slowly if left unused. If already ”fully” discharged it may drain beyond the point where the internal energy carrying lithium-ions die off and the battery looses capacity. Many medium-/higher-end chargers will refuse to charge over-discharged batteries for safety purposes. This is not the case for the more ”brute force” Turnigy charger used here, which just points out another lacking safety feature.
When it comes to fully charged batteries they do not take damage from slight continuous discharge over time, but the large amounts of energy stored when standby or stored away pose an unnecessary risk.
Most LiPo-chargers today have the option of charging/discharging batteries to a storage voltage of about 3.8 V per cell; neither fully charged, nor discharged. This is a feature not found in the tested solution.
All this being said, this paper has produced a working circuit where, for now, only the on-board charger needs to be improved (in addition to the L7812 heat issue). Implementing the lacking features mentioned is not far fetched, as they already exist in chargers on the market, with the exception of wireless live data transfer from drone to docking station.

The frame design
When it comes to the drone frame itself, there is no hiding that the weight is greater than ideal, especially when compared to the Black Hornet. It has already been mentioned that the design was purposely over-engineered so that flight tests could be conducted without worrying too much about frame damage. With the exception of the low resolution printed bars connecting shrouds to motor slots the frame sustained a number of crashes, taking no

damage.
A swift re-do of the frame design, reducing wall thickness of shrouds and the internal frame by 50%, brings Fusion 360 estimated frame weight down from 66.5 g to 39.2 g. A simulation of the new design, using the same conditions as in chapter 5.0.3, yields a minimum safety factor of 2.245 and stress distributions shown in figure 10.1

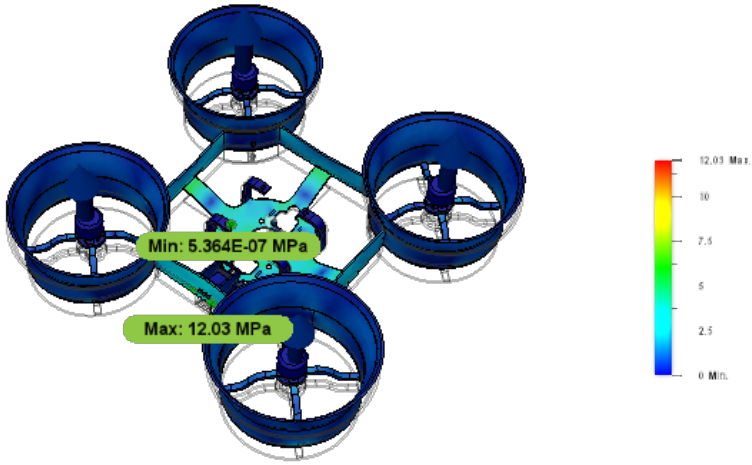

Figure 10.1: Stress distributions (von Mises) in reduced weight frame

While the shrouds continue to operate safely, additional stress is put on the internal frame, where the high maximum stress and low safety factor leaves little room for motor forces greater than the simulated 1 N. This re-do of the design and simulation does, however, prove that frame weight can, to a certain degree, safely be reduced as long as structural supports are implemented at critical points.
The full simulation report can be seen in chapter 12.2, *Analysis Simulation Appendix*.

The current design also leaves some excessive room between the shrouds. If the internal hardware dimensions allow for it the overall width/length of the drone can be reduced by ∼45 mm before the shrouds touch, and weight reduced accordingly. This would, however, require a new solution for LiDAR and sensor chamber modules to be attached, or for them to be a permanent solution of the frame.

Finally, one might argue that taking a different approach when designing the frame would have been better. Instead of over-engineering for safety purposes, the first approach could have been to under-engineer the design, and strengthen weak links in versions two, three and so on. Though this would be more time consuming it is likely to result in a more optimized design.

The shrouds
Three advantages of adding shrouds were mentioned; noise reduction, thrust increase and safety barriers.

In terms of both noise reduction and thrust increase there was little data to compare the use of shrouds to no shrouds with, as the drone was only used with shrouds. A true copy of the drone without shrouds would have been necessary in order for proper comparison. While there are no grounds for comparison, it was simple to conclude already at the first flight that the drone was far too noisy for use in noise sensitive areas, such as office buildings. Even if the shrouds are of sound geometric design they will have little effect when noise reflection and transmission qualities (NRC and STC ratings, respectively) are poor. Earlier mentioned Dotterel Technologies had great success in noise reducing shrouds, but they also had great focus on the choice of lightweight acoustic material. NRC and STC ratings for PLA can be assumed low, though not known, and there is likely to be a great reward in dedicating time on researching ”soundproofing” of the shrouds.
Determining the thrust effect of shrouds is even more challenging, and with the very limited data available on this it was not possible to analyse to what degree shrouds increase thrust. However, calculated flight time based on thrust test data came very close to actual flight time. Since the thrust test was done without shrouds it is implied that the shrouds had little to no effect on flight time and power consumption, and, hence, thrust increase.
The safety aspect of shrouds was (involuntarily) tested several times, most often due to a propeller falling off mid-flight. The conclusion is nearly as simple as the method of testing; shrouds increase safety, especially for the drone itself. Without shrouds present these crashes could potentially have caused broken propellers, damaged motors or caused less rigid parts of the frame to break. Even though the natural movement for a propeller loosening from a horizontally resting drone is upwards and away from humans (Newton’s third law of motion), the shrouds are there to reduce speed of any propellers who’s direction is influenced by imbalanced mounting or foreign objects. The shrouds also protect both humans and material surroundings from propeller contact in case of unfortunate ”bumps”. However, these ”tests” were conducted using over-engineered dimensions. As mentioned earlier, reducing thickness of the shrouds can be considered safe when operating normally, but no simulations on high force impact have been conducted. In other words, there is no guarantee that shrouds of reduced thickness can withstand crashes similar to the ones tested. A highly ductile material with high yield/ultimate strength is either way recommended, while thin shrouds of brittle material increase risk of injury upon impact.

The sensor chamber
While the sensor chamber was never tested calculations on the air flow rate indicated good circulation of air inside. Though it did not work quite as intended, the concept of a replaceable module that can be clipped on to the frame promised easy customization of the inside sensor bundle, as well as size and geometry.
With modular constructions come often performance drawbacks. This was exemplified in the first drone design, a large and bulky construction. In the case of the sensor chamber, as well as the LiDAR mounts, the clip on solution means there is no constant rigid contact between modules and frame. These modules may therefore very well be a source of vibration, which could influence data gathered by the sensors and cause long term ”wear and tear”.
The air ducts, estimated to provide the sensor chamber with a promising air flow of 1.2144 m^3/s, were never tested in action. As mentioned in a previous chapter there is no getting

away from the fact that this will disrupt propeller air flow, and, hence, overall efficiency. An additional element of concern, at least in the current modular clip on design, are the forces exerted on the air duct inlets. To much force on the inlets may cause them to bend and eventually break.
Another potential problem is the fact that the flow rate might be too great, if anywhere near the estimated value. Without knowing the specifications and workings of the sensors to be used, it is possible that air is replaced to fast for the sensors to continuously capture environmental data with high accuracy. The high velocity of incoming air may also have a cooling effect on the temperature sensor, or damage parts inside the chamber.
An alternative solution may be to rather *pull* air into the sensor chamber, rather than pushing it. This can be achieved by, for example, putting an air duct *outlet* at the top of the shroud and using the ventilation grid as an inlet. When the propellers rotate pressure is reduced at the top, and air flows through the chamber in an attempt to equalize the pressure difference. The concept is illustrated in figure 10.2, and may give a slower rate of air circulation as well as reduce the negative impact on overall flight efficiency.

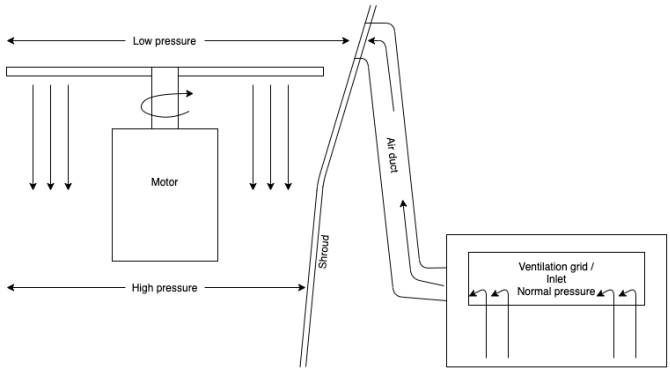

Figure 10.2: An alternative air duct concept

In total, it is likely that permanent solutions are better than clip on modules, as it reduces vibration and gives a more rigid construction. If tested with sufficient airflow for the sensors the above concept is likely far better than the designed clip on modules as well.

The flights
The flights conducted revealed a few weaknesses, with noise and vibrations being some of the first issues discovered. The fact that parts (bolts and heat sink) on both FC and ESC started falling off reveals excessive vibrations in the frame, though these parts may not have been fastened well enough in the first place. Either way, three other potential reasons for why these parts fell off have been considered.
One plausible cause for these vibrations may simply be the poor mounting of the motors. Since these had to be balanced by tightening/loosening their bolts (as the motors were not flat under) it is nearly impossible to perfectly balance them. The motors were re-balanced a number of times, and one of the shrouds in particular has green scratch marks from the green propeller, underlining the fact that the motors were not perfectly balanced. With all

motors potentially slightly inclined to each their direction, the generated air flow stirs up to create high frequency turbulence in the drone. This may also very well also explain why shrouds gave little to no improvement on thrust.
A second potential reason for excessive vibrations lie in the material of the frame. In theory PLA, a material more elastic than for example carbon fibre, should be able to absorb much of the vibration generated in the motors and propellers. That being said, PLA is no perfect material, and a poor design, vibration transmission wise, will transmit some of the induced vibrations.
Finally, the poles holding the FC, including IMU, were also quite unsteady and could be a source of vibration. However, when bolted in place on all four poles, the FC remained fairly rigid. This is somewhat backed up by the gyroscope plots, where roll, pitch and yaw noise come at different amplitudes, with yaw experiencing very little. If the IMU was overly unsteady more vibration should have been seen on the yaw axis. Additionally, unstable FC poles do not explain the ESC heat sink falling off.

A problem that carried on throughout all flights was the drifting issue, mainly on the pitch axis. Re-calibration of the drone and large improvements to the gyro noise did not yield any rewards on this matter.
Again, one may point to the imbalanced motors in a look for an answer. In a perfect system equal force on all motors should balance the drone with no drifting. However, at hover with motors imbalanced, the total motor force will be divided in two components; a vertical and horizontal component. The gyroscope will report no angle of rotation, while, simultaneously, there are horizontal components on the motors that bring the drone to drift.
A different theory, though still with base in the imbalanced motors, involves a ”dance” between the gyroscope and the accelerometer. Continuing from the previous theory, where the drone drifts, but is levelled on all axes, the gyroscope, which is told by the FC/operator to ”keep the drone levelled”, is satisfied. The initial acceleration of drifting does, however, not satisfy the accelerometer, and in an attempt to keep the drone still a set of motors accelerate, inducing a slight inclination in the drone. Once again, the gyroscope gets involved, and, hence, begins the dance between gyroscope and accelerometer.
”Proof” of the ”dance theory” can be seen in figure 9.2, or highlighted in figure 10.3, a segment from the flight #0 blackbox log. A lower frequency can be seen appearing along the high frequencies (later eliminated by the notch filter), while roll/pitch/yaw input commands (RC Command) remain zero (the lower line on RC command is vertical throttle).

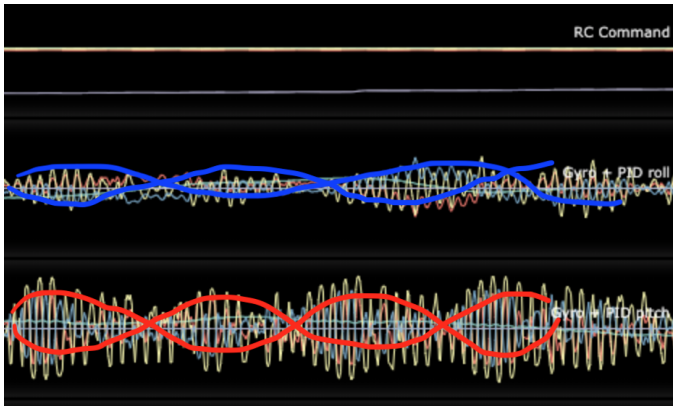

Figure 10.3: "Proof" of the gyroscope-accelerometer dance theory

This latter theory is plausible since *horizon mode* was used in all flights, and, according to one of Oscar Liang's guides:

With Angle mode and Horizon mode, the quadcopter will self-level using both the accelerometer (ACC) and Gyro (Liang, 2018b).

It must, however, be mentioned that Betaflight's architecture of the drone controller is not known, and, to the best of knowledge, not public. There is also no guarantee that this lower frequency noise comes from gyro-accelerometer disagreement. In addition, the noise effect on the yaw axis appeared to be very small, even though one would expect that imbalanced motors cause disturbance on all axes.

If correct, the two theories above may also explain why the simulated step response yielded no steady-state error, while reality presented a drifting drone. The equations of motion derived assume a more or less perfect setup, where, at equilibrium, no horizontal motor force component exists. That being said, the Betaflight software indicates a far more complicated architecture, with options for feed forward, notch filtering and more. A more complex and representative model, preferably coupled and non-linear, would probably be required for accurate enough estimations of drone behaviour.

Estimations of flight time could also benefit from a more complex model. While the method using motor efficiency data came very close to actual flight time it fails to directly take a number of factors into account, such as pitch, diameter and motor specifications. The method therefore presents no fully theoretical option on predicting flight performance for different sets of propellers or motors. Method 1, involving the propeller diameter, is also far too simple, in addition to proving inaccurate in this case. A reason for its inaccuracy may, however, have been the over simplified assumption of mechanical to electrical power efficiency of 0.5.

The hardware
The ESC and FC are hard to judge, as the general impression over a limited amount of flights was that both did their job. Both have promising specifications that never came to full use during this project.
The battery has already been mentioned as a component that should be replaced for increased flight time. Other options for number of cells have not been considered, mostly since 3S batteries have been commonly used in small/medium sized drones. Going up to a four cell battery would complicate and add weight to the charging circuit, and has been discarded. One option lies in the other direction; going down to a 2S battery. Reducing the number of cells helps reduce weight, and allows for a simpler and lighter charging circuit. However, the motors still need a certain amount of power, and with lower voltage this is compensated by higher currents. The solution may therefore only be useful if drone weight can be reduced so that less power is required.

When it comes to the motors these are best selected based on experience or thrust tests. The current motors proved to have more than enough thrust, but produced a lot of audible high frequency noise. High frequency noise generally do not travel as far as low frequency noise, and may be compared to the earlier discussed radio communication frequency, where low frequencies provide range and high frequencies robustness. Depending on the absorption qualities of the shrouds and its surroundings, there is a possibility that low frequency noise would be better. A potential option then is using a lower kV motor for lower RPM (and, hence, lower frequency of noise) with a wider stator for improved torque at low RPM. This could be paired with larger diameter propellers for more thrust, with low to medium pitch for increased low-end torque and lower power consumption. The additional thrust capabilities gained can be used to create space for the slightly heavy and bulky dust sensor, or larger capacity battery.
On the other hand, while this may reduce noise frequency and increase maximum thrust capabilities, it will also increase the visual disturbance of the drone. There is also no guarantee that the above suggestion will produce a more suitable drone for the indoor climate monitoring application, especially considering the fact that intended payload is not very high. Also, with Black Hornet in mind, it should not be impossible to create a small and well performing lightweight drone using motors and propellers similar to the ones already in use.

The execution of the project
In retrospect, a number of things could have been done differently throughout the project. Starting with the design of the frame itself, where mounting holes and receiver container were too small. Some of these faults came from sloppiness, while others were due to limited information available online and not enough time to order, wait and measure component dimensions before designing and printing the frame.
There were also numerous rounds of ordering parts, since it often was discovered that additional necessary parts were missing. The ”blame” for this may be divided between insufficient planning and outlining of the project, irregularities between suppliers on what is included in the product (motors came with bolts included, ESC and FC did not) and limited product information online.

In the end, the project was mostly disrupted by a number of unfortunate events, including the Covid-19-virus, parts lacking in orders and a damaged drone.

Chapter 11

Conclusion

In this thesis, a first step towards an autonomous indoor climate monitoring drone has been taken, with various success on each component of the project.
A method for wireless charging was developed, allowing for charging current up to 0.8 A to 3S batteries. Since using wireless charging technology the concept should be easily implemented in a autonomous solution in the future.
The setup, did, however, generate large amounts of heat due to the L7812 voltage regulator. In addition, while the concept was successfully tested, the LiPo-charger lacks some features before it can operate safely and efficient in an autonomous solution. The charger also limits the charging rate to 0.8 A, while the wireless transmitter/receiver is capable of 20 W, or close to 1.6 A at 12.6 V.

As for the shrouds, there was some hope that these would make a great improvement to drone performance. While there was little ground for comparison, there is doubt as to how much they improved noise reduction and thrust. A possible reason for why the shrouds were not experienced as very noise reducing may be that noise absorbing or soundproof materials were not used. As for thrust increase poorly mounted and balanced motors may have made the drone less efficient, regardless of the use of shrouds. At the same time, shrouds definitely added a layer of safety to drone operation.

The sensor chamber, designed to house environmental sensors and with air inlets connected to propeller air flow, was never tested. It was theoretically ”proven” that it could house a range of sensors, and, at the same time, effectively circulate air in the chamber.
Further analysis on the concept questioned the forces acting on the air duct inlets and to what extent these reduce overall flight efficiency. A concept that avoids interruption with propeller air flow was therefore presented as a potentially better solution in the future.

Finally, the flights are where the most critical flaws in the drone surfaced. A few problems were likely due to motors not being properly mounted, and a ”dance theory”, a theory where imbalanced motors cause ”disagreement” between gyroscope and accelerometer,

was introduced as the reason for a drifting drone.

The work done in this thesis firstly creates a platform for testing autonomous solutions as well as drone mounted environmental sensors. Through experience, certain points that need improvement, and what type of improvement, have been pointed out.

Chapter 12

Further work

Much still remains before the prototype for indoor climate monitoring by drone is ready, and most has already been mentioned in the last few chapters.
Summed up, the following is suggested for further work:

- Design a smarter on-board charger with necessary features
- Thoroughly investigate methods of soundproofing the shrouds. Involving acoustic materials may have a great impact on this
- Derive equations for flight time, power consumption and drone behaviour, taking more parameters as input for better estimations
- Conduct experiments on sensor chamber and consider the suitability of the latest suggested improvement involving low pressure pulling of air
- Thorough review of the frame. Reduce the degree of over-engineering, overall size if possible and make alterations where seen beneficial
- Design and create the full autonomous product, including autonomous interaction between docking station and drone (and cloud)

Bibliography

J. G. Allen. Research: Stale office air is making you less productive, 2017. URL https://hbr.org/2017/03/research-stale-office-air-is-making-you-less-productive.

M. Alvarado, F. Gonzalez, A. Fletcher, and A. Doshi. Towards the development of a low cost airborne sensing system to monitor dust particles after blasting at open-pit mine sites. *Sensors*, 15(8):19667–19687, 2015. ISSN 1424-8220. doi: 10.3390/s150819667. URL https://www.mdpi.com/1424-8220/15/8/19667.

Ash. How to solve transmitter betaflight endpoint mismatches (rxrange), 2017. URL https://www.droningon.co/2017/03/23/transmitter-betaflight-cleanflight-endpoint-midpoint-mismatch-rxrange/.

Banggood. 3s 40a li-ion lithium battery charger protection board pcb bms for drill motor 11.1v 12.6v lipo cell module with balance - a. URL https://bit.ly/30C1Z4K.

Battery University. Charging lithium-ion, 2018. URL https://batteryuniversity.com/learn/article/charging_lithium_ion_batteries.

Benewake. Tfmini datasheet. URL https://www.sgbotic.com/products/datasheets/sensors/DE-LiDAR%20TFmini%20Datasheet-V1.7-EN.pdf.

Berkely Lab. Cost effectiveness of improving indoor environments to increase productivity. URL https://iaqscience.lbl.gov/si/performance-cost.

BetaFPV. 300mah 3s 45c lipo battery r-version. URL https://betafpv.com/products/300mah-3s-45c-lipo-battery-2pcs.

Charlie. Modeling vehicle dynamics – quadcopter equations of motion, 2017. URL https://charlestytler.com/quadcopter-equations-motion/.

Direktoratet for Arbeidstilsynet. Hva melder legene?, 2015. URL https://www.arbeidstilsynet.no/globalassets/om-oss/forskning-og-rapporter/kompass-tema-rapporter/2015/kompass-tema-nr-2-2015-hva-melder-legene.pdf.

Dotterel Technologies. Our tech. URL https://dotterel.co.nz/noise-reduction/.

Drone Omega. The beginner's guide to drone motor essentials. URL https://www.droneomega.com/drone-motor-essentials/.

Elefun. Emax rs1106 ii 4500kv. URL https://www.elefun.no/p/prod.aspx?v=41194.

Elefun. 3s 550mah - 95c - gens ace tattu r-line xt30, a. URL https://www.elefun.no/p/prod.aspx?v=47198.

Elefun. 3s 650mah - 95c - gens ace tattu r-line xt30, b. URL https://www.elefun.no/p/prod.aspx?v=46918.

Elefun. 3s 850mah - 95c - gens ace r-line tattu xt30, c. URL https://www.elefun.no/p/prod.aspx?v=45965.

Elefun. Frsky rxsr s-bus/ccpm, a. URL https://www.elefun.no/p/prod.aspx?v=37107.

Elefun. Hq durable prop t2.5x2.5x3 black (2cw+2ccw), b. URL https://www.elefun.no/p/prod.aspx?v=40396.

Elefun. Hq durable prop t2.5x3.5x3 black (2cw+2ccw), c. URL https://www.elefun.no/p/prod.aspx?v=38891.

fishpepper. Thrust-test: Emax rs1106 4500kv, 2017. URL https://fishpepper.de/2017/11/29/thrust-test-emax-rs1106-4500kv/.

FLIR. Black hornet prs. URL https://www.flir.com/products/black-hornet-prs/.

GetFPV. Aikon ak32pin 20x20 4-in-1 35a 6s blheli32 esc, a. URL https://www.getfpv.com/aikon-ak32pin-20x20-4-in-1-35a-6s-blheli32-esc.html.

GetFPV. Gemfan flash 2540 durable 3 blade (black) - set of 8, b. URL https://www.getfpv.com/gemfan-flash-2540-durable-3-blade-black-set-of-8.html.

GetFPV. Lumenier lux f7 ultimate flight controller (dual gyros), c. URL https://www.getfpv.com/electronics/flight-controllers/lumenier-lux-f7-ultimate-flight-controller-dual-gyros.html.

GetFPV. All about multirotor drone fpv propellers, 2018. URL https://www.getfpv.com/learn/new-to-fpv/all-about-multirotor-fpv-drone-propellers/.

Global Energy Transmission. In-flight wireless charging. URL http://getcorp.com/technology-overview/#tab-542.

Helsedirektoratet. § 19. inneklima/ luftkvalitet. URL https://www.helsedirektoratet.no/veiledere/miljo-og-helse-i-skolen/veiledning-og-god-praksis-1-29/19-inneklima-luftkvalitet.

J. Hendrickson. What are the different self-driving car "levels" of autonomy?, 2020. URL https://www.howtogeek.com/401759/what-are-the-different-self-driving-car-levels-of-autonomy/.

M. Hepperle. How a propeller works, 1997. URL https://www.mh-aerotools.de/airfoils/propuls4.htm.

S. Hill. Wireless charging is convenient, but power over distance remains a challenge, 2019. URL https://www.digitaltrends.com/mobile/state-of-wireless-charging-2019/.

Hobbyking. Turnigy 12v 2-3s basic balance charger. URL https://hobbyking.com/en_us/turnigy-12v-2-3s-basic-balance-charger.html?___store=en_us.

V. Hrishikeshavan and I. Chopra. Development of a quad shrouded rotor micro air vehicle and performance evaluation in edgewise flow. volume 1, 05 2012.

V. Kadamatt. Choosing motors and propellers for multi-rotors, 2017. URL http://www.droneybee.com/choosing-motors-and-propellers-for-multirotors/.

S. Kittelsen. Development of environmental sensor for indoor air quality. December 2019.

J. Kočí. How to improve your 3d prints with annealing, 2019. URL https://blog.prusaprinters.org/how-to-improve-your-3d-prints-with-annealing/.

O. Liang. How to choose propeller for mini quad, 2017a. URL https://oscarliang.com/choose-propellers-mini-quad/.

O. Liang. Esc firmware and protocols overview, 2017b. URL https://oscarliang.com/esc-firmware-protocols/.

O. Liang. How to setup betaflight firmware, 2018a. URL https://oscarliang.com/betaflight-firmware-setup/.

O. Liang. Betaflight modes and how to setup for the first time?, 2018b. URL https://oscarliang.com/betaflight-modes/.

O. Liang. Fpv drone esc buyer's guide, 2020a. URL https://oscarliang.com/choose-esc-racing-drones/.

O. Liang. Fpv drone flight controller explained, 2020b. URL https://oscarliang.com/flight-controller-explained/.

Y. Lu. Industry 4.0: A survey on technologies, applications and open research issues. *Journal of Industrial Information Integration*, 6:1 – 10, 2017. ISSN 2452-414X. doi: https://doi.org/10.1016/j.jii.2017.04.005. URL http://www.sciencedirect.com/science/article/pii/S2452414X17300043.

A. Malaver, N. Motta, P. Corke, and F. Gonzalez. Development and integration of a solar powered unmanned aerial vehicle and a wireless sensor network to monitor greenhouse gases. *Sensors*, 15(2):4072–4096, 2015. ISSN 1424-8220. doi: 10.3390/s150204072. URL https://www.mdpi.com/1424-8220/15/2/4072.

Noise Control Specialist. Acoustic materials 101. URL https://noisecontrolspecialist.com/acoustical-materials-101/.

D. Palossi, A. Loquercio, F. Conti, E. Flamand, D. Scaramuzza, and L. Benini. A 64-mw dnn-based visual navigation engine for autonomous nano-drones. *IEEE Internet of Things Journal*, 6(5):8357–8371, 2019.

Qnovo. Why is charging with cccv bad?, 2014. URL https://qnovo.com/why-is-charging-with-cccv-bad/.

G. Rohi, O. Ejofodomi, and G. Ofualagbaa. Autonomous monitoring, analysis, and countering of air pollution using environmental drones. 2019. URL https://www.ncbi.nlm.nih.gov/pmc/articles/PMC6971350/.

RS Components. Ansmann 12 v dc, 15 v dc, 18 v dc, 19 v dc, 20 v dc, 22 v dc, 24 v dc power supply. URL https://no.rs-online.com/web/p/desktop-power-supplies/7023265/.

J. Ruiz-Jimenez, N. Zanca, H. Lan, M. Jussila, K. Hartonen, and M.-L. Riekkola. Aerial drone as a carrier for miniaturized air sampling systems. *Journal of Chromatography A*, 1597:202 – 208, 2019. ISSN 0021-9673. doi: https://doi.org/10.1016/j.chroma.2019.04.009. URL http://www.sciencedirect.com/science/article/pii/S0021967319303632.

J. Salt. 11 things to know about lipo batteries to get the best performance, life, value fun out of them, whatever you fly, 2020. URL https://www.rchelicopterfun.com/lipo-batteries.html.

Scentroid. Dr1000 flying lab. URL https://scentroid.com/products/analyzers/dr1000-flying-lab/.

F. Scibilia. Lecture: Introduction to autonomous robotics systems for industry 4.0, 2019.

Semtech. Semtech tsdmrx-19v/20w-evm, a. URL https://www.semtech.com/products/wireless-charging/linkcharge-medium-power-evms/linkcharge-20-receiver-tsdmrx-19v-20w-evm.

Semtech. Semtech tsdmtx-19v2-evm, b. URL https://www.semtech.com/products/wireless-charging/linkcharge-medium-power-evms/linkcharge-20-transmitter-tsdmtx-19v2-evm.

Semtech. User guide tsdmtx-19v2-evm dual-mode (qi and pma) wireless charging (rev1.0) transmitter, 2016. URL https://no.mouser.com/datasheet/2/761/TSDMTX-19V2-EVM-1278486.pdf.

Simplify3D. Filament properties table. URL https://www.simplify3d.com/support/materials-guide/properties-table/?filas=abs,pla.

R. Singh, R. Kumar, I. Farina, F. Colangelo, L. Feo, and F. Fraternali. Multi-material additive manufacturing of sustainable innovative materials and structures. *Polymers*, 11:62, 01 2019. doi: 10.3390/polym11010062.

Skysense. Indoor drone charging pad and infrastructure. URL https://www.skysense.co/indoor-charging-pad.

P. Spychalski. Frsky accst 2.x.x update for all accst transmitters and receivers, 2020. URL https://www.youtube.com/watch?v=RY5W0v2Tmtw.

Stanbur/RCGroups. battery, esc, and motor temps, 2017. URL https://www.rcgroups.com/forums/showthread.php?2839133-battery-esc-and-motor-temps.

StarscreamF22/RCUniverse. Need advice on my temperatures and possibly suitable esc and motor., May 2014. URL https://www.rcuniverse.com/forum/rc-electric-off-road-trucks-buggies-truggies-more-147/11598697-need-advice-my-temperatures-possibly-suitable-esc-motor.html.

STMicroelectr. L7800 series, 1998. URL https://www.hobbytronics.co.uk/datasheets/L7812.pdf.

A. Suleiman, Z. Zhang, L. Carlone, S. Karaman, and V. Sze. Navion: A 2-mw fully integrated real-time visual-inertial odometry accelerator for autonomous navigation of nano drones. *IEEE Journal of Solid-State Circuits*, 54(4):1106–1119, 2019.

The Revolutionaries. Phonix nanofibre-enhanced products winning innovation awards, 2016. URL https://www.revolutionfibres.com/2016/04/phonix-nanofibre-enhanced-products-winning-innovation-awards/.

J. Uthira Kumar, E. Narvydas, and D. Eidukynas. Reverse engineering and cfd analysis of propeller. 05 2017.

WiBotic. Products. URL https://www.wibotic.com/products/.

D. Wyon and P. Wargocki. How indoor environment affects performance. *A S H R A E Journal*, 55(3):46–52, 2013. ISSN 0001-2491. Copyright 2013 ASHRAE.

Appendix

12.1 Simulation Appendix

Simulation PDF starts at next page

Simulation Model 1:1

Study 1 - Static Stress

Study Properties

Study Type	Static Stress
Last Modification Date	2020-05-04, 15:50:40

Settings

General

Contact Tolerance	0.1 mm
Remove Rigid Body Modes	No

Damping

Mesh

Average Element Size (% of model size)	
Solids	5
Scale Mesh Size Per Part	No
Average Element Size (absolute value)	-
Element Order	Parabolic
Create Curved Mesh Elements	No
Max. Turn Angle on Curves (Deg.)	60
Max. Adjacent Mesh Size Ratio	1.5
Max. Aspect Ratio	10
Minimum Element Size (% of average size)	20

Adaptive Mesh Refinement

Number of Refinement Steps	0
Results Convergence Tolerance (%)	20
Portion of Elements to Refine (%)	10
Results for Baseline Accuracy	Von Mises Stress

Materials

Component	Material	Safety Factor
SHROUD	ABS Plastic	Yield Strength
FRAME	ABS Plastic	Yield Strength
SHROUD (1)	ABS Plastic	Yield Strength
SHROUD (2)	ABS Plastic	Yield Strength
SHROUD (1) (1)	ABS Plastic	Yield Strength
Body21	ABS Plastic	Yield Strength
Body22	ABS Plastic	Yield Strength
EMAX RS1106 II v2:1/Body1	Motor	Yield Strength
EMAX RS1106 II v2:1/Body2	Motor	Yield Strength
EMAX RS1106 II v2(Mirror):1/Body1	Motor	Yield Strength
EMAX RS1106 II v2(Mirror):1/Body2	Motor	Yield Strength
EMAX RS1106 II v2(Mirror) (1):1/Body1	Motor	Yield Strength
EMAX RS1106 II v2(Mirror) (1):1/Body2	Motor	Yield Strength
EMAX RS1106 II v2(Mirror)(Mirror):1/Body1	Motor	Yield Strength
EMAX RS1106 II v2(Mirror)(Mirror):1/Body2	Motor	Yield Strength
Aikon AK32PIN 20x20 4-in-1 35A 6S ESC v3:1/Body1	ESC	Yield Strength
Aikon AK32PIN 20x20 4-in-1 35A 6S ESC v3:1/Body2	Steel	Yield Strength
Aikon AK32PIN 20x20 4-in-1 35A 6S ESC v3:1/Body3	Steel	Yield Strength

Aikon AK32PIN 20x20 4-in-1 35A 6S ESC v3:1/Body4	Steel	Yield Strength
Aikon AK32PIN 20x20 4-in-1 35A 6S ESC v3:1/Body5	Steel	Yield Strength
Aikon AK32PIN 20x20 4-in-1 35A 6S ESC v3:1/Body6	Steel	Yield Strength
Aikon AK32PIN 20x20 4-in-1 35A 6S ESC v3:1/Body7	Steel	Yield Strength
Aikon AK32PIN 20x20 4-in-1 35A 6S ESC v3:1/Body8	Steel	Yield Strength
Aikon AK32PIN 20x20 4-in-1 35A 6S ESC v3:1/Body9	Steel	Yield Strength
Aikon AK32PIN 20x20 4-in-1 35A 6S ESC v3:1/Body10	Steel	Yield Strength
Aikon AK32PIN 20x20 4-in-1 35A 6S ESC v3:1/Body11	Steel	Yield Strength
Aikon AK32PIN 20x20 4-in-1 35A 6S ESC v3:1/Body12	Steel	Yield Strength
Aikon AK32PIN 20x20 4-in-1 35A 6S ESC v3:1/Body13	Steel	Yield Strength
Aikon AK32PIN 20x20 4-in-1 35A 6S ESC v3:1/Body14	Steel	Yield Strength
Aikon AK32PIN 20x20 4-in-1 35A 6S ESC v3:1/Body15	Steel	Yield Strength
Aikon AK32PIN 20x20 4-in-1 35A 6S ESC v3:1/Body16	Steel	Yield Strength
Aikon AK32PIN 20x20 4-in-1 35A 6S ESC v3:1/Body17	Steel	Yield Strength
Aikon AK32PIN 20x20 4-in-1 35A 6S ESC v3:1/Body18	Steel	Yield Strength
Aikon AK32PIN 20x20 4-in-1 35A 6S ESC v3:1/Body19	Steel	Yield Strength
Aikon AK32PIN 20x20 4-in-1 35A 6S ESC v3:1/Body20	Steel	Yield Strength
Lumenier LUX F7 Ultimate Flight Controller v4:1	Flight Controller	Yield Strength

⊟ Motor

Density	4E-06 kg / mm^3
Young's Modulus	210000 MPa
Poisson's Ratio	0.3
Yield Strength	207 MPa
Ultimate Tensile Strength	345 MPa
Thermal Conductivity	0.056 W / (mm C)
Thermal Expansion Coefficient	1.2E-05 / C
Specific Heat	480 J / (kg C)

⊟ Flight Controller

Density	3E-06 kg / mm^3
Young's Modulus	210000 MPa
Poisson's Ratio	0.3
Yield Strength	207 MPa
Ultimate Tensile Strength	345 MPa
Thermal Conductivity	0.056 W / (mm C)
Thermal Expansion Coefficient	1.2E-05 / C
Specific Heat	480 J / (kg C)

⊟ ESC

Density	3E-06 kg / mm^3
Young's Modulus	210000 MPa
Poisson's Ratio	0.3
Yield Strength	207 MPa
Ultimate Tensile Strength	345 MPa
Thermal Conductivity	0.056 W / (mm C)
Thermal Expansion Coefficient	1.2E-05 / C
Specific Heat	480 J / (kg C)

⊟ Steel

Density	7.85E-06 kg / mm^3
Young's Modulus	210000 MPa
Poisson's Ratio	0.3
Yield Strength	207 MPa
Ultimate Tensile Strength	345 MPa
Thermal Conductivity	0.056 W / (mm C)

Thermal Expansion Coefficient	1.2E-05 / C
Specific Heat	480 J / (kg C)

ABS Plastic

Density	1.06E-06 kg / mm^3
Young's Modulus	2240 MPa
Poisson's Ratio	0.38
Yield Strength	20 MPa
Ultimate Tensile Strength	29.6 MPa
Thermal Conductivity	1.6E-04 W / (mm C)
Thermal Expansion Coefficient	8.57E-05 / C
Specific Heat	1500 J / (kg C)

Contacts

Bonded

Name
[S] Bonded1 [Aikon AK32PIN 20x20 4-in-1 35A 6S ESC v3:1(Body1)||Aikon AK32PIN 20x20 4-in-1 35A 6S ESC v3:1(Body20)]
[S] Bonded2 [Aikon AK32PIN 20x20 4-in-1 35A 6S ESC v3:1(Body1)||Aikon AK32PIN 20x20 4-in-1 35A 6S ESC v3:1(Body19)]
[S] Bonded3 [Aikon AK32PIN 20x20 4-in-1 35A 6S ESC v3:1(Body1)||Aikon AK32PIN 20x20 4-in-1 35A 6S ESC v3:1(Body18)]
[S] Bonded4 [Aikon AK32PIN 20x20 4-in-1 35A 6S ESC v3:1(Body1)||Aikon AK32PIN 20x20 4-in-1 35A 6S ESC v3:1(Body17)]
[S] Bonded5 [Aikon AK32PIN 20x20 4-in-1 35A 6S ESC v3:1(Body1)||Aikon AK32PIN 20x20 4-in-1 35A 6S ESC v3:1(Body16)]
[S] Bonded6 [Aikon AK32PIN 20x20 4-in-1 35A 6S ESC v3:1(Body1)||Aikon AK32PIN 20x20 4-in-1 35A 6S ESC v3:1(Body15)]
[S] Bonded7 [Aikon AK32PIN 20x20 4-in-1 35A 6S ESC v3:1(Body1)||Aikon AK32PIN 20x20 4-in-1 35A 6S ESC v3:1(Body14)]
[S] Bonded8 [Aikon AK32PIN 20x20 4-in-1 35A 6S ESC v3:1(Body1)||Aikon AK32PIN 20x20 4-in-1 35A 6S ESC v3:1(Body13)]
[S] Bonded9 [Aikon AK32PIN 20x20 4-in-1 35A 6S ESC v3:1(Body1)||Aikon AK32PIN 20x20 4-in-1 35A 6S ESC v3:1(Body12)]
[S] Bonded10 [Aikon AK32PIN 20x20 4-in-1 35A 6S ESC v3:1(Body1)||Aikon AK32PIN 20x20 4-in-1 35A 6S ESC v3:1(Body11)]
[S] Bonded11 [Aikon AK32PIN 20x20 4-in-1 35A 6S ESC v3:1(Body1)||Aikon AK32PIN 20x20 4-in-1 35A 6S ESC v3:1(Body10)]
[S] Bonded12 [Aikon AK32PIN 20x20 4-in-1 35A 6S ESC v3:1(Body1)||Aikon AK32PIN 20x20 4-in-1 35A 6S ESC v3:1(Body9)]
[S] Bonded13 [Aikon AK32PIN 20x20 4-in-1 35A 6S ESC v3:1(Body1)||Aikon AK32PIN 20x20 4-in-1 35A 6S ESC v3:1(Body8)]
[S] Bonded14 [Aikon AK32PIN 20x20 4-in-1 35A 6S ESC v3:1(Body1)||Aikon AK32PIN 20x20 4-in-1 35A 6S ESC v3:1(Body7)]
[S] Bonded15 [Aikon AK32PIN 20x20 4-in-1 35A 6S ESC v3:1(Body1)||Aikon AK32PIN 20x20 4-in-1 35A 6S ESC v3:1(Body6)]
[S] Bonded16 [Aikon AK32PIN 20x20 4-in-1 35A 6S ESC v3:1(Body1)||Aikon AK32PIN 20x20 4-in-1 35A 6S ESC v3:1(Body5)]
[S] Bonded17 [Aikon AK32PIN 20x20 4-in-1 35A 6S ESC v3:1(Body1)||Aikon AK32PIN 20x20 4-in-1 35A 6S ESC v3:1(Body4)]
[S] Bonded18 [Aikon AK32PIN 20x20 4-in-1 35A 6S ESC v3:1(Body1)||Aikon AK32PIN 20x20 4-in-1 35A 6S ESC v3:1(Body3)]
[S] Bonded19 [Aikon AK32PIN 20x20 4-in-1 35A 6S ESC v3:1(Body1)||Aikon AK32PIN 20x20 4-in-1 35A 6S ESC v3:1(Body2)]
[S] Bonded20 [EMAX RS1106 II v2(Mirror)(Mirror):1(Body1)||EMAX RS1106 II v2(Mirror)(Mirror):1(Body2)]
[S] Bonded21 [EMAX RS1106 II v2(Mirror) (1):1(Body1)||EMAX RS1106 II v2(Mirror) (1):1(Body2)]
[S] Bonded22 [EMAX RS1106 II v2(Mirror):1(Body1)||EMAX RS1106 II v2(Mirror):1(Body2)]
[S] Bonded23 [EMAX RS1106 II v2:1(Body1)||EMAX RS1106 II v2:1(Body2)]
[S] Bonded24 [Simulation Model 1:1(SHROUD (1) (1))||EMAX RS1106 II v2(Mirror)(Mirror):1(Body1)]
[S] Bonded25 [Simulation Model 1:1(SHROUD (2))||EMAX RS1106 II v2(Mirror) (1):1(Body1)]
[S] Bonded26 [Simulation Model 1:1(SHROUD (1))||EMAX RS1106 II v2(Mirror):1(Body1)]

[S] Bonded27 [Simulation Model 1:1(FRAME)||Simulation Model 1:1(Body22)]
[S] Bonded28 [Simulation Model 1:1(FRAME)||Simulation Model 1:1(Body22)]
[S] Bonded29 [Simulation Model 1:1(FRAME)||Simulation Model 1:1(Body21)]
[S] Bonded30 [Simulation Model 1:1(FRAME)||Simulation Model 1:1(Body21)]
[S] Bonded31 [Simulation Model 1:1(FRAME)||Simulation Model 1:1(SHROUD (2))]
[S] Bonded32 [Simulation Model 1:1(FRAME)||Simulation Model 1:1(SHROUD (1))]
[S] Bonded33 [Simulation Model 1:1(FRAME)||Simulation Model 1:1(SHROUD (1) (1))]
[S] Bonded34 [Simulation Model 1:1(FRAME)||Aikon AK32PIN 20x20 4-in-1 35A 6S ESC v3:1(Body1)]
[S] Bonded35 [Simulation Model 1:1(FRAME)||Lumenier LUX F7 Ultimate Flight Controller v4:1]
[S] Bonded36 [Simulation Model 1:1(FRAME)||Lumenier LUX F7 Ultimate Flight Controller v4:1]
[S] Bonded37 [Simulation Model 1:1(FRAME)||Lumenier LUX F7 Ultimate Flight Controller v4:1]
[S] Bonded38 [Simulation Model 1:1(FRAME)||Lumenier LUX F7 Ultimate Flight Controller v4:1]
[S] Bonded39 [Simulation Model 1:1(SHROUD)||Simulation Model 1:1(FRAME)]
[S] Bonded40 [Simulation Model 1:1(SHROUD)||EMAX RS1106 II v2:1(Body1)]

Mesh

Type	Nodes	Elements
Solids	211629	110547

Load Case1

Constraints

Fixed1

Type	Fixed
Ux	Yes
Uy	Yes
Uz	Yes

Selected Entities

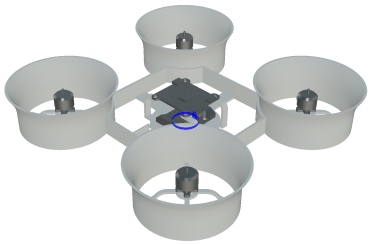

Loads

Force1

Type	Force
Magnitude	1 N
X Value	0 N
Y Value	1 N
Z Value	0 N
Flip Direction	Yes
Force Per Entity	Yes

Selected Entities

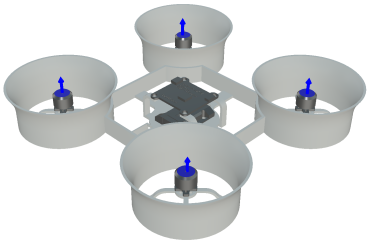

Results

Result Summary

Name	Minimum	Maximum
Safety Factor		
Safety Factor (Per Body)	7.226	15
Stress		
Von Mises	2.769E-06 MPa	3.221 MPa
1st Principal	-1.722 MPa	2.888 MPa
3rd Principal	-4.126 MPa	1.149 MPa
Normal XX	-3.167 MPa	1.808 MPa
Normal YY	-2.731 MPa	1.348 MPa
Normal ZZ	-2.85 MPa	2.636 MPa
Shear XY	-1.484 MPa	1.155 MPa
Shear YZ	-0.8007 MPa	1.153 MPa
Shear ZX	-1.087 MPa	1.051 MPa
Displacement		
Total	0 mm	0.5963 mm
X	-0.09084 mm	0.1012 mm
Y	-3.349E-04 mm	0.5812 mm
Z	-0.08335 mm	0.1159 mm
Reaction Force		
Total	0 N	4.117 N
X	-0.2034 N	0.195 N
Y	-3.122 N	4.115 N
Z	-0.3703 N	0.3007 N
Strain		
Equivalent	1.631E-11	0.001868
1st Principal	-4.938E-08	0.001958
3rd Principal	-0.001565	7.41E-07
Normal XX	-9.596E-04	7.651E-04
Normal YY	-4.675E-04	4.501E-04
Normal ZZ	-0.001117	0.001056
Shear XY	-8.366E-04	8.934E-04
Shear YZ	-7.251E-04	9.86E-04
Shear ZX	-0.001339	0.001295
Contact Pressure		
Total	0 MPa	2.104 MPa
X	-0.9395 MPa	0.7816 MPa
Y	-0.9398 MPa	1.745 MPa
Z	-1.153 MPa	0.8002 MPa

Safety Factor

⊟ **Safety Factor (Per Body)**

0 8, Threshold: 4.8 - 8

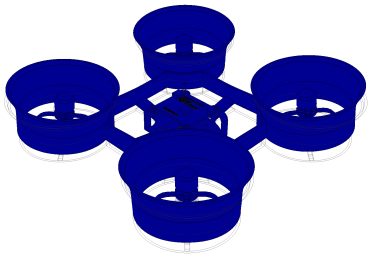

⊟ **Stress**

⊟ **Von Mises**

[MPa] 0 3.221

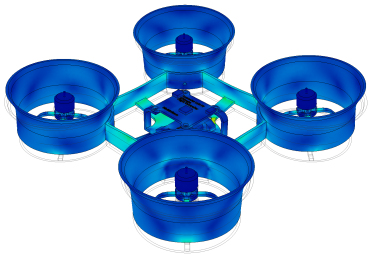

⊟ **1st Principal**

[MPa] -1.722 2.888

⊟ **3rd Principal**

[MPa] -4.126 1.149

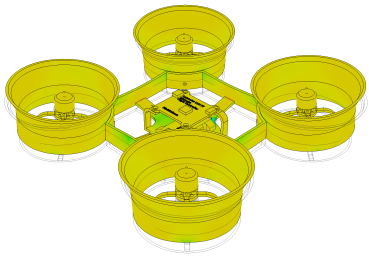

⊟ **Displacement**

⊟ **Total**

[mm] 0 0.5963

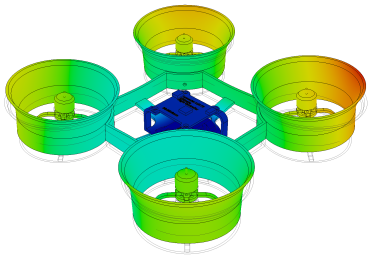

12.2 Analysis Simulation Appendix

Simulation PDF starts at next page

Simulation Model 1:1

Study 2 - Static Stress

Study Properties

Study Type	Static Stress
Last Modification Date	2020-06-08, 11:36:00

Settings

General

Contact Tolerance	0.1 mm
Remove Rigid Body Modes	No

Damping

Mesh

Average Element Size (% of model size)	
Solids	5
Scale Mesh Size Per Part	No
Average Element Size (absolute value)	-
Element Order	Parabolic
Create Curved Mesh Elements	No
Max. Turn Angle on Curves (Deg.)	60
Max. Adjacent Mesh Size Ratio	1.5
Max. Aspect Ratio	10
Minimum Element Size (% of average size)	20

Adaptive Mesh Refinement

Number of Refinement Steps	0
Results Convergence Tolerance (%)	20
Portion of Elements to Refine (%)	10
Results for Baseline Accuracy	Von Mises Stress

Materials

Component	Material	Safety Factor
SHROUD	ABS Plastic	Yield Strength
FRAME	ABS Plastic	Yield Strength
SHROUD (1)	ABS Plastic	Yield Strength
SHROUD (2)	ABS Plastic	Yield Strength
SHROUD (1) (1)	ABS Plastic	Yield Strength
Body21	ABS Plastic	Yield Strength
Body22	ABS Plastic	Yield Strength
MOUNTING SLOT	Rilsan Invent Natural - PA 11	Yield Strength
EMAX RS1106 II v2:1/Body1	Motor	Yield Strength
EMAX RS1106 II v2:1/Body2	Motor	Yield Strength
EMAX RS1106 II v2(Mirror):1/Body1	Motor	Yield Strength
EMAX RS1106 II v2(Mirror):1/Body2	Motor	Yield Strength
EMAX RS1106 II v2(Mirror) (1):1/Body1	Motor	Yield Strength
EMAX RS1106 II v2(Mirror) (1):1/Body2	Motor	Yield Strength
EMAX RS1106 II v2(Mirror)(Mirror):1/Body1	Motor	Yield Strength
EMAX RS1106 II v2(Mirror)(Mirror):1/Body2	Motor	Yield Strength

Rilsan Invent Natural - PA 11

Density	1.02E-06 kg / mm^3
Young's Modulus	1500 MPa
Poisson's Ratio	0.44
Yield Strength	43 MPa
Ultimate Tensile Strength	53 MPa
Thermal Conductivity	2.25E-04 W / (mm C)
Thermal Expansion Coefficient	1.3E-04 / C
Specific Heat	15000 J / (kg C)

⊟ Motor

Density	4E-06 kg / mm^3
Young's Modulus	210000 MPa
Poisson's Ratio	0.3
Yield Strength	207 MPa
Ultimate Tensile Strength	345 MPa
Thermal Conductivity	0.056 W / (mm C)
Thermal Expansion Coefficient	1.2E-05 / C
Specific Heat	480 J / (kg C)

⊟ ABS Plastic

Density	1.06E-06 kg / mm^3
Young's Modulus	2240 MPa
Poisson's Ratio	0.38
Yield Strength	20 MPa
Ultimate Tensile Strength	29.6 MPa
Thermal Conductivity	1.6E-04 W / (mm C)
Thermal Expansion Coefficient	8.57E-05 / C
Specific Heat	1500 J / (kg C)

⊟ Contacts

⊟ Bonded

Name
[S] Bonded9 [EMAX RS1106 II v2(Mirror)(Mirror):1(Body1)||EMAX RS1106 II v2(Mirror)(Mirror):1(Body2)]
[S] Bonded10 [EMAX RS1106 II v2(Mirror) (1):1(Body1)||EMAX RS1106 II v2(Mirror) (1):1(Body2)]
[S] Bonded11 [EMAX RS1106 II v2(Mirror):1(Body1)||EMAX RS1106 II v2(Mirror):1(Body2)]
[S] Bonded12 [EMAX RS1106 II v2:1(Body1)||EMAX RS1106 II v2:1(Body2)]
[S] Bonded20 [Simulation Model 1:1(Body22)||Simulation Model 1:1(MOUNTING SLOT)]
[S] Bonded21 [Simulation Model 1:1(Body22)||Simulation Model 1:1(MOUNTING SLOT)]
[S] Bonded22 [Simulation Model 1:1(Body21)||Simulation Model 1:1(MOUNTING SLOT)]
[S] Bonded23 [Simulation Model 1:1(Body21)||Simulation Model 1:1(MOUNTING SLOT)]
[S] Bonded24 [Simulation Model 1:1(SHROUD (1) (1))||EMAX RS1106 II v2(Mirror)(Mirror):1(Body1)]
[S] Bonded25 [Simulation Model 1:1(SHROUD (2))||EMAX RS1106 II v2(Mirror) (1):1(Body1)]
[S] Bonded27 [Simulation Model 1:1(SHROUD (1))||EMAX RS1106 II v2(Mirror):1(Body1)]
[S] Bonded41 [Simulation Model 1:1(FRAME)||Simulation Model 1:1(MOUNTING SLOT)]
[S] Bonded42 [Simulation Model 1:1(FRAME)||Simulation Model 1:1(MOUNTING SLOT)]
[S] Bonded43 [Simulation Model 1:1(FRAME)||Simulation Model 1:1(MOUNTING SLOT)]
[S] Bonded44 [Simulation Model 1:1(FRAME)||Simulation Model 1:1(MOUNTING SLOT)]
[S] Bonded46 [Simulation Model 1:1(SHROUD)||EMAX RS1106 II v2:1(Body1)]
[S] Bonded47 [Simulation Model 1:1(FRAME)||Simulation Model 1:1(SHROUD (2))]
[S] Bonded48 [Simulation Model 1:1(FRAME)||Simulation Model 1:1(SHROUD (1))]
[S] Bonded49 [Simulation Model 1:1(FRAME)||Simulation Model 1:1(SHROUD (1) (1))]
[S] Bonded50 [Simulation Model 1:1(SHROUD)||Simulation Model 1:1(FRAME)]

⊟ Mesh

Type	Nodes	Elements

Solids	80905	39626

Load Case1

Constraints

Fixed1

Type	Fixed
Ux	Yes
Uy	Yes
Uz	Yes

Selected Entities

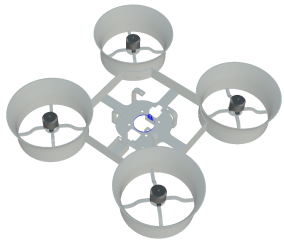

Loads

Force1

Type	Force
Magnitude	-1 N
X Value	0 N
Y Value	1 N
Z Value	0 N
Force Per Entity	Yes

Selected Entities

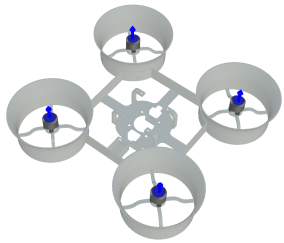

Results

Result Summary

Name	Minimum	Maximum

Safety Factor		
Safety Factor (Per Body)	2.245	15
Stress		
Von Mises	5.364E-07 MPa	12.03 MPa
1st Principal	-10.86 MPa	25.66 MPa
3rd Principal	-19.19 MPa	15.45 MPa
Normal XX	-12.7 MPa	18.8 MPa
Normal YY	-11.42 MPa	18.51 MPa
Normal ZZ	-18.55 MPa	22.41 MPa
Shear XY	-2.904 MPa	3.072 MPa
Shear YZ	-1.858 MPa	2.849 MPa
Shear ZX	-4.391 MPa	3.611 MPa
Displacement		
Total	0 mm	3.339 mm
X	-0.5193 mm	0.5128 mm
Y	-9.809E-04 mm	3.317 mm
Z	-0.7105 mm	0.6012 mm
Reaction Force		
Total	0 N	10.68 N
X	-2.501 N	2.202 N
Y	-5.698 N	10.46 N
Z	-1.937 N	2.042 N
Strain		
Equivalent	7.094E-11	0.01134
1st Principal	-2.903E-11	0.01251
3rd Principal	-0.008634	3.756E-11
Normal XX	-0.004015	0.004055
Normal YY	-0.004003	0.003743
Normal ZZ	-0.008193	0.007458
Shear XY	-0.003579	0.003785
Shear YZ	-0.002592	0.00547
Shear ZX	-0.008431	0.006934
Contact Pressure		
Total	0 MPa	22.88 MPa
X	-12.12 MPa	12.17 MPa
Y	-2.876 MPa	4.431 MPa
Z	-18.55 MPa	22.41 MPa

⊟ Safety Factor

⊟ Safety Factor (Per Body)

0 8

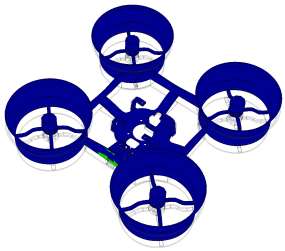

⊟ Stress

Von Mises

[MPa] 0 12.03

1st Principal

[MPa] -10.86 25.66

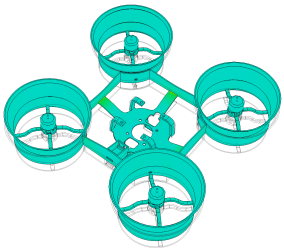

3rd Principal

[MPa] -19.19 15.45

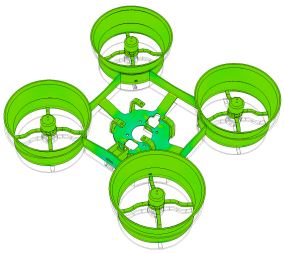

Displacement

Total
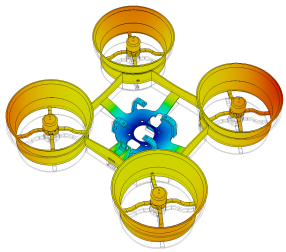
[mm] 0 3.339